MONASH University

Characteristics of the Atmospheric Boundary Layer at Different Scales

by

Francisco Andrés Lang Tasso

A thesis submitted for the degree of

Doctor of Philosophy

in

Atmospheric Sciences

at

Monash University

School of Earth, Atmosphere, and Environment

Victoria, Australia

June 2018

Copyright Notice

Abstract

The behaviour of the atmospheric boundary layer (ABL) at different scales of motion is described with an emphasis on the largest contributions to the total turbulence kinetic energy (TKE). First, large sudden wind-direction shifts and submesoscale (or submeso) motion variability under nocturnal conditions over land are examined using a micrometeorological network of stations in north-western Victoria, Australia. Submeso motions generally includes the complex mix of motions on scales between the main turbulent eddies and smallest mesoscale motions (<2 km). The submeso motions at the study site exhibit behaviour typical of flat terrain, such as the lower relative mesovelocity scale and smaller cross-wind variances than that for complex terrain. Large wind-direction shifts tend to be associated with a sharp decrease in air temperature (74% of the time), which is associated with rising motion of cold air, followed by an increase in turbulent mixing.

Second, we explore changes in the thermodynamic structure of the Marine Atmospheric Boundary Layer (MABL) over the Southern Ocean (SO) in relation to the synoptic meteorology, where the SO storm track modulates the ABL. The specific focus is to analyse cold front passages over the SO, which may be a major contributor to the large shortwave radiative bias in this region. Thermodynamic profiles of the MABL from the ERA-Interim reanalyses are compared/evaluated with observations from Macquarie Island. Observations confirm that boundary layer clouds over the SO commonly reside within a shallow MABL under the influence of frequent mid-latitude cyclones and fronts. The evaluation of MABL height reveals that under cold frontal passages, the main inversion heights are underestimated by ERA-Interim by 22%. Significant differences are found in the moisture profiles within the MABL between the observations and ERA-Interim soundings within the context of cold frontal passages. The moisture in the ERA-Interim is found to be too confined to the surface layer, which is consistent with the shallower MABL represented by the ERA-Interim. Analysis of the surface precipitation unrelated to the passage of cold fronts shows that the annual ERA-Interim precipitation is lower than Macquarie Island precipitation by 11%. In addition, the hourly Macquarie Island precipitation records were used to examined the diurnal cycles and their relationship with the MABL. The results show that the greatest variation of the diurnal precipitation cycle occurs during the austral summer, with a magnitude $\sim$0.04 mm hr^{-1}. The highest amount of precipitation occurred at night during summer. Variability of precipitation is not reflected in changes of water content within the MABL.

In the last part of this research, shipborne observations from the CAPRICORN exper-

iment have been used to evaluate the Weather Research and Forecasting (WRF) model, in simulating the cold front passages over the SO (cases studies on the synoptic scale). The simulated MABL thermodynamic structure and atmospheric water content are compared against the observations. Experiments are also undertaken to test the sensitivity of microphysical schemes and planetary boundary layer schemes. The WRF simulations demonstrate a considerable level of skill in representing the temperature profiles and the MABL heights under pre- and post-frontal conditions. However, the simulations have difficulties reproducing cloud fraction and cloud phase, which was more extensive under post-frontal conditions.

Declaration

This thesis contains no material which has been accepted for the award of any other degree or diploma at any university or equivalent institution and that, to the best of my knowledge and belief, this thesis contains no material previously published or written by another person, except where due reference is made in the text of the thesis.
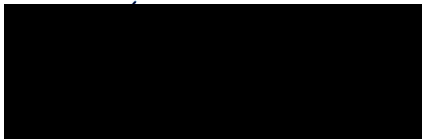
Francisco Andrés Lang Tasso

September 17, 2018

Publications during enrolment

- Lang, F., D. Belušić and S. Siems (2018). Observations of wind-direction variability in the nocturnal boundary layer. *Boundary-Layer Meteorol.* 166(1), 51-68. doi: 10.1007/s10546-017-0296-4.

- Lang, F., Y. Huang, S. T. Siems and M. J. Manton (2018). Characteristics of the marine atmospheric boundary layer over the Southern Ocean in response to the synoptic forcing. *J. Geophys. Res.: Atmospheres.* 123(15), 7799-7820. doi: 10.1029/2018JD028700

Thesis including published works declaration

I hereby declare that this thesis contains no material which has been accepted for the award of any other degree or diploma at any university or equivalent institution and that, to the best of my knowledge and belief, this thesis contains no material previously published or written by another person, except where due reference is made in the text of the thesis.

This thesis includes 2 original papers published in peer reviewed journals. The core theme of the thesis is boundary later meteorology. The ideas, development and writing up of all the papers in the thesis were the principal responsibility of myself, the student, working within the School of Earth, Atmosphere and Environment under the supervision of A/Prof. Steven T. Siems. The inclusion of co-authors reflects the fact that the work came from active collaboration between researchers and acknowledges input into team-based research. In the case of Chapters 2 and 3 my contribution to the work involved the following:

Thesis Chapter	Publication Title	Status	Nature and % of student contribution	Co-author name(s) Nature and % of Co-author's contribution	Co-author(s) Monash student Y/N
2	Observations of wind-direction variability in the nocturnal boundary layer	Published	80% Concept, processing data and writing drafts	1) Danijel Belušić, concept and writing, 10% 2) Steven T. Siems, revision 10%	No
3	Characteristics of the marine atmospheric boundary layer over the Southern Ocean in response to the synoptic forcings	Published	70% Concept, processing data and writing drafts	1) Yi Huang, concepts and writing 15% 2) Steven T. Siems, concepts and writing 10% 3) Michael J. Manton, revision 5%	No

I have renumbered sections of submitted or published papers in order to generate a consistent presentation within the thesis.

Student signature: Date: September 17, 2018

The undersigned hereby certify that the above declaration correctly reflects the nature and extent of the student's and co-authors' contributions to this work. In instances where I am not the responsible author I have consulted with the responsible author to agree on the respective contributions of the authors.

Main Supervisor signat   Date: September 17, 2018

Acknowledgments

First of all, I would like to acknowledge the National Commission for Scientific and Technological Research (CONICYT) for supporting my PhD through "Becas Chile" Doctoral Fellowship program.

The competition of this thesis would not been possible without the support of many people. Firstly, I would like to thank my main supervisor Steven Siems, who I have had the great fortunate to work with over the past four years. Your guidance and patience during my candidature are priceless. Thank you for always supporting me to attend conferences, workshops and field campaigns. These have given me an invaluable experience as a researcher.

I am also especially grateful to my co-supervisor Yi Huang. Definitely, you are one of the smartest people I had the opportunity to meet over my PhD. Thank you for your insightful comments and suggestions along the way. Thanks must also be given to my co-supervisor Danijel Belušić for the guidance and patience. I would also like to give special thanks to Michael Manton. I greatly appreciate the help and advice you have provided me over the years.

To all my former colleagues in my research group at Monash University. I really appreciated all your constructive comments and support over the course of my PhD.

To my family and friends in Chile, thank you for your constant source of love and support from the distance. In particular, both of my parents supporting me throughout my PhD. Thanks to Carla, Stephanie and Emanuel, my best friends in Melbourne, for making my life in Australia a lot more enjoyable.

Finally, mostly of all, to my best friend and life partner, María José. I would have not been able to complete this thesis without your love and support. Thank you for accompanying me so far from our lives in Chile. And thank you for sharing the good times, and for tolerating me during the hard times. This thesis is dedicated to you.

Contents

List of Figures

List of Tables

Abbreviations

ABI	Advanced Baseline Imager
ABL	Atmospheric Boundary Layer
ACCESS	Australian Community Climate and Earth-System Simulator
ACE-1	Aerosol Characterization Experiment
ACM2	Asymetric Convective Model version 2
AHI	Advanced Himawari Imager
BASTA	Bistatic Radar System for Atmospheric Studies
CAPRICORN	Clouds, Aerosols, Precipitation, Radiation, and atmospherIc Composition Over the southeRn oceaN Project
CASES-99	Cooperative Atmosphere-Surface Exchange Study
CTP	Cloud-Top Phase
CTT	Cloud-Top Temperature
ECMWF	European Centre for Medium Range Weather Forecasts
EIS	Estimated Inversion Strength
ERA-Interim	ECMWF Re-Analysis Interim
EZ	Entrainment Zone
FLOSSII	Fluxes Over Snow Surfaces II
GCM	Global Circulation Model
GPCP	Global Precipitation Climatology Project
LCL	Lifting Condensation Level
LST	Local Standard Time
LTS	Lower Troposphere Stability
MABL	Marine Atmospheric Boundary Layer
MAC	Macquarie Island Station
MARCUS	Measurements of Aerosols Radiation Clouds over the Southern Oceans
MCC	Mesoscale Cellular Convection
MCSM	Modeling, Analysis, and Prediction (MAP) Climatology of Midlatitude Storminess
MERRA	Modern-Era Retrospective Analysis for Research and Applications
ML	Mixed Layer
MSLP	Mean Sea Level Pressure
MYJ	Mellor-Yamada-Janjic

NESDIS	National Environmental Satellite, Data, and Information Service
NOAA	National Oceanic and Atmospheric Administration
NWP	Mesoscale Numerical Weather Prediction Model
PBL	Planetary Boundary Layer
RL	Residual Layer
RLW	Relative Fraction of Liquid Water to Total Water
RRTMG	Rapid Radiative Transfer Model for GCMs
SAS	Simplified Arakawa-Schubert
SL	Surface Layer
SLW	Supercooled Liquid Water
SO	Southern Ocean
SOCEX	Southern Ocean Cloud Experiments
SOCRATES	Southern Ocean Cloud Radiation and Aerosol Transport Experimental Studies
SST	Sea Surface Temperature
T-AMIP2	Transpose-Atmospheric Model Intercomparison Project II
UTC	Coordinated Universal Time
WDM6	WRF Double-Moment 6-class
WRF	Weather Research and Forecasting Model
WSM5	WRF Single-Moment 5-class
YSU	Yonsei University

Chapter 1

Introduction

1.1 The Atmospheric Boundary Layer

The atmospheric boundary layer (ABL) or planetary boundary layer (PBL) supports multiple definitions according to the characteristics that are highlighted. Kaimal and Finnigan (1994) describe the ABL as "the lowest 1-2 km of the atmosphere, the region most directly influenced by the exchange of momentum, heat, and water vapor at the Earths surface". Nieuwstadt and Duynkerke (1996) define it as "the region where meteorological variables (wind velocity, temperature and humidity) adjust from their values in the free atmosphere to the boundary conditions at the ground". However, different definitions might entail a certain ambiguity or generality in the description of its characteristics. Stull (1988) instead defines it as the portion of the atmosphere most affected by the surface of Earth and that responds to surface forcings with a timescale of about an hour or less; such forcings include friction or surface drag, evaporation, heat transfer and emission of pollutants, among others. Above this layer, there is an upper layer which is referred to as the free atmosphere. The range of thickness or depth of the boundary layer is quite variable in space and time, from one hundred meters to few kilometers, depending on the forcings (Stull 1988). The main idea that underlies all these definitions is the common turbulent state of atmospheric flow, and its effect on the behaviour and evolution of the atmosphere.

Turbulence and static stability generates a strong stable layer with a capping inversion, which defines a limit between the ABL and the free atmosphere or free troposphere.

The capping inversion maintains moisture, turbulence and pollutants within the ABL and prevents most of the surface friction from affecting the free atmosphere (Stull 2017).

1.1.1 Turbulence and Scales

The mixing within the atmosphere is closely related to the turbulent characteristics of near-surface flow due to the non-linearity of the processes governing its dynamics. Turbulence is defined as a complex superposition of many different scales of motion, consisting of a superposition of swirls called eddies that interact to create quasi-random, chaotic motions (Stull 1988).

Turbulence plays a significant role on the development and evolution of ABL depth over space and time scales (Panofsky and Dutton 1984) ranging from planetary-scale circulations or large-scale waves (several hours of duration) to turbulence scale with small eddies (few seconds of duration) (Mahrt 2014; Stull 1988).

The spectrum of wind speed is shown in Fig. 1.1a, the y-axis represents a measure of the portion of turbulence kinetic energy (TKE) that is associated with a particular size eddy; and the x-axis gives the eddy size in terms of the time period and frequency of the wind-speed variation (Van der Hoven 1957). Small eddies have shorter timescales than larger eddies, the peaks indicates the largest contributions to TKE (Stull 1988). The first peak on the left corresponds to the variations in wind speed associated with the passage of fronts and meteorological systems; the second peak responds to the growth of the wind speed during the day and its decrease during the night; and the last peak, located on the right, corresponds to the microscale.

TKE is not conserved and is continually dissipated into internal energy by molecular viscosity (Fig. 1.1b). This dissipation usually happens at only the tiniest eddies (microscale), but it affects all turbulent scales because of the turbulent cascade of energy from larger-size to smaller eddies (Stull 2006).

1.1.2 Sublayers of ABL and Diurnal Cycle over Land

Figure 1.2 shows the diurnal evolution of the ABL during summer over land under fair-weather and cloud-free conditions (Stull 1988). The ABL can be divided into different

(a)

(b)
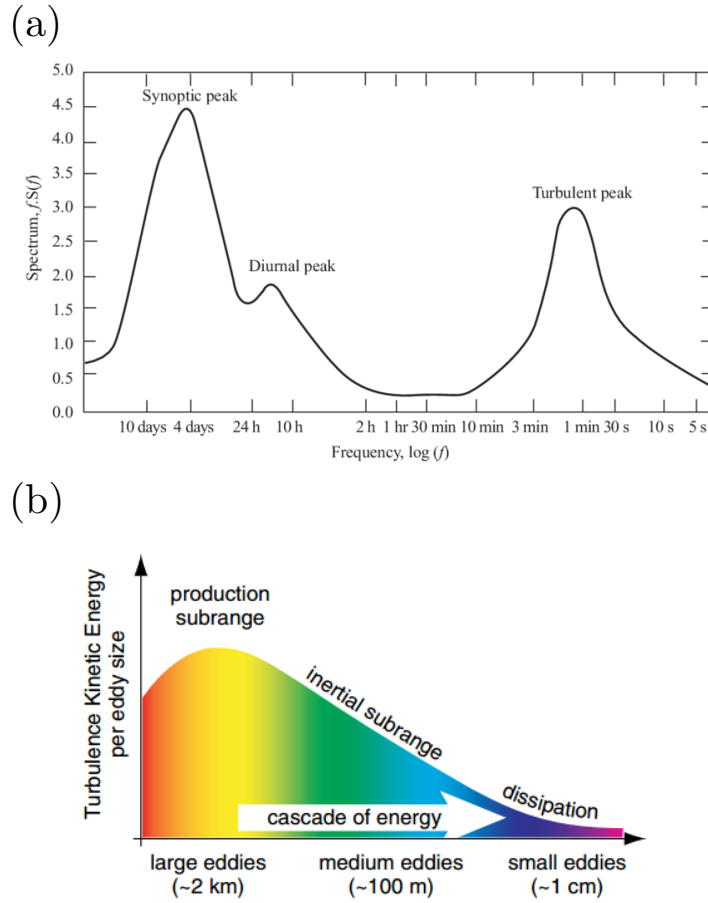
Figure 1.1: (a) The spectrum of turbulence kinetic energy (Van der Hoven 1957) and (b) the turbulence kinetic energy cascades (Stull 2006).
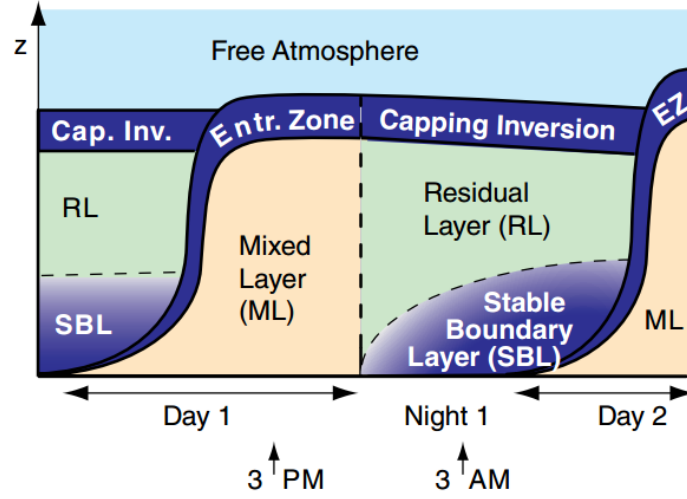
Figure 1.2: The diurnal cycle of ABL during fair weather over the land (from Stull 2017).

sublayers during fair weather conditions over land: a very turbulent mixed layer (ML), also known as the convective boundary layer, a less turbulent residual layer (RL) containing former mixed-layer air, a stable boundary layer (SBL), the entrainment zone (EZ) and surface layer (SL) (Stull 2017).

After sunrise, the warmed surface heats the air and causes turbulent eddies to develop. These eddies rise and create the ML, where meteorological quantities such as potential temperature and water vapor mixing ratio are quite uniform. Above the ML, the EZ is a stable layer, where there is a sharp temperature increase at the layer top and the temperature gradient suppresses the turbulence mixing. In the EZ, free-atmosphere air is incorporated into the mixed layer through a process called entrainment, causing the ML depth to increase during the day (Stull 2017). At the sunset, longwave radiation cools the surface and creates the SBL, which is a shallow stable layer of air that is in direct contact with the ground. Above the SBL layer, a RL is the left over part of the ML. Finally close to the ground, the SL is the lower part of ABL. In this layer, the winds, temperature and humidity vary rapidly with altitude, and the characteristics of turbulence are affected by the surface. The turbulent fluxes in the SL are approximately constant with height (Stull 1988).

1.1.3 Surface Forcings and Energy Budget

As discussed above, the exchange of heat and moisture between the surface and overlying atmosphere is responsible for the diurnal variations in ABL. In this sense, heat fluxes from the surface play a major role in generating boundary layer turbulence (Markowski and Richardson 2010). It is through the energy budget at the surface that heat and moisture fluxes are tied to the net radiation received at the ground.

The surface receives during the day predominantly short-wave solar radiation, where the amount absorbed by the surface depends on the cloud fraction, solar angle, and surface albedo. Further, the ground also receives long-wave radiation emitted by clouds and the atmosphere. The earth's surface, on the other hand, also emits radiation at long wavelengths. The net radiation (R_n) is the difference between the incoming short-wave and long-wave radiation and the outgoing long-wave radiation. In addition to the radiative fluxes at the surface, the fluxes of sensible and latent heat also need to be taken into account (Markowski and Richardson 2010; Stull 1988). Therefore, the surface energy budget, that is, the relationship between the R_n and the sensible (Q_h), latent (Q_e), and ground heat (Q_g) fluxes, can be expressed as

$$R_n = Q_h + Q_e + Q_g, \tag{1.1}$$

where R_n is defined to be positive when incoming radiation exceeds outgoing radiation, and the heat fluxes are defined to be positive when directed away from the surface (i.e., Q_h and Q_e are positive when upward directed, and Q_g is positive when downward directed). Figure 1.3 shows the direction of the fluxes during day and night in fair weather conditions with light to calm winds over land.

1.2 The Stable Boundary Layer

The SBL forms when the solar heating ends and the bottom parts of the RL is transformed by its contact with a quickly cooling of the ground, inducing a positive vertical temperature gradient, which generates a SBL (Stull 1988). The cooling process typically begins an hour or two before sunset, once the incoming solar radiation is lower than the
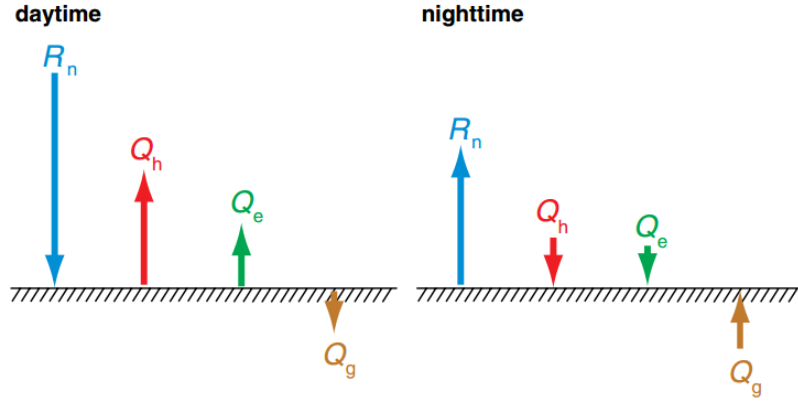
Figure 1.3: Schematic representation of the surface energy budget during daytime and nighttime (from Markowski and Richardson 2010) .

net long-wave radiative cooling (Mahrt 2014).

Despite its prevalence and significance, the SBL has evaded proper theoretical description for decades. Even less understood are the very stable conditions that occur when winds are weak (e.g., Sun et al. 2013). Under very stable conditions, the turbulence is highly intermittent and is associated with non-stationary processes (Sun et al. 2015a). Small-scale non-turbulent motions, such as gravity waves and horizontal meandering, govern the environment (Vickers et al. 2008). The turbulent motions in the very stable ABL are characterised by (a) quite small correlations between vertical velocity fluctuations and scalars compared to traditional turbulence (Mahrt et al. 2012); (b) horizontal motions with weak vertical velocity fluctuations and constrained vortex stretching (Mahrt 2014); and (c) relatively large temperature fluctuations, which can be posed in terms of exchanges between available potential and TKE (Mahrt 2014; Winters et al. 1995).

The range of turbulence scales is highly dependent on stability, as the stability increases, the range decreases (Fig. 1.4). Under very stable environments, it is difficult to differentiate a clear separation between turbulence and waves, and an intermediate range of scales appears to have characteristics between those of turbulence and non-turbulent motions. Figure 1.4 shows two additional categories between the traditional mesoscale and turbulence scales. The first category is called submeso and is defined in various ways, the term submeso generally includes the complex mix of motions on scales between the main turbulent eddies and smallest mesoscale motions, traditionally specified to be about 2 km horizontal scale (Mahrt 2014). Mahrt (2014) defines an additional category between

(a)

(b)
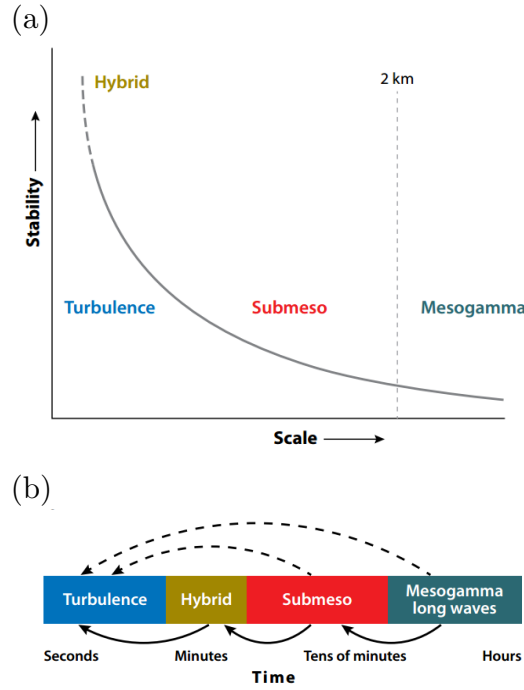
Figure 1.4: Boundary layer regimes defined by Mahrt (2014): (a) The basic regimes in stability-scale space. (b) The solid arrows indicate downscale energy flow and the dashed arrows represent short-circuiting of the energy flow directly from larger scales to the turbulent scales.

turbulence and submeso motions, called hybrid, which includes modes with intermediate characteristics and the superposition of turbulent and non-turbulent modes that overlap in timescale.

1.2.1 Submeso Motions

Submeso motions exist under all atmospheric conditions, but are very important when the mean flow is weak, as they then can become the dominant motion patterns (Cava et al. 2016; Mortarini et al. 2016; Vickers et al. 2008). This is a broad definition and considers processes with different physical origins that may coexist in the nocturnal ABL (Acevedo et al. 2014). The high variability of submeso processes seems to be influenced in a complex way by local surface features, such as terrain and vegetation (Monti et al. 2002; Vickers and Mahrt 2007).

Based on numerical studies, laboratory experiments and theoretical considerations, the perturbation flow is partitioned into turbulence, two-dimensional modes[*], and propa-

---

[*]Primarily horizontal motions in the strongly stratified boundary layer with negligible vertical motion and minimal vertical coherence, but often with significant vertical vorticity (Mahrt 2014).

gating waves (e.g. gravity waves), in which the latter two categories are usually considered as submeso motions (Mahrt 2014). Two dimensional modes have been produced in a laboratory enviroment and numerically simulated and are characterized by significant vertical coherence (Billant and Chomaz 2000). However, such vertically coherent modes have been difficult to identify from atmospheric data (Mahrt 2009). Propagation waves are also common in the stable boundary layer, and they are associated with a wide variety of scales (Mahrt 2014). Gravity waves are less clearly defined near the surface due to weak vertical motions and involve a complex variety of generating mechanisms. These mechanisms includes overlying critical levels, reflection at the surface and ducting in the nocturnal boundary layer.

1.3 The Marine Atmospheric Boundary Layer

The marine atmospheric boundary layer (MABL) is defined as the portion of the troposphere directly influenced by the presence of the ocean's surface. The MABL plays an important role in controlling the transfer of energy and moisture from the ocean to the free atmosphere (Kloesel 1989). Over the oceans, where low-level clouds are dominant (stratus and stratocumulus), the depth of the MABL varies relatively slowly in space and time because the ocean has a much larger heat capacity than the land, which allows it to absorb and store solar energy during the day and release it at night. This produces nearly constant ocean surface temperatures over the diurnal cycle (Garratt 1994; Stull 2017). Cold-air advection over the oceans contributes to the maintenance of stratiform cloud decks. When cold-air masses are advected over a relatively warm ocean, the surface layer is destabilised and the flux of water vapor from the sea surface is enhanced. In addition, cold-air advection leads to shallow convection in the MABL (Stull 2006).

In the MABL, the latent heat flux is higher in relation to sensible heat due to evaporation over the sea surface. Further, when stratocumulos-topped boundary layer are dominant, the surface latent heat flux provides the main source of moisture (Wood 2012). Over warm oceans, in well-mixed stratocumulos-topped boundary layer, the surface latent heat flux is an important source of buoyant TKE production (Bretherton and Wyant 1997).

The two major factor that influence the MABL clouds are solar radiation and precipitation. When solar radiation is absorbed by droplets, a local source of heating is generated, and distributed into the clouds, while the cloud-top is cooling. This heating-cooling process provides a source of local convection and turbulence that is restricted in the vertical by the overlying temperature inversion. However, solar heating reduces convective turbulence near cloud top by offsetting cloud-top cooling (Boers 2001). Overall, a reduction in convective turbulence is found due to the effect of solar heating, reducing entrainment (Boers 1995). This reduction in convective turbulence means that a deep boundary layer cannot be maintained and the cloud layer decouples from the lower surface layer. Because the moisture supply into the cloud is interrupted, the cloud cover becomes broken. The effect of precipitation is similar to that of solar radiation. Precipitation produces that the sub-cloud layer cools due to evaporation, which also suppresses turbulence and a well-mixed layer can not be maintained (Boers 2001; Bretherton and Wyant 1997; Jones et al. 2011; Nicholls 1984).

Decoupled boundary layers are a common observation of the low-level MABL clouds and have been observed in the sub-tropical trade wind cumulus regime since the late 1940s (Boers 2001). Nicholls and Leighton (1986) described for the first time decoupled stratocumulus layers at the top of the MABL in mid-latitudes.

1.4 The Marine Atmospheric Boundary Layer over the Southern Ocean

The clouds over the Southern Ocean (SO) are commonly located within the lowest kilometer above the ocean surface (i.e. within MABL) (Huang et al. 2012a). These low-level clouds offer a significant contrast in the albedo to the underlying ocean surface (Huang et al. 2012b).Because the absence of any land at the surface, the clouds and the dynamics of the MABL over the SO offer many contrasts with those observed over the Northern Hemisphere (Huang et al. 2015). Haynes et al. (2011) identified that the lack of low-level clouds by models is the major cause of bias in the absorbed shortwave radiation over the SO, due to the net radiative budget is highly sensitive to the thermodynamic cloud-

phase tops. Further, Bodas-Salcedo et al. (2012) highlight the importance these bias in simulation of stratocumulus and mid-top clouds in a post-frontal air mass.

1.4.1 SO Storm Track

The meteorology of the SO is commonly defined by the SO storm track (Simmonds and Keay 2000). The storm track is characterized by a high density of extra-tropical cyclones and fronts (e.g., Hoskins and Hodges 2005; Simmonds and Keay 2000). Low-altitude clouds are commonly present in pre- and post-frontal environments between fronts (Haynes et al. 2011), which dominate the energy budget over the SO (Mace 2010). Jimi et al. (2007) found that fronts passed over Tasmania with a frequency of roughly twice a week during winter and slightly less during summer. In summer, the storm track is commonly present between 40°S and 60°S, whereas in winter, the storm track is more asymmetric with a spiral around the Antarctica and an outer spiral in the sector of the strong subtropical jet (Hoskins and Hodges 2005).

1.4.2 Observations over the SO

1.4.2.1 Past Field Campaigns

Comprehensive field experiments with in situ observations of the MABL and low-elevation clouds over the SO have generally been limited to relatively sparse and isolated field campaigns. The Aerosol Characterization Experiment (ACE-1, Bates et al. 1998) in November and December of 1995 was the first of a series of experiments to observe the evolution of the pristine aerosol chemistry within the boundary layer. During ACE-1, Russell et al. (1998) described a unique layer between the MABL and the overlying free troposphere. They called this layer "buffer layer", which was found to be up to 1000 m deep, deeper than the MABL ($\sim$600 m deep). Further, this buffer layer was found to be transient in nature with partial cloud cover and strong wind shear commonly observed at its boundaries and even within it (Wang et al. 1999). The Southern Ocean Cloud Experiments (SOCEX I and II, Boers et al. 1998) studied the seasonal variability of microphysical and radiative properties of the clouds over the SO. During SOCEX, Jensen et al. (2000) defined an "intermediate layer" within the MABL, which contained a high
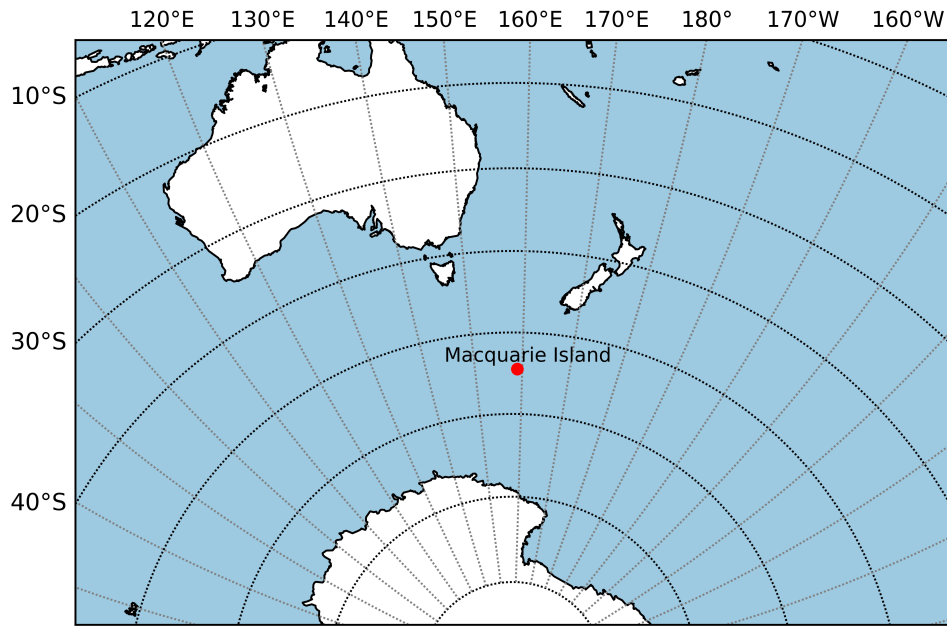
Figure 1.5: Map showing the location of Macquarie Island, Australia, New Zealand and Antarctica.

fractional cloud cover. This intermediate layer was most unique in that the winds through the layer were at a heading of 320° (northwesterly) while the winds both above and below the layer were at a heading of 290° or less.

1.4.2.2 Macquarie Island Observations

Macquarie Island is a small and remote sub-antarctic island situated in the midst of the SO (54.62°S, 158.85°E), approximately half way between Australia and Antarctica (Fig. 1.5). A station is maintained by the Australian Antarctic Division since 1948, with a rich, quality record of both surface and upper air observations. The island was included on the World Heritage list in 1997 to highlight its importance as an environment with a unique natural diversity. Further, Macquarie Island also plays an important role in understanding the planetary weather and climate as one of the few places in this region with a dedicated meteorological station. Standard surface observations are recorded along with twice-daily upper-air soundings and hourly surface records. The launch site of soundings is at an elevation of 8 m above sea level and has direct exposure to the prevailing westerly winds (Wang et al. 2015).

The island is a north-south oriented isthmus close to sea level, about 34 km long and 5 km wide (Jovanovic et al. 2012). The average elevation of the island is around 100-200

m, and the highest point on the island is in the south, and extends to about 410 m (Hande et al. 2012a; Wang et al. 2015)

Recent studies over the SO have reflected on the importance of the observations recorded at Macquarie Island in helping develop an understanding of the atmospheric conditions over the SO. For instance, Adams (2009) examined the trends over the period from 1971 to 2008 in the surface observations. They highlight a 35% increase in the annual precipitation at Macquarie Island due to an increase in cyclonic activity. These strong trends were not evident in the European Centre for Medium-Range Weather Forecasts (ECMWF) ERA-40 reanalysis.

Hande et al. (2012a) employed the upper-air soundings at Macquarie Island to analyse the thermodynamic structure of the MABL. They identified systematic biases in ECMWF operational analysis, noting discrepancies in the inversion height, boundary layer wind shear and boundary layer decoupling. They found that the "buffer layer" occurs 33.7% of the time in Macquarie Island soundings. Huang et al. (2012b) used the upper-air soundings over Macquarie Island to compare against both CloudSat and raDAR/liDAR MASK products (Delanoë and Hogan 2008; Huang et al. 2012b). They found that the satellite products underestimate the fraction of boundary layer clouds in the lowest kilometer of the ABL, likely due to a surface clutter contamination. Wang et al. (2015) analyzed the climatology of the precipitation over Macquarie Island and found that a majority of the surface precipitation is relatively weak and arrives predominantly from the west. They estimated that the average annual Macquarie Island precipitation (1,023 mm) was 6.8% greater than that from ERA-Interim (953 mm) from 1979 to 2011.

Macquarie Island is located on the Southern Hemisphere storm track, which is an ideal place to experience a variety of synoptic conditions (Simmonds and Keay 2000; Streten 1988).

1.4.2.3 CAPRICORN Project

The Clouds, Aerosols, Precipitation, Radiation, and atmospherIc Composition Over the southeRn oceaN (CAPRICORN) project phase I was conducted from 14 March to 16 April 2016. The project is part of a broader SO strategy to characterize cloud-aerosol-

precipitation processes, representing an important contribution of uncertainties in future climate projections (Bodas-Salcedo et al. 2014). The scientific goals of CAPRICORN are to: (i) characterise the cloud, aerosol, and precipitation properties, boundary layer structure, atmospheric composition, and surface energy budget, as well as their latitudinal variability; (ii) evaluate and improve satellite estimations of these properties, and (iii) evaluate and improve the representation of these properties in the Australian Community Climate and Earth-System Simulator (ACCESS) regional and global model. The ship R/V Investigator traversed a large area of the SO, with observations between latitudes from 43°S to 53°S and longitudes from 141°E to 151°E. A wide variety of meteorological conditions were encountered during the experiment, which are very typical of this region such as cold fronts, warm fronts and mid-latitude cyclones. The large-scale frontal systems observed in the area allowed for the sampling of pre-frontal, frontal, and post-frontal clouds over the period. The number of fronts registered corresponds to the typical frequency of front passages of about one every three days as described in the climatology of SO fronts from Berry et al. (2011).

1.4.3 Thesis Structure and Research Aims

The following chapters of this thesis describe the ABL at different scales, with a focus on the largest contributions to TKE according to the Fig. 1.1a, at synoptic, daily and turbulent scales.

The aims of this thesis are summarised by chapter as follow:

Chapter 2

The main objective of this chapter is to examine submeso variability and large sudden wind-direction shifts in the nocturnal boundary layer by using a micrometeorological network. The characteristics of the horizontal propagation of motions causing the wind-direction shift have not been addressed in previous studies.

This research has been published by Boundary-Layer Meteorology.

Chapter 3

In this chapter the role of synoptic meteorology on the thermodynamic structure of the MABL over the SO is examined using upper-air soundings and surface precipitation at Macquarie Island, with a primary focus on the post-cold-frontal environment. Thermodynamic profiles from the ECMWF ERA-Interim reanalyses are compared with the observations to evaluate their representation of the MABL characteristics.

This research has been published by Journal of Geophysical Research: Atmospheres.

Chapter 4

An extension of the research in Chapter 3 is presented. Surface observations and upper-air soundings at Macquarie Island are used to identify the diurnal cycle of the precipitation and analyze its relationship with the MABL at this site. Further, a comparison between the in-situ observations and those produced by the ECMWF ERA-Interim reanalyses is made. The intraseasonal variability is examined to further reveal its nature. Specific features from the diurnal cycle of precipitation may help to understand physical and/or dynamic mechanisms of the MABL over the SO.

This work will be submitted for publication in the very near future.

Chapter 5

The objective of this chapter is to evaluate the Weather Research and Forecasting (WRFV3.9.1) mesoscale numerical weather prediction (NWP) model in simulating a frontal passage and the post-frontal clouds over Tasmania and the SO with shipborne observations from CAPRICORN Project and Himawari-8 satellite products. Two study cases are simulated and evaluated, with a focus on shallow convective clouds and frontal

passages. The simulated meteorological times series, thermodynamic boundary layer structure, cloud cover, cloud-top phase and cloud-top temperature are compared with the observations. Sensitivity experiments with different physical parameterization schemes are performed to investigate the impact of boundary layer and microphysical processes on the simulations of the shallow convective clouds.

Chapter 6

A succinct summary of key conclusions from the previous chapters is presented.

Chapter 2

Observations of Wind-Direction Variability in the Nocturnal Boundary Layer[*]

2.1 Introduction

Over land under nocturnal conditions and relatively clear skies, the net radiative cooling of the ground induces a positive vertical temperature gradient, which generates a stable atmospheric boundary layer (ABL) (Mahrt 2014). Even with the prevalence of the stable ABL, and the existence of many studies that have examined its behaviour, the knowledge of fundamental features remains incomplete (Sun et al. 2015b). The behaviour of turbulent and non-turbulent motions in the stable ABL is not well described by the classical theories of the ABL, and this lack of understanding increases with stability (Acevedo et al. 2014; Grachev et al. 2005; Kang et al. 2015; Mahrt 2014; Vercauteren and Klein 2015).

The very stable ABL does not categorically satisfy traditional definitions of turbulence (Mahrt 2014). Under very stable conditions, the turbulence is highly intermittent and is associated with non-stationary processes (Sun et al. 2015b), and small-scale non-turbulent motions govern the environment (Vickers et al. 2008). In this regard, the turbulence time and length scales may be restricted to very small values; in very stable conditions, the turbulent processes may have an upper time scale limit of between 5 and 10 s (Acevedo et al. 2014). Such small time scales relate to a spectrum of generally unknown motions,

which separate turbulence scales from the mesoscale (Belušić and Mahrt 2012; Vercauteren et al. 2016). Motions in this range have been termed submesoscale (or submeso) and are loosely defined as non-turbulent atmospheric motions on scales larger than seconds, but smaller than those traditionally classified as mesoscale (Acevedo et al. 2014; Belušić and Mahrt 2008; Sun et al. 2015b). Such a loose definition could be given in terms of space scales, although there is a general understanding that submeso motions do not follow the Taylor hypothesis, and knowledge of them derives from point measurements. Submeso motions exist under all atmospheric conditions, but are very important when the mean flow is weak (Cava et al. 2016; Mortarini et al. 2016; Vickers et al. 2008). With low wind speeds they become the dominant motion pattern, produce sudden and large wind-direction shifts, and influence mixing and fluxes of scalars and momentum. The above definition is broad and considers processes with different physical origins that may coexist in the nocturnal ABL (Acevedo et al. 2014). The high variability of submeso processes seems to be influenced in a complex way by local surface features, such as terrain and vegetation (Monti et al. 2002; Vickers and Mahrt 2007).

Only a few studies have analyzed abrupt and large wind-direction shifts under stable conditions. Mahrt (2007, 2008) analyzed wind-direction variability from different field experiments, and found that changes in wind direction at low wind speeds are more often abrupt shifts rather than gradual meandering of the wind vector. These studies conclude that abrupt changes in wind direction are associated with a wide variety of phenomena and are not systematically related to changes in turbulence intensity or changes of other variables, except for a slight tendency for the development of larger wind-direction shifts with the passage of cold microfronts.

Since sudden wind-direction shifts occur predominantly with low wind speeds, and are prone to high concentrations of atmospheric pollutants due to low mixing and ventilation (Vickers et al. 2008), they may have a considerable impact on air quality. However, sudden submeso wind-direction shifts are currently not reproduced or parametrized in numerical models (Belušić and Güttler 2010; Güttler and Belušić 2012; Suarez et al. 2015), and an understanding of their generation remains incomplete (Mahrt 2008). Some of the ubiquitous problems related to modelling the stable ABL in numerical weather prediction

and climate models (e.g., Sandu et al. 2013) may be related to the absence of a treatment of submeso processes. Mahrt (2014) specifically identified the parametrization of change of wind direction as a challenge in the simulation of horizontal dispersion.

The main goal of our study is to examine submeso variability and large sudden wind-direction shifts under nocturnal conditions using a micrometeorological network of stations. The network allows us to characterize the horizontal propagation of events causing the wind-direction shifts, which has not been addressed previously. We attempt to answer the following questions:

- Can we confirm that the submeso wind-direction variability is related to local terrain characteristics?

- Are submeso motions advected by, or at least related to, the local mean flow?

- Can we gain any insight into their spatial scales from point observations?

- Hence, could submeso motions be parametrized locally?

The paper is structured as follows: the dataset, study area and methods are described in Sect. 2.2, and the general statistics of submeso motions are presented and compared with other field experiments in Sect. 2.3. Section 2.4 analyzes the characteristics and effects of large sudden wind-direction shifts, and in Sect. 2.5, the horizontal propagation of events causing wind-direction shifts is estimated and compared to the mean flow. Section 2.6 provides conclusions.

2.2 Data and Methods

2.2.1 Data

The field experiment was designed to characterize the submeso motions that are not generated by terrain or surface heterogeneity, to the maximally achievable extent considering the ubiquitous heterogeneity of the land surface. The wind and temperature data were collected from a micrometeorological network composed of four towers that form an equilateral Y-shaped horizontal array with a radius of 580 m (Fig. 2.1), positioned within a
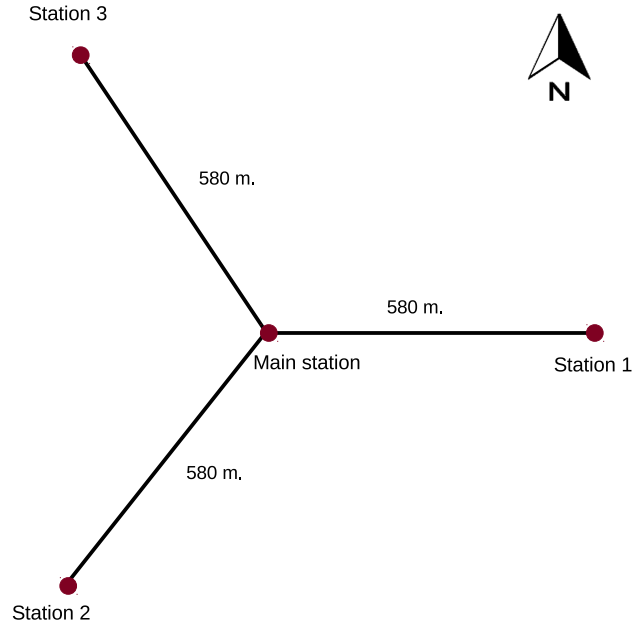
Figure 2.1: The schematic of the micrometeorological network in north-western Victoria, Australia.

large area with predominantly homogeneous and flat terrain in north-western Victoria, Australia. The terrain has a small slope towards the south (less than 0.05% within 10 km around the network). In addition, there is a 20-m high hill approximately 15 km north-east of the network, and a 30-m high hill about 30 km to the south-west. The horizontal network of high-resolution measurements was designed to cover the typical range of horizontal scales of submeso structures in the ABL.

The main tower was located at the centre of the network (main station; 35° 52′ 5.89″S, 143° 20′ 35.96″W). It was instrumented with a three-dimensional Campbell Scientific CSAT3 sonic anemometer at 3 m above the ground sampling at 10 Hz, and slow response wind and temperature sensors at 6 m above the ground sampling with a 1-min interval. The three satellite towers were instrumented with two-dimensional Gill WindSonic sonic anemometers at 3 m above the ground sampling at 4 Hz. The three-dimensional sonic data were tilt-corrected using the planar fit method (Wilczak et al. 2001).

The experiment was conducted from 23 March 2013 to 25 January 2015; however, the main station only operated from 23 March 2013 to 19 June 2013 due to technical problems. Since only the main station was equipped with a three-dimensional anemometer, we focus the analysis on the latter shorter period, except when specifically noted otherwise.

Following similar analysis in Mahrt (2008), the data between 2000 LST and 0800 LST the next day were used for the analysis in order to remove daytime conditions.

2.2.2 Methods

We use three different methodologies for investigating the submeso motions and wind-direction variability: a bulk approach analyzing the statistics of the entire dataset, an approach based on extracting all individual structures that cause large and sudden wind-direction shifts, and finally an analysis of the propagation of these structures.

2.2.2.1 Submeso Motions

Two measures of submeso motions are used here to compare our field experiment with previous studies, corresponding to: the cross-wind velocity variance and the mesovelocity scale.

The contribution to the cross-wind velocity variance from submeso motions is a typical measure of the plume spread, and we use the method of Vickers and Mahrt (2007) to calculate the cross-wind velocity variance. They defined this as the difference between the total variance at averaging time scale τ and the variance due to turbulent motions alone. For the purpose of comparison with Vickers and Mahrt (2007), the coordinate system was rotated such that the 4-h average v-component was zero, in order to obtain the cross-wind component. With the same purpose, the contribution of turbulent motions was fixed to the scale of 5 min, and different time scales τ used to calculate the velocity variance are shown in Table 2.1. As discussed in Vickers and Mahrt (2007) and Mahrt (2008), the final statistics depend strongly on the choice of averaging time, which is why we closely repeated their procedure.

A measure of the strength of the submeso flow, called the mesovelocity scale, is defined by Mahrt (2007) as

$$V_{meso} \equiv \left[\left(\tilde{v}^2 + \tilde{u}^2 \right)^{1/2} \right], \tag{2.1}$$

where the tilde indicates the deviations of 1-min averages from the 1-h record average and the brackets refer to averaging over the 1-h record (Mahrt 2008). The choice of 1 min as

Table 2.1: Mean (standard deviation in parenthesis) of the log base 10 of the submeso cross-wind velocity variance (m^2 s^{-2}) for averaging times τ of 15, 60 and 240 min. The values from Vickers and Mahrt 2007 for FLOSSII and CASES-99 are included for comparison.

Site	Class	15	60	240
Victoria	Weakly stable	$-1.43(0.34)$	$-0.85(0.39)$	$-0.44(0.46)$
	More stable	$-1.52(0.31)$	$-0.98(0.34)$	$-0.67(0.38)$
FLOSSII	Weakly stable	$-0.76(0.41)$	$-0.21(0.45)$	$0.17(0.48)$
	More stable	$-0.85(0.34)$	$-0.34(0.33)$	$-0.04(0.36)$
CASES-99	Weakly stable	$-1.46(0.46)$	$-0.99(0.40)$	$-0.59(0.47)$
	More stable	$-1.71(0.38)$	$-1.13(0.42)$	$-0.71(0.44)$

the time scale is thoroughly discussed in Mahrt (2007). Note that although this measure is originally termed the mesovelocity scale, it may refer to submeso scales given the loose definition of submeso used above. In addition, the relative strength of the submeso flow is defined as

$$RV_{meso} = \frac{V_{meso}}{V},\tag{2.2}$$

where V is the 1-h average wind speed. According to Mahrt 2007, wind-direction statistics can be related to RV_{meso}, and it was shown for the Fluxes Over Snow Surfaces II (FLOSSII) experiment that maximum wind-direction shifts increase with increasing RV_{meso} (Mahrt 2008). Values of $RV_{meso} > 1$ indicate a significant influence of submeso motions on the total velocity vector, yet $RV_{meso} < 1$ might still indicate important contributions from submeso motions.

2.2.2.2 Wind-direction Shifts

Wind-direction variability is analyzed through sudden changes of wind direction, changes that are very common under low wind speeds in the stable ABL (Mahrt 2010). Wind-direction shifts are defined as the difference between the subsequent 1-min wind direction and the previous 1-min wind direction, implying that the differences are centred across 2-min intervals

$$\Delta WD_i = WD_{i+1} - WD_{i-1}\tag{2.3}$$

where $\Delta WD_i \in [-180, 180]$. Mahrt (2008) notes that the variability of the wind direction

decreases as the averaging length increases and the smallest submeso motions are eliminated. In order to detect large sudden shifts from the time series, we define "events" at the main station as $\Delta WD > 60°$. To analyze how these events are related to other variables before and after the wind-direction shift, we define time windows or sampling windows centred around the events. Different lengths of sampling windows were tested, and the length of 20 min (10 min before and after the events) was chosen as best suited for our goals. This sampling length also provides a sufficient number of points to study the propagation of structures (see the following sub-section). Sampling windows are extracted from the time series through an iterative process, and the first extracted sample is centred around the largest ΔWD within the entire dataset. Wind-direction shifts within this sampling window are then removed from further iteration. The next sample is centred around the largest ΔWD in the remaining dataset, and so on. Since a sampling window can contain more than one event, the number of sampling windows is smaller than the number of events.

2.2.2.3 Propagation of Structures

We use the 20-min sampling windows surrounding wind-shift events to study the propagation of structures. The method for propagation is based on the cross-correlation function method (Rees and Mobbs 1988), which calculates the speed and direction of propagation between any three meteorological stations in a triangle. Given the stations 1, 2 and 3 with coordinates (x_1, y_1), (x_2, y_2) and (x_3, y_3), and time lags τ_{12}, τ_{13} and τ_{23}, respectively, assuming a disturbance with inverse period f passing through the three stations, the following relationships for the inverse horizontal wavelengths (k, ℓ) hold (Rees and Mobbs 1988)

$$kx_1 + \ell y_1 = kx_2 + \ell y_2 - f\tau_{12} \tag{2.4}$$

$$kx_1 + \ell y_1 = kx_3 + \ell y_3 - f\tau_{13} \tag{2.5}$$

Equations 2.4 and 2.5 can be solved for k and ℓ, hence the speed v_p and direction α of propagation can be determined (Monserrat and Thorpe 1992). Therefore

$$k = \frac{f\left\{\tau_{12}\left(y_1 - y_3\right) - \tau_{13}\left(y_1 - y_2\right)\right\}}{\left(x_1 - x_3\right)\left(y_1 - y_2\right) - \left(x_1 - x_2\right)\left(y_1 - y_3\right)} \tag{2.6}$$

$$\ell = \frac{f\left\{\tau_{13}\left(x_1 - x_2\right) - \tau_{12}\left(x_1 - x_3\right)\right\}}{\left(x_1 - x_3\right)\left(y_1 - y_2\right) - \left(x_1 - x_2\right)\left(y_1 - y_3\right)} \tag{2.7}$$

$$v_p = \frac{f}{\sqrt{k^2 + \ell^2}} \tag{2.8}$$

$$\alpha = 180° + \tan^{-1}|k/\ell| \quad \text{if} \quad k > 0, \quad k > 0,\, \ell > 0 \tag{2.9}$$

$$\alpha = 180° - \tan^{-1}|k/\ell| \quad \text{if} \quad k < 0, \quad k < 0,\, \ell > 0 \tag{2.10}$$

$$\alpha = 0° + \tan^{-1}|k/\ell| \quad \text{if} \quad k < 0, \quad k < 0,\, \ell < 0 \tag{2.11}$$

$$\alpha = 360° - \tan^{-1}|k/\ell| \quad \text{if} \quad k > 0, \quad k > 0,\, \ell < 0 \tag{2.12}$$

Note that since k and ℓ are linear functions of f (Eq. 2.6 and Eq. 2.7), then Eqs. 2.8-2.11 show that v_p and α are not functions of f. The angle α is defined as if measured from the north toward the direction of propagation. In order to have a consistent definition with the wind direction, α is later rotated to the standard meteorological convention.

Sampling windows are extracted from the three satellite stations over the same time periods as for the main station. An arbitrary example of a sampling window is shown in Fig. 2.2, illustrating a central event at the main station and its development through the network. To calculate the time lags between stations, the wind components were averaged to 10 s. A number of different averages were tried, and the 10-s average was found to perform best at removing small-scale variability while maintaining the main features of wind-direction shifts. The time lags between the stations of the network are determined using the maximum cross-correlation. In order to improve accuracy of the time-lag estimates, we use both horizontal wind components and the mean wind speed in

calculations of the cross-correlation. From the four stations, six pairs of maximum cross-correlation coefficients and the corresponding time lags are obtained for each variable. The value of 0.7 is defined as the lower limit for the maximum cross-correlation coefficient using trial and error. Cases with two or more maximum cross-correlation coefficients from the six pairs that are above this limit are considered for propagation estimation. To choose among the available variables the one that will be used to estimate the speed and direction of propagation for a particular case, the variable with the greatest maximum cross-correlation coefficient averaged over the six pairs of stations is chosen.

2.3 Submeso Statistics

Here we calculate different measures of submeso variability and compare them with other field experiments and previous publications.

2.3.1 Cross-Wind Velocity Variance

While the remainder of the study uses the entire nocturnal period, the stable conditions are quantified using the dimensionless stability parameter z/L, where z is the measurement height and L is the Obukhov length. For determining L, the turbulent fluctuations are calculated as deviations from the 5-min mean and the averaging time for fluxes is 4 h, which is consistent with the definition of the cross-wind velocity variance. This is done for the purpose of consistent comparison with the results of Vickers and Mahrt (2007). Following Vickers and Mahrt (2007), two classes of stable conditions are defined: the first with $0 < z/L < 0.1$ for weakly stable conditions, and the second with $0.1 < z/L < 2$. The mean and standard deviation of the cross-wind variance for different averaging lengths and two stability classes are shown in Table 2.1.

Vickers and Mahrt (2007) analyzed the cross-wind velocity variance for nine datasets in the USA and found that the variance was larger in complex terrain compared to flatter terrain and near homogeneous sites. Table 2.1 shows the cross-wind velocity variance for two of these datasets: FLOSSII, which lies in a complex terrain setting, and the Cooperative Atmosphere-Surface Exchange Study (CASES-99) (Poulos et al. 2002), which is over a relatively flat and homogeneous grass-covered terrain. Our homogeneous site has
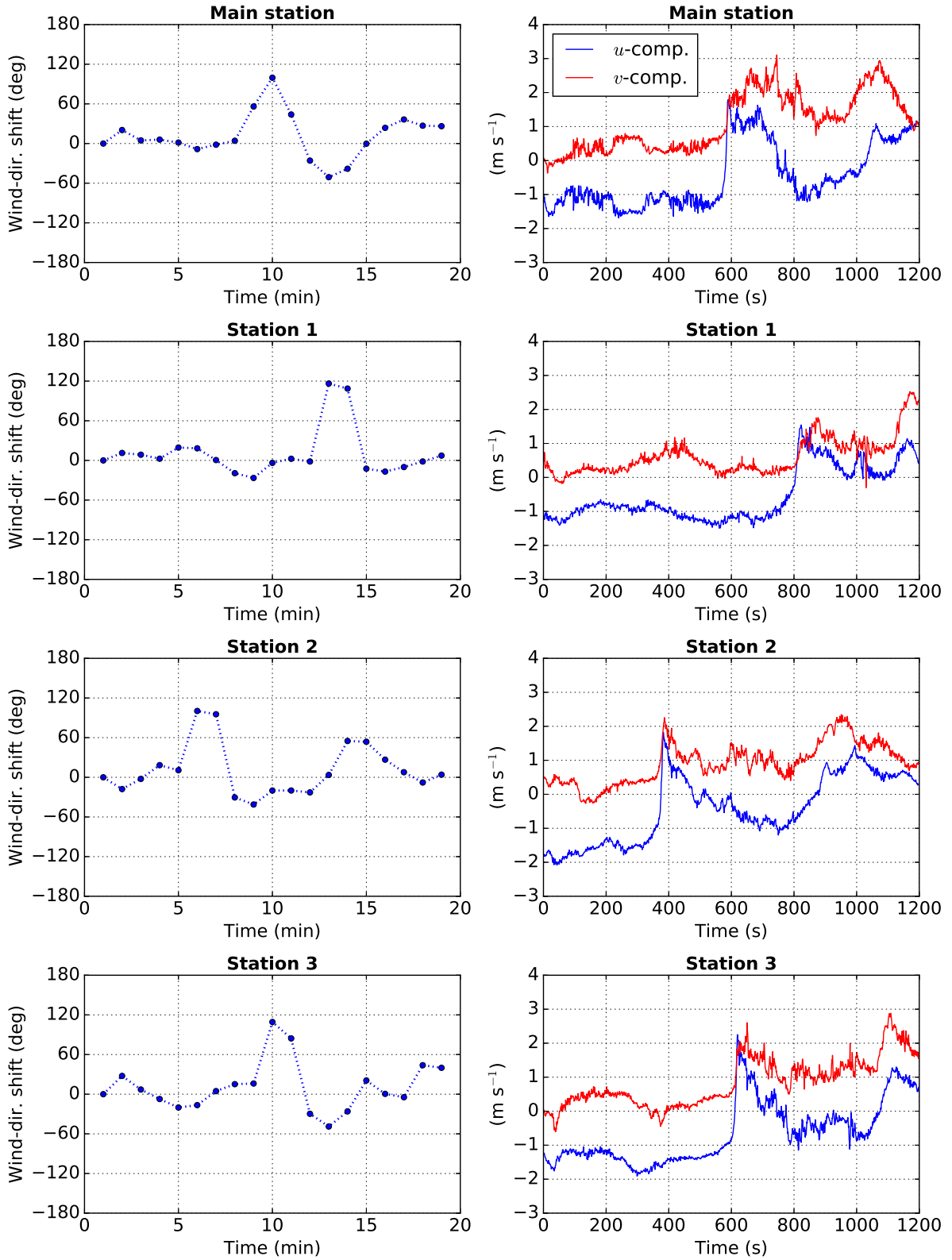
Figure 2.2: An example of a sampling window for all the stations of the network: the wind-direction shifts (left panels) and 1-s averages (for display purposes) of the horizontal velocity components (right panels).

Table 2.2: Site name of field experiments, surface conditions, height of the sensor above the ground, percentage of records with $RV_{meso} > 1$ and percentage of records with a wind-direction shift of 90° or larger.

Site	sfc.	h	$RV_{meso} > 1$	Shift $> 90°$
Victoria	Grass/crops	3	3	14
FLOSSII	Grass/snow	2	14	23
CASES-99	Grass	5	2	16

variances similar to CASES-99 and other such sites from Vickers and Mahrt (2007), which agrees with the hypothesis that the terrain complexity influences the submeso motions.

2.3.2 Mesovelocity Scale

The two additional datasets are used here as well to compare the overall statistics of RV_{meso} for stable conditions between different sites (Table 2.2). In the FLOSSII experiment, $RV_{meso} > 1$ occurs 14% of the time. On the other hand, for a flatter-terrain site, such as in CASES-99, this reduces to 2% of the time. Although the variability even between similar sites is generally large, $RV_{meso} > 1$ occurs 3% of the time for our site, which is comparable to a flatter site such as that at CASES-99.

2.4 Wind-direction Shifts

2.4.1 Frequency Distribution of Wind-direction Shifts

A total of 381 events were detected at the main station over the 89 nights, leading to 130 samples using the 20-min sampling window. There are usually two or more events in each sample, suggesting that isolated events are not common. We use only the central values of wind-direction-shifts within a sample, together with other available variables, to investigate the characteristics of 130 wind-direction-shift events.

The distribution of wind-direction shifts in Fig. 2.3a shows that there are 72 negative shifts (counter-clockwise rotation) and 58 positive shifts (clockwise rotation). The preference for counter-clockwise rotation is robust to the changes of the period of analysis, so there are more negative shifts during the longer 22-month period too, with the ratio of negative to positive shifts increasing with ΔWD. It could be hypothesized that
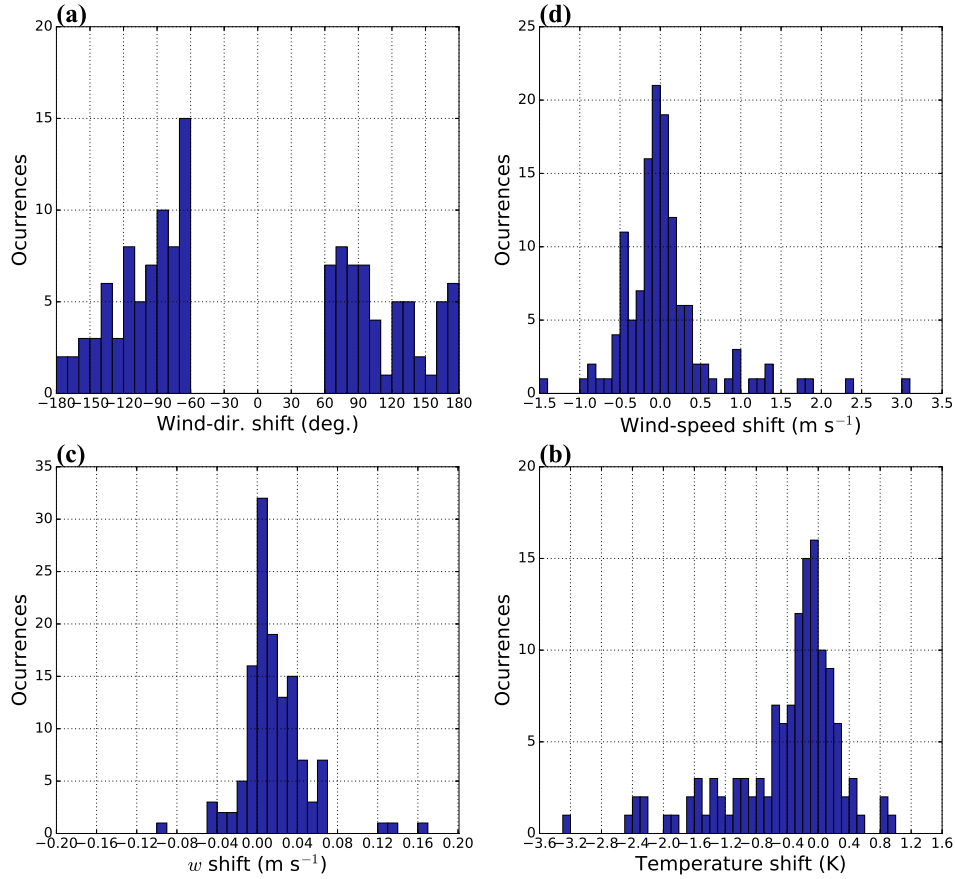
Figure 2.3: Distribution of changes of the (a) wind direction, (b) wind speed, (c) vertical velocity component (w) and (d) temperature for the central events detected at the main station.

the events resulting from downward mixing would have a tendency for counter-clockwise rotation in the Southern Hemisphere due to the possible Ekman turning in the ABL or due to the local acceleration resulting from vertical convergence of the momentum flux (Hande et al. 2012b; Sun et al. 2013), while other mechanisms would not show such a preference. The samples were first separated according to the direction of rotation and analyzed separately. However, no significant structural difference between clockwise and counter-clockwise wind-direction shifts was detected, so we continue the analysis on all the samples together and return to the question of direction of rotation later. The central events are characterized by wind speeds below 1.5 m s^{-1} in 95% of the cases. This is in agreement with Anfossi et al. (2005), who defined wind speeds < 1.5 m s^{-1} as weak flow, with significant mesoscale variability of the wind direction occurring when large-scale flow was weak.
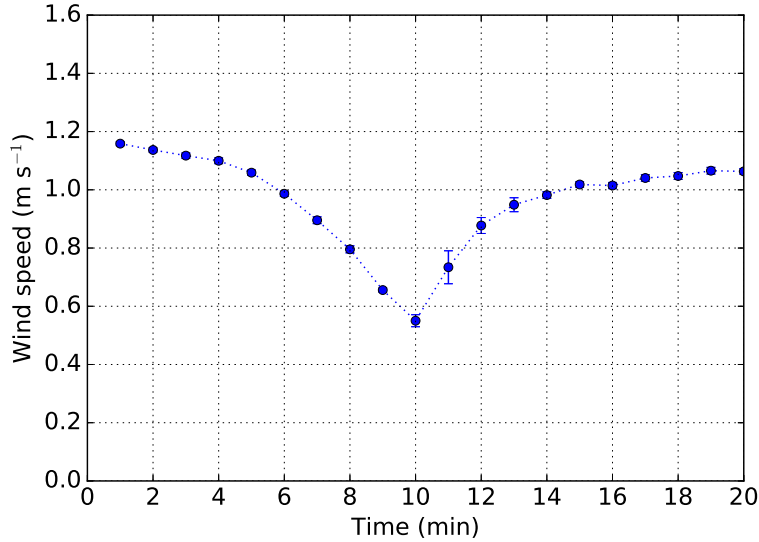
Figure 2.4: Composite structure of mean wind speed for the central events detected at the main station. Error bars show ± one standard error.

Changes in the wind speed during a central event are shown in Fig. 2.3b. Slightly more events (53%) are characterized with an increase of wind speed, and most of the changes are small, with values below 0.5 m s^{-1}. These changes, however, are defined by a centred difference over each 2-min interval. As such, they do not capture any transient fluctuations within this 2-min window including at the exact time of the event. To illustrate this, Fig. 2.4 shows the composite mean wind speed over all samples, indicating a considerable decrease of mean wind speed during a wind-direction shift. This decrease is evident for both scalar- and vector-averaged wind speed. The vertical velocity component shows a tendency to increase during an event (76%; Fig. 2.3c) and we will return to this below.

The frequency distribution of temperature changes (Fig. 2.3d) shows a tendency to decrease (74%), which includes a few especially large temperature changes. This is consistent with Mahrt (2010), where in stable conditions the strongest wind-direction shift tends to occur with a sharp decrease of temperature (a cold microfront).

2.4.2 Effects of Temperature

Relatively large oscillations of air temperature are quite common in the very stable regime (Mahrt 2014), and here we look at the effects of temperature increase and decrease on the vertical motion and turbulence during an event. The samples have been separated according to the sign of the temperature derivative during the central event and then

Table 2.3: Number of cases and mean speeds (m s^{-1}) for wind and propagation, separated by the effects of temperature.

	All cases		Propagation cases		
	n	Wind speed	n	Wind speed	Propagation speed
$dT/dt < 0$	96	1.0	51	1.1	3.8
$dT/dt > 0$	34	0.7	18	0.7	2.6

composited according to the temperature decrease or increase. Table 2.3 shows the number of cases for each group. The temperature decrease is considerably more frequent for these large and sudden wind-direction shifts. Additionally, the cases with decreasing temperature tend to be associated with somewhat larger mean wind speeds.

Both the composite structure of the vertical velocity component and its variance reveal a clear difference between increasing and decreasing temperature cases (Fig. 2.5). The most conspicuous characteristic is that rising motion is found when the temperature decreases (Fig. 2.5a), followed by a positive change in the vertical velocity variance corresponding to an increase in turbulence intensity (Fig. 2.5b). As the composite structure is based on 1-min averages, this does not include small overturning events at, or immediately behind, the temperature decrease. These results for the decreasing temperature are in agreement with Mahrt (2010), who observed that the maximum rising motion is above the cold microfront. In contrast, positive changes of temperature exhibit an increase of mixing during the sudden wind-direction shift and sinking motion closely following the shift. Again, these results are consistent with Mahrt (2010), who found that warm microfronts are associated with sinking motion in the warm air behind the microfront, suggesting that advection and downward mixing of air with higher momentum and higher temperatures could produce such warm microfronts. It is interesting to note that positive changes of temperature, which are associated with increased mixing after the microfront passage, have a tendency to develop clockwise wind-direction shifts, with 65% of the cases exhibiting this behaviour. This result is not consistent with the hypothesized effects of downward mixing assuming Ekman turning in the ABL. However, a more detailed analysis would require vertical profiles of the wind direction, which were not available for this field experiment. The opposite behaviour is found for negative temperature changes, with 63% of the cases having counter-clockwise shifts.
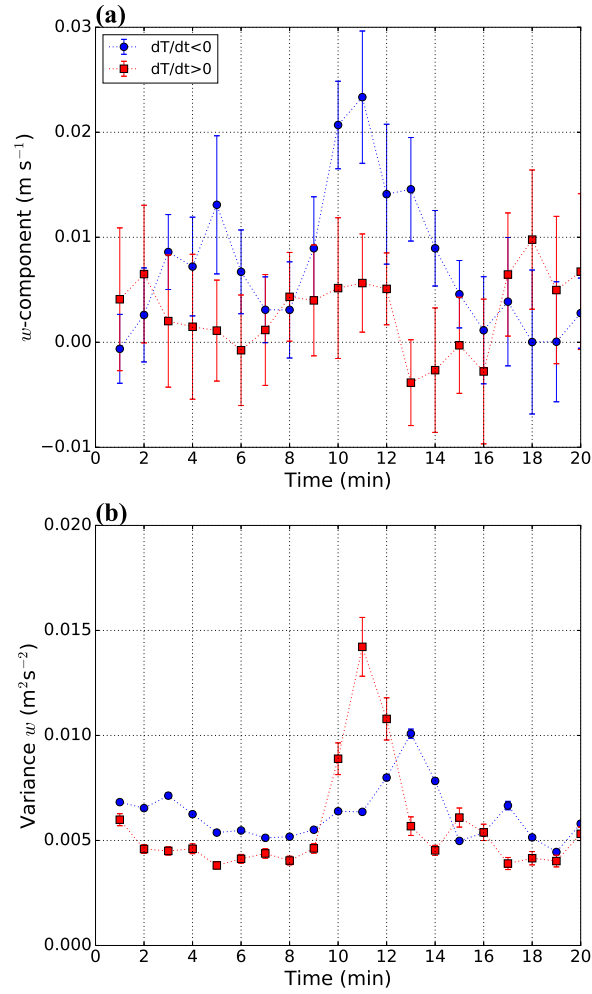
Figure 2.5: Composited structure separated by increasing and decreasing temperature of, (a) vertical velocity component, and (b) variance of the vertical velocity component for the central events detected at the main station. Error bars show $\pm$ one standard error.
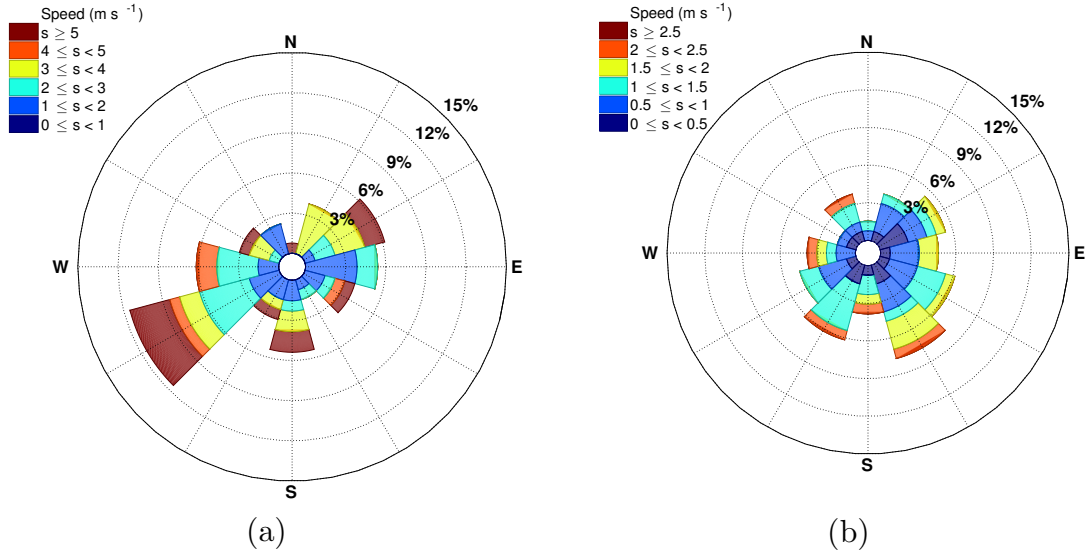
Figure 2.6: Roses of, (a) propagation of the central events, and (b) the corresponding mean wind speed at the main station for the 3-month period.

2.5 Propagation of Structures

2.5.1 Direction and Speed of Propagation

Of the original 130 samples, 84 remained after the minimum cross-correlation constraint was applied. The constraint was applied to any combination of three station towers, even though all four stations were available for this period. To make the selection of cases more robust, all four combinations of three station towers were tested. We required that at least two of the four combinations to be within $30°$ and 2 m s^{-1} of each other. We then used the average of these "consistent" combinations to obtain a single value for the speed and direction for a sample. This additional "consistency" constraint further reduced the number of useful samples to 69.

A "propagation rose" for these 69 samples (Fig. 2.6a) displays a strong south-westerly preference despite the mostly homogeneous, flat terrain. Overall, the average propagation speed for the 69 samples is 3.5 m s^{-1} with approximately 72% of these events having propagation speeds between 1 and 4 m s^{-1}. Few samples reach speeds greater than 10 m s^{-1}.

It is important to examine whether the propagation is related to the mean wind vector. The wind rose for the 69 samples (Fig. 2.6b) does not display any strong preference for
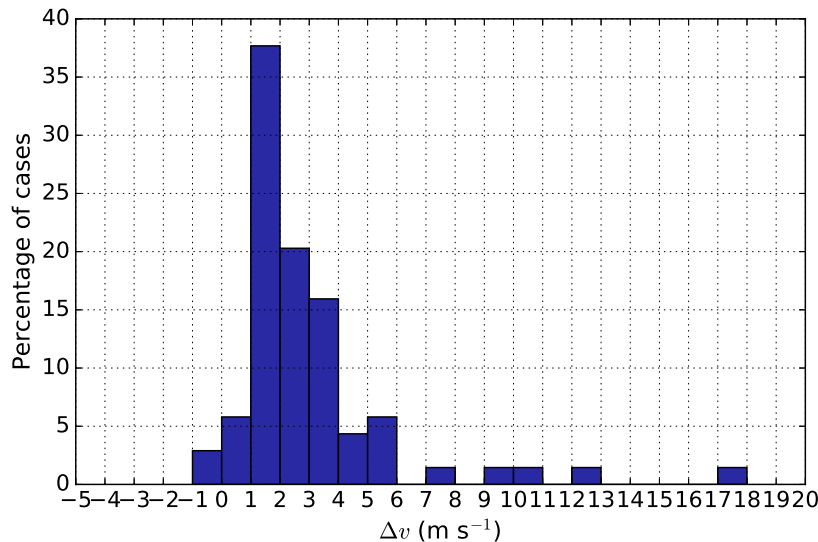
Figure 2.7: Frequency distribution of differences between the propagation speed and the corresponding mean wind speed (Δv) at the main station for the 3-month period.

wind direction and is not similar to the propagation rose. Rees and Mobbs (1988) found similar results for gravity waves at Halley Base, Antarctica. The distribution of the difference between propagation speed and wind speed (Fig. 2.7) displays a clear tendency for the propagation speed to be greater than the wind speed. The correlation coefficient between the propagation and wind speed is -0.005, and the correlation coefficient between the propagation and wind direction is -0.12, which does not support any relationship between the propagation and the mean wind.

The effects of temperature on the propagation speed are shown in Table 2.3. As in the previous analysis with all the samples, decreasing temperature exhibits a larger number of cases and somewhat larger mean wind speeds. Propagation speed follows this behaviour and the events propagate more rapidly when temperature decreases.

2.5.2 Complete Period of Measurements

Here we perform the same analysis as above, except for the entire period when the three satellite stations were operating (22 months). The main station is substituted by station 1 to detect wind-direction-shift events. A total of 1565 wind-direction-shift events and 861 sampling windows were found at station 1. Using the same threshold of 0.7 for the cross-correlation coefficient as before, 736 samples are obtained for the calculation of speed and direction of propagation. No additional "consistency' criteria can be applied.
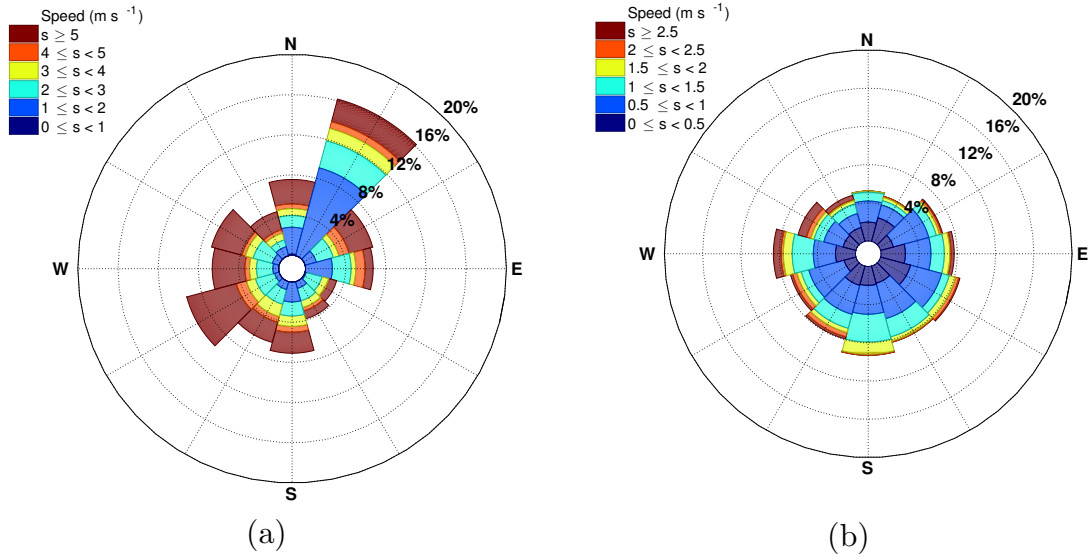
Figure 2.8: Roses for the complete observational period of, (a) propagation of the central events, and (b) the corresponding mean wind speed at station 1.

Figure 2.8 shows both the propagation and mean wind roses for the 736 samples. As before, there is no clear relationship between either the propagation and mean wind direction or the propagation and mean wind speed. The absolute values of correlation coefficient for speed and direction between propagation and mean wind vectors are less than 0.15. The propagation speeds are again most of the time greater than wind speed, with values of wind speed under 5 m s^{-1} and some values of propagation speed reaching 30 m s^{-1}. While there is still a clear preference for a south-westerly direction for the propagation direction, there is now a much stronger preference for a north-easterly origin. One could speculate that the predominance of north-easterly propagation directions is related to a 20-m hill located 15 km north-east of the network. Sun et al. (2015a) found that for the relatively flat CASES-99 site, the changes in wind and temperature were generated by internal gravity waves resulting from cold currents associated with small terrain irregularities.

The complete period of measurements allowed the analysis of the seasonal variability of wind-direction shifts. The seasonal cycle of the number of wind-direction shifts per night (Fig. 2.9a) peaks during the cold season (JJA) and has a minimum during the warm season (DJF). The variability of the number of events is larger between years than seasons (not shown). A stronger seasonal variability is present for the time between
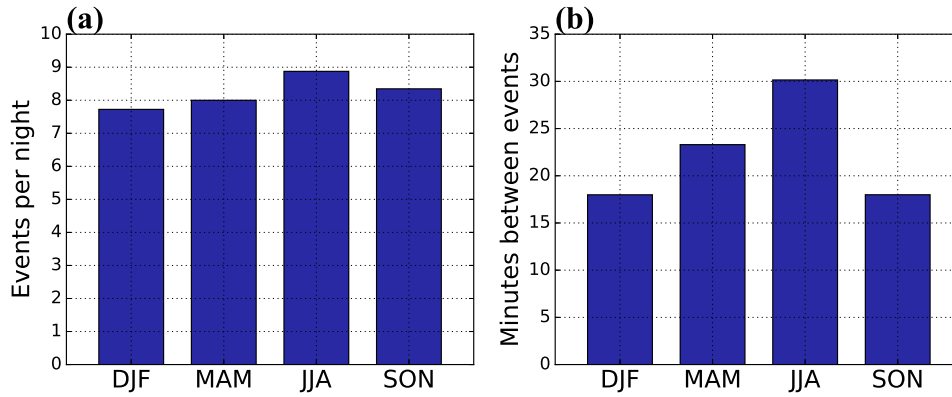
Figure 2.9: Seasonal variability of, (a) the average number of wind-direction shifts per night, and (b) the average time (minutes) between wind-direction shifts.

events, where the mean time between events increases from 18 min in the warm season to 30 min in the cold season (Fig. 2.9b).

The propagation direction of the samples exhibits a noticeable seasonal cycle (Fig. 2.10). During JJA and SON there is a strong tendency of wind-direction shifts to develop and propagate from the north-east, similar to the overall mean. During DJF the propagation is predominantly from the south-west, which is similar to the propagation during the 3-month period (Figure 7) of all four towers operating. MAM is as a transitional period between the warm and cold seasons. Figure 2.11 shows the corresponding mean wind roses for each season. Although the mean wind exhibits some seasonal changes, there is still no obvious relationship between it and the propagation vector.

2.6 Discussion and Conclusions

A horizontal network of high-resolution measurements in north-western Victoria, Australia is used to estimate statistics of submeso motions over an area with relatively homogeneous and flat terrain. The submeso motions at this site exhibit behaviour typical for this type of terrain, such as the lower relative mesovelocity scale and smaller cross-wind variances than for complex terrain. These results corroborate the hypothesis that local surface features, such as terrain complexity and surface heterogeneity, influence submeso processes.

The wind-direction variability in stable conditions was analyzed by extracting individual events with large and sudden wind-direction shifts. The large sudden wind-direction
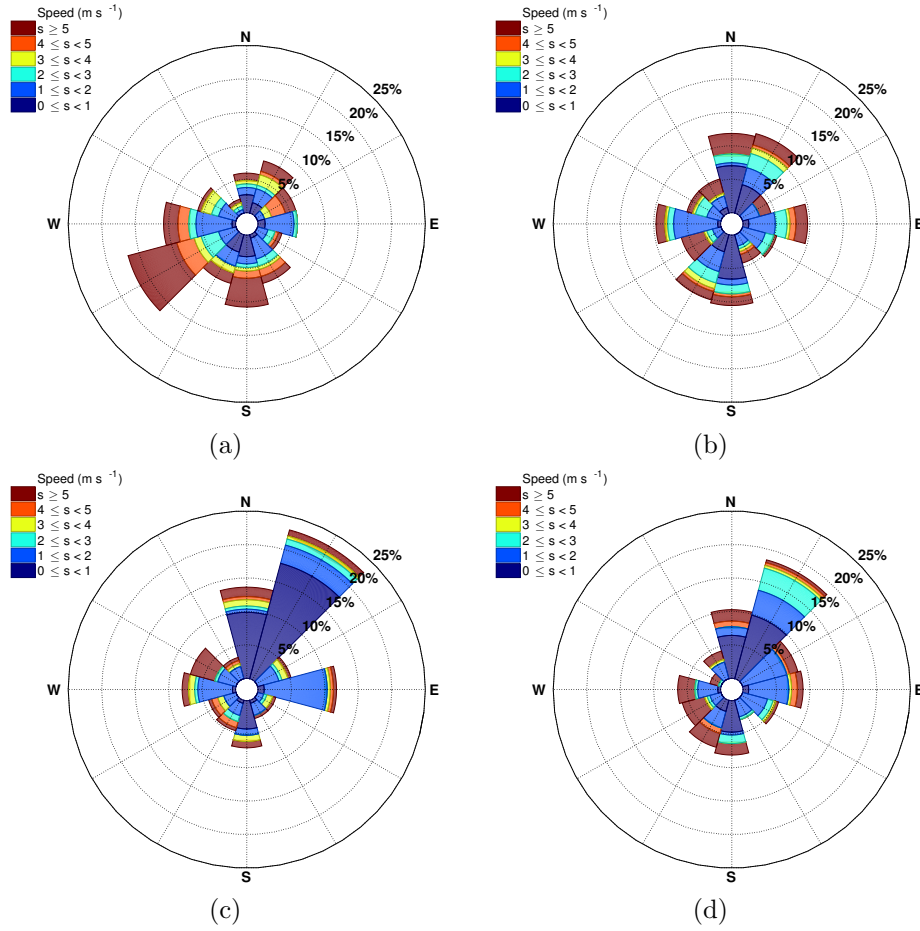
Figure 2.10: Seasonal roses of propagation of the central events at station 1 for the complete observational period. (a) DJF, (b) MAM, (c) JJA and (d) SON.
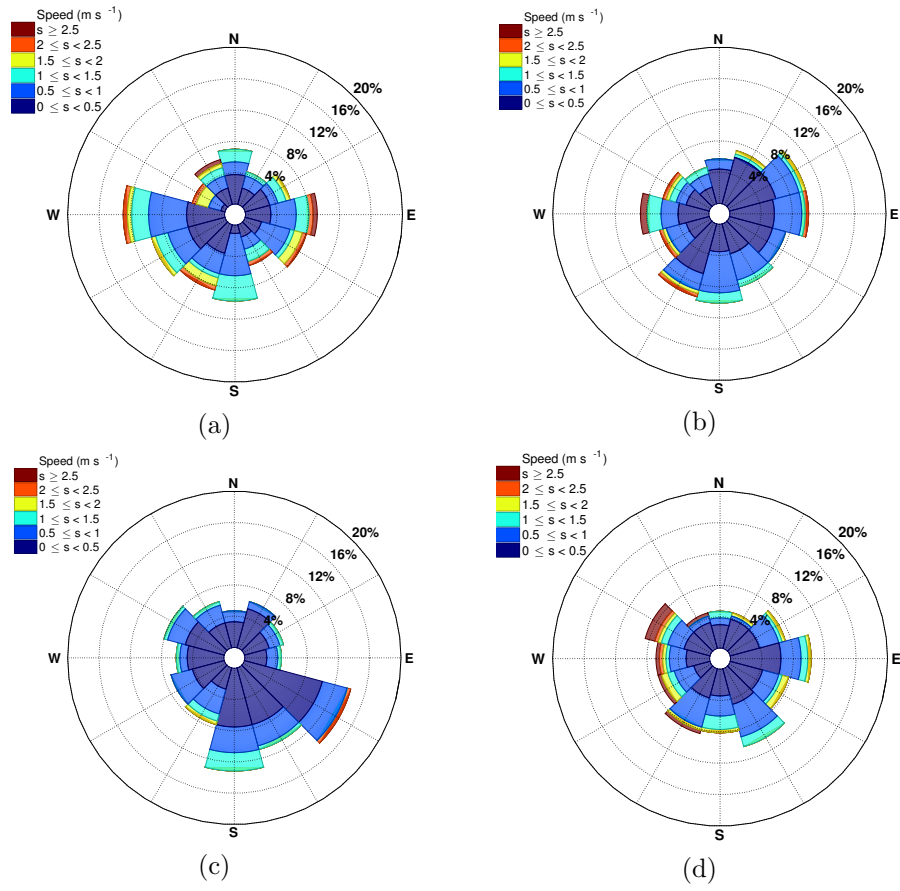
Figure 2.11: As Fig. 10, except showing the roses of mean wind speed corresponding to the central events.

shifts have a tendency to develop with a decrease in air temperature (74% of time). These events are associated with rising motions when the temperature decreases, suggesting that an external source of energy is required to maintain these thermal circulations. Characteristics of large changes in wind direction are consistent with previous studies (e.g., Mahrt 2007, 2008).

The horizontal propagation of the wind-direction shifts was analyzed using the cross-correlation function method. The propagation directions show a preference for directions from the south-west during the 3-month period. However, when the entire dataset of 22 months is considered, the preference shifts to a north-easterly direction, although with considerable seasonal variability. A potential source of events propagating from the north-east could be related to the 20-m hill located about 15 km to the north-east of the network, while the south-westerly propagation might be related to the 30-m hill located about 30 km to the south-west. If true, this would imply that disturbances generated by small obstacles in a stable boundary layer propagate several tens of km and produce large and sudden wind-direction shifts, together with the associated effects analyzed herein. Such behaviour would preclude strictly local parametrization of submeso motions in numerical models. Further analysis is needed to confirm the generality of such mechanisms.

Propagation speeds tend to be greater than the mean wind speed for all the cases analyzed. There is no relationship between the propagation vector and the mean wind vector, indicating that the events are not flow perturbations advected by the local flow. Hence the Taylor hypothesis is not applicable, and no inference can be made about the spatial structure of submeso motions from time series. This indicates that developing a suitable parametrization in numerical models might require different techniques and observations than are typically available from point measurements. Furthermore, if the observed relationship between the terrain complexity and submeso variability can be quantified, parametrizations could be developed that are based on the characteristics of the model subgrid-scale terrain.

Chapter 3

Characteristics of the Marine Atmospheric Boundary Layer over the Southern Ocean in Response to the Synoptic Forcing[*]

3.1 Introduction

Biases in the energy budget over the Southern Ocean (SO) persist in both reanalysis data sets and coupled global climate models. Trenberth and Fasullo (2010) identified that a multitude of general circulation models (GCMs) present a systematic negative bias in cloud amount over the SO, which contributes directly to an overestimation of the incoming shortwave radiation that is further linked to persistent biases in the SO mixed-layer temperatures (Bodas-Salcedo et al. 2014; Sallée et al. 2013). Further, large uncertainties exist in the estimated amount of precipitation over the SO (Behrangi et al. 2014), which also has the potential to contribute to the regional biases. The ubiquitous boundary layer clouds over the SO (Huang et al. 2012a; Mace et al. 2009; Muhlbauer et al. 2014) have been linked to both the incoming solar radiation bias (Bodas-Salcedo et al. 2016) and, more recently, to frequent drizzle/light precipitation (Ahn et al. 2017; Huang et al. 2017). In order to better understand potential biases in the boundary layer clouds, it is necessary to understand if the boundary layer structure is properly represented in the widely used climate data sets.

---

[*]This chapter is word-for-word the published paper: Lang, F., Y. Huang, S. T. Siems and M. J. Manton (2018). Characteristics of the marine atmospheric boundary layer over the Southern Ocean in response to the synoptic forcing. *J. Geophys. Res.: Atmospheres.* 123(15), 7799-7820. doi: 10.1029/2018JD028700

The storm track over the SO is characterized by a high density of extratropical cyclones and fronts (e.g., Hoskins and Hodges 2005; Simmonds and Keay 2000), where low-altitude clouds are commonly present in prefrontal and postfrontal environments (Haynes et al. 2011). Bodas-Salcedo et al. (2012) and Williams et al. (2013) suggest that the climate models had difficulties in producing low-level clouds in the cold sector of common extratropical cyclones over the SO, and this may be a major contributor to the large shortwave radiative bias in this region. The cold sector of the cyclones is dominated by subsidence and low-level, often broken, clouds (e.g., Haynes et al. 2011; Naud et al. 2014, 2015; Norris 1998a,b).

The remote nature of the SO and its harsh environment has severely limited the ability to make either routine or intensive field observations. Many of the advances in our knowledge made in the past decade have relied heavily on satellite observations. This knowledge has underpinned many studies on evaluating reanalysis products and numerical simulations. For example, Naud et al. (2014) used A-train satellite observations to find that both the Modern-Era Retrospective Analysis for Research and Applications (MERRA) and European Centre for Medium-Range Weather Forecasts (ECMWF) ERA-Interim reanalysis (Dee et al. 2011) products underrepresent the cloud cover in the cold sector of cyclones over the SO. Huang et al. (2014) employed A-train observations to evaluate Weather Research and Forecasting Model (WRF) simulations of clouds, finding that the simulations have great difficulties in reproducing the amount of marine boundary layer clouds commonly found in the hours after a frontal passage. They speculate that these difficulties are due to errors in representing the marine atmospheric boundary layer (MABL) processes, possibly as a result of either strong entrainment or weak surface fluxes. These findings suggest that the poor simulations of MABL clouds may partially be attributable to the poor representation of the physical processes that govern the MABL dynamics.

Unfortunately, space-borne remote-sensing technologies have known challenges in accurately retrieving shallow boundary layer clouds and their properties (Chan and Comiso 2011; Huang et al. 2012a). Infrared observations, for example, are often interfered by the emissivity of the underlying sea surface, thus having difficulties in accurately retrieving

cloud-top temperature/height for MABL clouds (Holz et al. 2008). CloudSat, with the cloud profiling radar aboard, cannot reliably measure reflectivities in the lowest kilometer due to ground clutter (Marchand et al. 2008). The space-borne lidar on Cloud-Aerosol Lidar and Infrared Pathfinder Satellite Observation, despite its high resolutions, suffers from heavy signal extinction through liquid cloud tops, as well as contaminations by sea spray aerosols in MABL (Kawai et al. 2015). These challenges are exacerbated over the SO, where low-level clouds are commonly observed (Haynes et al. 2011) with altitude as shallow as 500 m (Hande et al. 2012b; Huang et al. 2012b) and highly stratified (Jensen et al. 2000; Russell et al. 1998). Both the lack of in-situ observations and the ambiguity in satellite observations have prevented confidence in the representation of MABL thermodynamic structure over the SO (Naud et al. 2014).

The ongoing historical field observations at Macquarie Island (MAC, 54.62°S, 158.85°E) are one of a few long-term records that allow for a study of both the thermodynamics of the MABL (e.g., Hande et al. 2012b) and surface precipitation (e.g., Adams 2009; Wang et al. 2015) over the measurement-sparse SO. Hande et al. (2012b) employed the upper-air soundings at Macquarie Island to construct a climatology of the thermodynamic structure of the MABL. They identified systematic biases in ECMWF operational analysis, noting discrepancies in the inversion height, boundary layer wind shear (which potentially affects entrainment and surface fluxes) and boundary layer decoupling. Specifically, Hande et al. (2012b) found that the average height of the primary inversion was 1,302 m from field observations but only 1,144 m for the ECMWF operational analysis. This is particularly interesting as Williams et al. (2013) noted that climate model simulations of the MABL inversion over the SO were commonly too shallow in comparison with the ECMWF product. They attributed this error to the coarse vertical resolution of the simulations.

The precipitation records at Macquarie Island have also been of interest: Adams (2009) highlighted a 35% increase in the annual precipitation at Macquarie Island over the period from 1971 to 2008. Wang et al. (2015) analyzed the climatology of the precipitation over Macquarie Island. They found that a majority of the surface precipitation is relatively weak (<0.5 mm hr^{-1}) and arrives predominantly from the west. Higher precipitation rates are found to be more commonly associated with cold fronts, which contribute to

more than 40% of the precipitation above 1 mm hr^{-1}. CloudSat precipitation products and the ERA-Interim reanalysis precipitation were found to underestimate the frequency of light precipitation in comparison to the surface observations. This is potentially a consequence of light precipitation from shallow clouds not being adequately represented in either CloudSat or ERA-Interim. They estimated that the average annual Macquarie Island precipitation (1,023 mm) was approximately 6.8% greater than that from ERA-Interim (953 mm) from 1979 to 2011.

Neither Hande et al. (2012b) nor Wang et al. (2015) coupled the thermodynamic soundings with the surface precipitation. Further, Hande et al. (2012b) did not explore the relationship between the synoptic meteorology and the thermodynamic structure. Specifically, no investigation was made on the potential bias in the MABL in the post-frontal environment that has been linked to the cloud and radiation bias. In this study, a 16-year record (1995-2010) of high-resolution upper-air soundings at Macquarie Island and the ECMWF ERA-Interim operational reanalysis data set are employed to examine the thermodynamic structure of the MABL over the SO and its response to the synoptic meteorology. Our aim is to employ the field observations to understand the role of fronts and midlatitude cyclones in shaping the MABL characteristics and to evaluate its representation in the ERA-Interim reanalysis. Further, this analysis is extended to the surface precipitation. Our examination is primarily focused on the post-cold-frontal environment given that the largest model bias has been linked to this sector.

3.2 Data and Methods

3.2.1 Macquarie Island Observations and ERA-Interim Data set

Macquarie Island is uniquely situated in the midst of the SO (54.62°S, 158.85°E), approximately half way between Australia and Antarctica. A station has been maintained by the Australian Antarctic Division since 1948, located at the northern end of the island (Fig. 3.1a). Standard surface observations are recorded since 1995 along with twice daily upper-air soundings and hourly precipitation records. The launch site of soundings is at an elevation of 8 m above sea level and has direct exposure to the prevailing west-

(a)

(b)

(c)
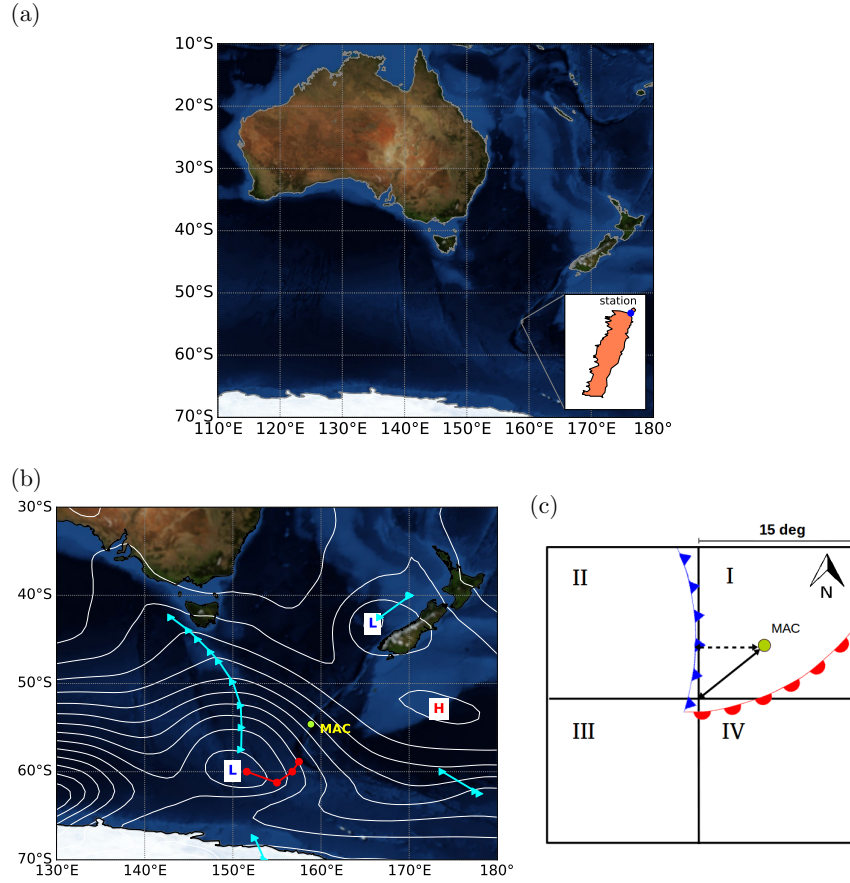
Figure 3.1: (a) Map showing the location of Macquarie Island over the Southern Ocean. The inset shows Macquarie Island together with the approximate location of the station. (b) Mean sea level pressure analysis over Macquarie Island for 5 September 2006 at 00 Z. Front locations are indicated by lines with triangle and circle symbols indicating cold and warm front, respectively. (c) Cyclone-centered scheme relative to the island; black line indicates distance between MAC and low pressure center, and dashed line indicates distance between MAC and closest point from the cold front.

erly winds (Wang et al. 2015). Wang et al. (2016) used high-resolution simulations to demonstrate that the orographic influence on the station measurements is not paramount under the most common synoptic conditions. As such, the station record is appropriate for long-term climate studies in this area.

The upper-air data used in this analysis are the 10-s vertical resolution atmospheric soundings obtained from the Australian Bureau of Meteorology for the period from 1995 through to 2010. During this period, the upper-air soundings were launched twice per day for 96% of all days, comprising 11,327 soundings in total. These upper-air soundings data are used to determinate the height of the MABL following Hande et al. (2012b). For comparison with the ERA-Interim data set that is constructed at a much lower resolution

(37 pressure levels), the high resolution MAC soundings are initially smoothed using a five-point running average to remove small scale variability. Hande et al. (2012b) tested a number of different smoothing options on the MAC soundings, finding that the five-point running average performs the best while maintaining the main features of the thermo-dynamic profiles. The smoothed profiles are then interpolated on to standard pressure levels for comparison with ERA-Interim. Via sensitivity tests (not shown), the five-point smoothing was found to have a minor impact relative to the interpolation onto the 37 pressure levels. Given that the MAC surface pressure may occasionally be under 1,000-hPa level, the 1,000-hPa standard pressure level within ERA-Interim is used only where appropriate.

The method used to define the MABL height relies on the thermodynamic properties of the vertical profile. Following Hande et al. (2012b), the primary MABL inversion is defined as the maximum gradient in the virtual potential temperature profile, $d\theta_v/dz$, between 100 and 5,000 m with a minimum gradient threshold of 0.01 K m^{-1} required to define an inversion as "significant". This same definition is employed on the matching ERA-Interim reanalysis profiles. Note that no smoothing or interpolation is required for the ERA-Interim profiles.

A number of methodologies exist in the literature for determination of the atmospheric boundary layer (ABL) height, most of which are based on vertical gradients of thermodynamic variables. von Engeln and Teixeira (2013) present a comparison of different methods using the ECMWF reanalysis data set finding that, depending on the topic being studied, methods based on the vertical gradients of relative humidity, potential temperature and virtual temperature appear to be most robust. In this study, we have chosen to use the gradient of θ_v because it provides a reliable way of determining the planetary boundary layer (PBL) inversion, especially for marine cloudy boundary layer — a major characteristics of the SO — and has previously been used in Hande et al. (2012b). Another commonly used method employs the bulk Richardson number (e.g., Seibert et al. 2000; Seidel et al. 2012). While this method has been shown to have many advantages (e.g. less dependent on small differences in profile conditions), it is not considered to be most suitable for our interests, due to the following: (i) The calculation of the Richardson

number is less straightforward than obtaining the gradients of thermodynamic variables, and (ii) the Richardson number is a measure of local turbulence and thus poorly characterizes turbulent properties of convective, cloudy marine boundary layers. Specifically, von Engeln and Teixeira (2013) found that the Richardson number based method has a tendency to provide an estimated planetary boundary layer height that is closer to the cloud-base height in marine cloudy boundary layers.

The hourly MAC precipitation record is available from 1998 and its minimum detected precipitation is 0.2 mm for the hourly records. For ERA-Interim, the precipitation product is available at a 3-hr temporal resolution and $0.75° \times 0.75°$ spatial resolution. Note that the ERA-Interim precipitation represents a mean precipitation amount over a grid box while the MAC precipitation is a point measurement. Using typical surface wind speeds of 12–16 m s^{-1}, a 3-hr window of the MAC surface precipitation spans $\sim$140 km, which is on the same order of magnitude as ERA-Interim $0.75°$ (Wang et al. 2015).

3.2.2 Cyclones

SO extratropical cyclones were identified using the National Aeronautics and Space Administration Modeling, Analysis, and Prediction (MAP) Climatology of Midlatitude Storminess (MCMS; Bauer and Genio 2006; Bauer et al. 2016) database. The algorithm looks for sea level pressure local minima and tracks them over time. The MCMS software is intended for use on different gridded see level pressure data sources such as climate and reanalysis products. In this study, we use the ERA-Interim reanalysis. A detailed description of the MCMS algorithm is discussed in Bauer et al. (2016). Following this work, we use the term "cyclone" to refer to a specific storm event, rather than a complete storm life cycle. An example of the mean sea level pressure analysis over Macquarie Island and the cyclone-centered scheme are illustrated in Figures 3.1b and 3.1c. Each MAC sounding (and matching ERA-Interim profile) is paired with the closest MCMS cyclone core, and the location of MAC station is identified relative to the core (Fig. 3.1c), if the core is within $15°$ of the island. Following Naud et al. (2014) and Bodas-Salcedo et al. (2014), the cold-air side of the cyclone is defined roughly as the northwest and southwest quadrants (i.e., quadrants II and III, western side of the cyclones) and the warm sector as the

northeast quadrant (i.e., quadrant I, precold frontal area).

At the time of this study, the MCMS archive for ERA-Interim data set is available from 2006 to 2010. During this period, there were 3,514 soundings available at Macquarie Island, with 2,208 (63%) of these soundings located within 15° of a low-pressure center (Table 3.1). From these 2,208 soundings, a total of 1,941 (88%) present an inversion stronger than the defined threshold; the majority of the remaining 12% are located in the immediate vicinity of a cyclone core or cold front where a significant inversion is not detectable. The detection of significant inversion differs for ERA-Interim data, where 2,289 profiles associated with cyclone-centers are available. From the 2,208 sounding that match MAC, an inversion is detected in only 1,157 (52%) cases (Table 3.1). This means that 48% of profiles for ERA-Interim are classified as no significant inversion cases, indicating that the frequency of the significant inversion is underestimated in ERA-Interim at the specified threshold. As mentioned in section 3.1, a similar discrepancy is reported in Hande et al. (2012b) for the ECMWF operational analysis with 91 model levels, which provides much higher vertical resolution than ERA-Interim. The frequency of no significant inversion occurrence for MAC soundings reported in Hande et al. (2012b) is 15.6%, similar to our results, although they considered all soundings, not just those within 15° of a MCMS cyclone core. Using a Student's t test to compare MABL height means between the MAC and ERA-Interim data sets, differences were found to be statistically significant at the 95% confidence level.

As an initial step to examine the influence of different synoptic regimes on the MABL characteristics over Macquarie Island, a cluster analysis was performed on the MAC data set for the period between 2006 and 2010. The purpose of this analysis is to attempt to determine whether the observations at MAC can alone be related to the results of the cyclone analysis. A cluster analysis using only the MAC observations was chosen over other methods that depend on reanalysis products (e.g., self-organizing maps or empirical orthogonal functions), as such products have relatively coarse resolution over the remote SO and may miss mesoscale circulations (e.g., Irving et al. 2010). The cluster analysis algorithm used is the K-means cluster analysis algorithm (Anderberg 1973), which has been widely used in a variety of meteorological applications (e.g., Hande et al. 2012a;

Table 3.1: Number of soundings available: Soundings associated with cyclones or cold fronts, number of cases with an inversion, and number of no significant inversion cases in MAC and ERA-Interim soundings.

Analysis		Number of soundings			
		Total available	Total associated	Inversion	No significant inversion
Cyclones analysis (MCMS dataset, within 15°, 2006-2010)	MAC	3,514	2,208	1,941 (88%)	267 (12%)
	ERA-Interim			1,157 (52%)	1,051 (48%)
Cold fronts analysis (Berry et al. (2011) dataset, within 10°, 1995-2010)	MAC	11,327	2,806	2,469 (88%)	337 (12%)
	ERA-Interim			791 (28%)	2,015 (72%)

Jakob and Tselioudis 2003; Pope et al. 2009; Sarmadi et al. 2017) including to identify cloud regimes over the SO (e.g., Haynes et al. 2011; Mason et al. 2015).

The K-means clustering algorithm was run on low-level thermodynamic variables, specifically the temperature, relative humidity, zonal wind (u), and meridional wind (v) at 700, 850, 925 hPa and surface pressure, temperature and relative humidity (a total of 15 variables at four levels). Following the algorithm, these 15 variables have been normalized to zero mean and unity standard deviation before applying the cluster analysis. This procedure is commonly used in grouping soundings through cluster technique (e.g., Dai et al. 2014; Wilson et al. 2013). By choosing these variables, our interest is focused on the lower troposphere, where the MABL and the majority of the SO clouds reside (Huang et al. 2015, 2012a). The algorithm was run for 3 through 10 clusters. The most appropriate number of clusters was found to be 5, as this number makes it possible to readily differentiate known synoptic conditions, which could not otherwise be appreciated with a smaller number of groups. A larger number of clusters (≥ 6) generate at least one small cluster (less than five soundings), which is not considered to provide a robust representation.

3.2.3 Cold Fronts

The front data set used in this analysis was produced by Berry et al. (2011) with the ECMWF ERA-Interim reanalysis data, using the method originally proposed in Hewson (1998). This algorithm identifies fronts by the horizontal gradient in the wet-bulb potential temperature at 850 hPa and computes front speed ranges to differentiate between types of front (cold, warm and quasi-stationary fronts). Berry et al. (2011) found highest front frequency in the midlatitude storm tracks over the SO, North Atlantic, and North Pacific Oceans.

Similar to the cyclone-centered analysis method, we characterize the MABL structure in relation to the position of the Berry et al. (2011) cold fronts, in order to complement the understanding of the influence of synoptic characteristics. This common approach has been used in a number of studies to investigate the cloud cover deficiencies behind the cold fronts in model simulations and reanalysis data sets (e.g., Naud et al. 2016, 2015).

In this analysis each MAC sounding and matching ERA-Interim profile are paired with the closest Berry et al. (2011) cold front within 10°, and the relative distance to the island is estimated by calculating the minimum distance from the cold front (Fig. 3.1c). Soundings and precipitation records are averaged by distance into 1° bins, both prefrontal and postfrontal, to produce a composite cross-section across a cold front. Positive values of distance are pre-frontal (i.e., in the warm sector) and negative for post-frontal (i.e., cold sector) environments. Note that the analysis range was reduced from 15° to 10° for this section, as it is common to observe fronts far to the west of Macquarie Island that never actually reach the island (Berry et al. 2011). Soundings in this additional range arguably do not reflect the immediate frontal dynamics.

Berry et al. (2011) cold fronts were reviewed to check its agreement with synoptic features over the SO. A common deficiency was breaks in the continuity of the frontal lines, which may affect the accuracy of the number of fronts and their relative distance to Macquarie Island. A simple criterion was used to discard these cases: sets of points with less than two elements or cases with two or more points separated by distances greater than 5° (to avoid long breaks of continuity between the frontal points). It was found that ~11% of the cold fronts were discarded by this criteria, but further analysis (not shown) found that this additional filtering had little impact on the results.

During the period from 1995 to 2010 a total of 2,806 upper-air soundings are within 10° distance of a Berry et al. (2011) cold front. From these available soundings, 2,496 MAC soundings (88%) present a significant inversion. As for the cyclone case, detection of the significant inversion differs strongly for the matched ERA-Interim profiles, where only 791 (28%) cases present a significant inversion (Table 3.1).

Within the context of frontal passage, two additional metrics — lower troposphere stability (LTS; Klein and Hartmann 1993) and estimated inversion strength (EIS; Wood and Bretherton 2006) — are also examined. Previous studies have reported good correlations between low-level cloud amounts and LTS and EIS in various regions across the world (e.g., Muhlbauer et al. 2014; Naud et al. 2016). The EIS is defined as follows:

$$EIS = LTS - \Gamma_m^{850}\left(Z_{700} - LCL\right), \tag{3.1}$$

where the LTS is the lower-tropospheric stability defined in Klein and Hartmann (1993), that is the difference in potential temperature between 700 hPa and the surface ($LTS = \theta_{700} - \theta_{surf}$). The variable Γ_m^{850} is the moist-adiabatic potential temperature gradient at 850 hPa; Z_{700} is the altitude of the 700-hPa level, and LCL is the lifting condensation level, which is computed following Bolton (1980). For Γ_m^{850}, we use the equation given in Wood and Bretherton (2006), which depends on surface and 700-hPa air temperatures and the saturation specific humidity at 850 hPa, which is approximated with a formula proposed by Bolton (1980).

EIS represents the MABL inversion strength, which is a measure of the difference in potential temperature that caps the MABL. High EIS is associated with strong and low-lying inversions, which are more effective at trapping moisture within the MABL, permitting greater cloud cover (Wood and Bretherton 2006).

3.3 Analysis in Relation to Cyclones

In this section, we investigated the passage of MCMS cyclones to understand their influence on the MABL thermodynamic structure. The cyclone analysis includes 1,941 soundings from MAC and the matching 1,157 from ERA-Interim from 2006 to 2010 with a significant inversion within 15° of a MCMS cyclone core (Table 3.1). These soundings are used to create cyclone-centered composites for both MAC and ERA-Interim data sets to appreciate the influence of cyclones on MABL.

3.3.1 MABL and Precipitation Characteristics in SO Cyclones

3.3.1.1 MABL Characteristics

The analysis is sorted by quadrant, season and distance from the low center, respectively. The height of the MABL inversion is examined as a function of the quadrant, season and distance according to cyclone-centered composites (Fig. 3.2). In general, the variability of MAC inversion height is greater than that of ERA-Interim, this difference in the variability cannot simply be explained by the difference in the sample size, as will be discussed later. The MABL height is greatest in the northwest quadrant (Fig. 3.2a) for both MAC and

ERA-Interim, reaching a maximum median of 1,980 and 1,869 m, respectively. In general, the MABL height is lower when the island is to the south of a MCMS cyclone. For both MAC and ERA-Interim, soundings are more commonly found to the north of the cyclone center (top box percentages in Fig 3.2a), which suggests that cyclones more commonly pass to the south of Macquarie Island. The northeast quadrant with 689 soundings for MAC (35.5%), 389 for ERA-Interim (33.6%), and the northwest quadrant with 631 for MAC (32.5%), 351 for ERA-Interim (30.3%). We note that the SO polar front passes to the south of Macquarie Island (Dong et al. 2006). For the two north quadrants, the differences in the distributions between MAC and ERA-interim are statistically significant; for the two south quadrants, the differences are not statistically significant.

Figure 3.2b shows the seasonal variability of MABL height; MAC exhibits a noticeable seasonal cycle, with larger values of MABL height present during the austral spring (September–November), and the lowest values during the austral winter (June–August). ERA-Interim also exhibits a peak during spring, but a seasonal cycle is much less discernible. An important feature of the seasonal cycle is the presence of a shallower MABL during winter, consistent with Huang et al. (2015), where the MABL height is inferred from the cloud structure derived from the A-Train satellite observations. For both March–May and September–November seasons, statistically significant differences are found between MAC and ERA-Interim.

The statistics as a function of distance from the low centers are shown in Fig. 3.2c. Soundings have been grouped by distance from the cyclone center in 5° bins. These results suggest that fewer soundings have inversion detected between 0 and 5° from the low centers. This might be expected due to the low-level convergence of cyclones (i.e., regions of predominantly ascending air). For the cases where an inversion is detected in this bin, the lowest MABL heights are actually found, on average. This is true for both the observations and ERA-Interim, although the median MABL height for MAC is almost twice as high as for ERA-Interim. However, given that the frequencies of the profiles with an inversion within 5° of the low centers are quite low (8.2% for MAC and 5.8% for ERA-Interim), the implication of this result may be limited. In contrast, most of the profiles with a significant inversion are located at distances greater than 10–15°, 1,132
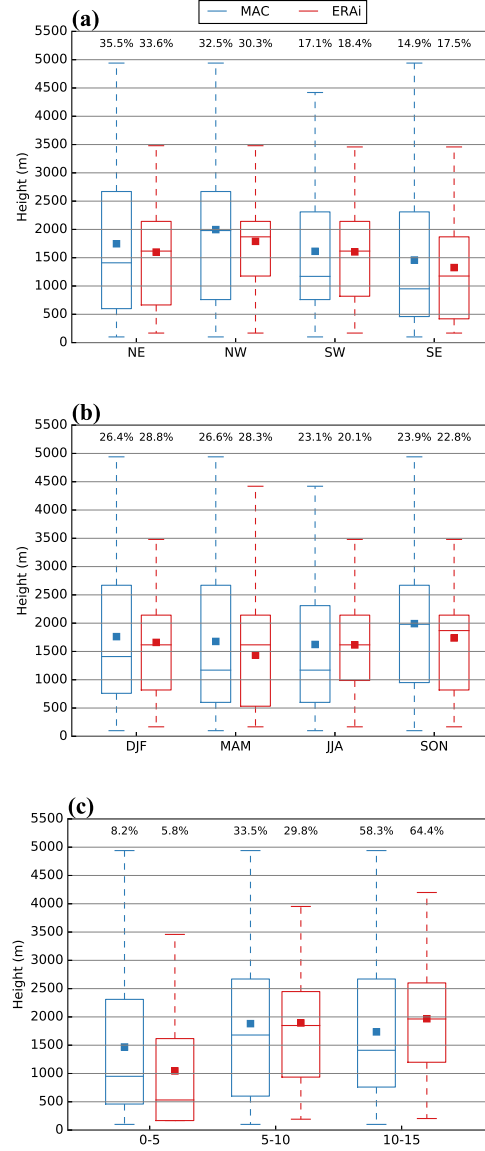
Figure 3.2: Box-and-whisker plots of the marine atmospheric boundary layer height statistics for cyclone-centered composites for MAC and ERA-Interim profiles (a) by quadrants, (b) by season and (c) by distance. The median values are shown as horizontal lines and the mean values as squares. Boxes indicate the interquartile range (25th to 75th percentiles) and the whiskers extend to $\pm 2\sigma$ of the standard normal distribution. Percentages on the top indicate the percentages of individual groups within the 1,941 MAC cases and 1,157 ERA-Interim cases analyzed.

(58.3%) for MAC and 1,250 (64.4%) for ERA-Interim. Moving away from the low center, the ERA-Interim MABL height increases as the distance to the cyclone center increases, and is higher than that of MAC. This is not intuitive, as one might anticipate that high pressure subsidence would be evident far away from the MCMS, forcing a lower inversion height. Unlike ERA-Interim, the median MABL height for MAC decreases from 1,680 m in the 5-10° range to 1,410 m in the 10-15° range.

As discussed, within a synoptic low-pressure system, it is often difficult to identify an inversion as we move closer to the core of the cyclone. In addition, considering that a low percentage of profiles with inversions are found within 5°, it could be hypothesized that significant inversions are rarely present close to the low centers. Figure 3.3a shows the frequencies of no significant inversions as a function of distance from the low center. While the number of soundings varies, the distributions are overall quite similar, with a relative low frequency of no significant inversion presents within the nearest 5°. The ratio of no significant inversion to significant inversion cases is shown in Fig. 3.3b, where it is possible to observe the contrast due to the differences in the detection of inversions between MAC and ERA-Interim. Despite the differences in the number of no significant inversions, a larger ratio is found close to the low centers for both observations and reanalysis. This indicates that, although soundings with no significant inversion increase when moving away from the cyclone core, the proportion of soundings with no significant inversion decreases far away from the cyclone core.

Differences in sample size between the two data sets are analyzed by comparing the results using all soundings with estimates of inversion height from soundings where an inversion is detected in both MAC and ERA-Interim, that is matched cases. The analysis with matched cases shows that the variability of MAC is still greater than that of ERA-Interim. Table 3.2 shows the average of MABL height for MAC all observations, for MAC observations that match the ERA-Interim detection of inversions and ERA-Interim cases, the p values of the t test between MAC matched cases and all the cases are included. On average the MABL height from only cases that match the ERA-Interim inversion detection is 6% lower than the average of all cases (Table 3.2). Regarding the location of soundings, the largest differences of MABL height are located in the northeast quadrant,
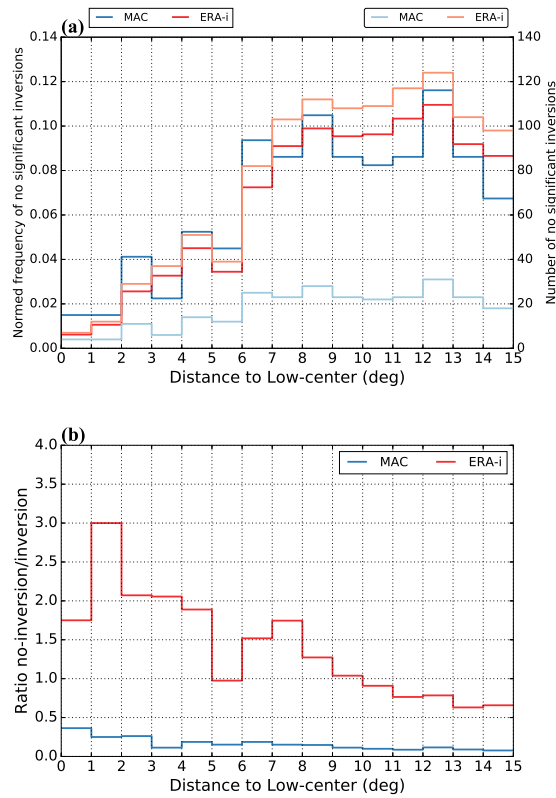
Figure 3.3: (a) Distribution of the relative frequency (left y axis) and number of no significant inversions (right y axis) related to the distance from the low-centers and (b) ratio of no significant inversions to significant inversions. Both graphs are sorted by distance with 1° bins.

and matched cases are on average 7% lower in height than all the cases detected at Macquarie Island. Summer (December–February) and autumn (March–May) show the largest difference in the MABL height by season, 7% and 10% respectively. Winter is the only case where the MABL height of matched ERA-Interim cases is slightly higher than the overall (0.4%). In the differences by distance, the largest percentage is found in the closest 5° bin, with a difference of 13.4%. Hit rates for heavy precipitation are lower than those for light and moderate precipitation. Overall, although there are differences in the MABL heights, these are not statistically significant between the two sample groups (Table 3.2).

3.3.1.2 Precipitation Characteristics

The 6-hr accumulated precipitation (3 hr before and after) is calculated for all soundings within 15° of MAC, independent of whether a significant inversion is detected. Observed surface precipitation characteristics associated with the low centers of the extratropical cyclones are shown in Fig. 3.4. A total of 4,564 cyclone centers within 15° is associated with surface observations regardless of whether an inversion is detected. From this total, 92% (4,206) have records of surface precipitation. Percentages in Fig. 3.4 indicate the ratio of measurements within each quadrant divided by the total number of measurements available. The observed precipitation is lower compared with ERA-Interim, MAC median values are under 0.1 mm, and in the case of the southwest quadrant, the median is 0. The statistics sorted by quadrant show that the mean precipitation amount in the southeast of cyclone cores is much larger compared to the other quadrants (Fig. 3.4). This quadrant also has the largest variability, followed by the northeast quadrant. A closer examination suggests that the high values of accumulated precipitation are most commonly present near the low-pressure center (not shown). Both eastern quadrants are characterized with higher precipitation than western quadrants, consistent with the findings in Bauer and Genio (2006) and Naud et al. (2014), which also show higher moisture amounts in the eastern quadrants of the cyclones using reanalysis data. According to Naud et al. (2014), the maximum precipitation is located along the warm front poleward and eastward of the low-pressure center, where a maximum cloud cover is found using both ERA-Interim and

Table 3.2: Average of MABL heights for MAC all observations, for MAC observations that match the ERA-Interim detection of inversions, percentage of difference between all and matched MAC cases, p values of t test and average of MABL heights for ERA-Interim. Statistics are separated by Quadrant, Season, and Distance from the low center of the cyclone. DJF=December–February; MAM=March–May; JJA=June–August; SON=September–November.

Separation by		MAC height overall (m)	MAC height matched (m)	Difference (%)	p values t test	ERA-Interim height (m)
Quadrant	NE	1,747	1,625	7.0	0.13	1,595
	NW	1,997	1,865	6.6	0.12	1,789
	SW	1,613	1,585	1.7	0.78	1,603
	SE	1,459	1,429	2.1	0.79	1,325
Season	DJF	1,762	1,637	7.1	0.16	1,660
	MAM	1,677	1,507	10.1	0.05	1,437
	JJA	1,623	1,629	-0.4	0.95	1,615
	SON	1,992	1,897	4.8	0.35	1,738
Distance from low	0–5°	1,468	1,272	13.4	0.31	1,045
	5–10°	1,881	1,718	8.7	0.07	1,893
	10–15°	1,735	1,661	4.3	0.19	1,968
Overall		1,762	1,656	6.0		1,610
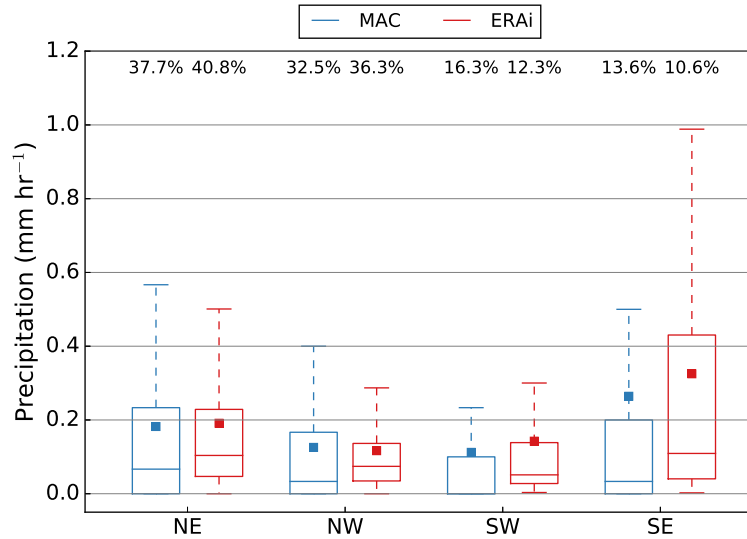
Figure 3.4: Box-and-whisker plots of the mean accumulated precipitation over 3 hr before and after cyclone passage for MAC and ERA-Interim precipitation records. Percentages represent the ratio of precipitation records to the total number of measurements available within each quadrant.

satellite observations.

For the northern quadrants, the variability of the observed precipitation is higher than that of the reanalysis data, whereas the opposite occurs for the southern quadrants. Both the observed median values and lower quartiles are lower than that from the ERA-Interim for all quadrants. Overall, the total annual MAC precipitation for this period (2006–2010) is higher than ERA-Interim precipitation by 16%. This indicates that within a 15° cyclone-centered framework, ERA-Interim overestimates the amount of precipitation over Macquarie Island.

Table 3.3 shows the frequencies of occurrence of MAC and ERA-Interim precipitation for each quadrant and separated by categories. The categories of precipitation are defined as in Wang et al. (2015): light as $0 \leq P < 0.5$ mm hr^{-1}, moderate as $0.5 \leq P < 1.5$ mm hr^{-1}, and heavy as $P \geq 1.5$ mm hr^{-1}. Overall, light and moderate precipitation for both MAC and ERA-Interim are quite comparable in all the quadrants; however, ERA-Interim underestimates the frequencies of occurrence for heavy precipitation. The highest hit rates are obtained for moderate precipitation in NE and NW quadrants (96.5% and 95.8%, respectively). Hit rates for heavy precipitation are lower than those for light and moderate precipitation. In general, ERA-Interim seems to better capture the precipitation below 1.5 mm hr^{-1}, but has limited skills in capturing heavy precipitation around the

cyclone centers.

3.3.2 Synoptic Classification by Cluster Analysis

The cluster analysis ($K = 5$) was applied to all the soundings available at Macquarie Island during the period 2006–2010 that are within 15° of the cyclone cores. Figure 3.5 shows the distribution of each class around the cyclone center, Fig. 3.6 summarizes the properties of each cluster, and Fig. 3.7 shows the mean vertical profiles for each one. Cluster 1, which represents 19.8% of the soundings, exhibits characteristics of a precold front condition. The highest temperature, highest humidity and northwesterly winds are found in this cluster (Fig. 3.7a), corresponding to the warm sector of extratropical cyclones (or the warm conveyor belt). In contrast, Cluster 4 (21.8%) shows characteristics that are consistent with a postfrontal condition in the cold sector of cyclones. The mean (Fig. 3.6b) and vertical profile (Fig. 3.7d) of temperature are the coldest among the clusters. Compared to the other clusters, the dew point temperature profile is significantly drier and relative humidity at the surface has the lowest median. In addition, the change in wind direction to southwesterly is characteristic of postfront conditions. Indeed, the position of the soundings for both clusters shows that most soundings in Cluster 1 (Cluster 4) are located in northeast (northwest) quadrant, which correspond to the warm sector (cold sector) of the cyclones (Fig. 3.5).

Cluster 2 (13.4% of the soundings), represents an environment more closely associated with a high pressure system away from the cyclone core. The surface pressure of this cluster is much higher than other clusters with a mean value of 1,009 hPa. The mean profile of this cluster (Fig. 3.7b) shows a marked decline in the dew point from the surface to ~700 hPa. The easterly wind extends throughout the entire troposphere, with an intensity weaker than other clusters. Unlike Cluster 2, Cluster 3 (16.3% of the soundings) exhibits a larger variability of the surface pressure and the lowest median values (Fig. 3.6a). Wind direction profile shows the northerly winds in the low level and northwesterly winds in the upper level. Within this cluster, the location of most soundings is within 5° from the low centers and to the south side of the cyclone core, indicating a close association with a low pressure system.

Table 3.3: The frequencies of occurrence and hit rates (%) of MAC and ERA-Interim precipitation for each quadrant separated by categories. The three categories for the precipitation are defined as in Wang et al. (2015).

Quadrant	MAC			ERA-Interim			Hits		
	Light	Moderate	Heavy	Light	Moderate	Heavy	Light	Moderate	Heavy
NE	55.4	20.9	23.7	63.6	21.7	14.7	87.1	96.5	62.1
NW	63.2	21.8	15.0	70.6	22.7	6.7	89.5	95.8	44.4
SW	74.6	13.1	11.8	83.8	9.5	6.7	89.0	69.9	56.8
SE	64.0	12.8	23.2	74.6	9.1	16.3	85.9	71.2	70.5
Overall	62.2	18.9	18.9	70.7	18.3	11.0	88.1	97.0	58.4
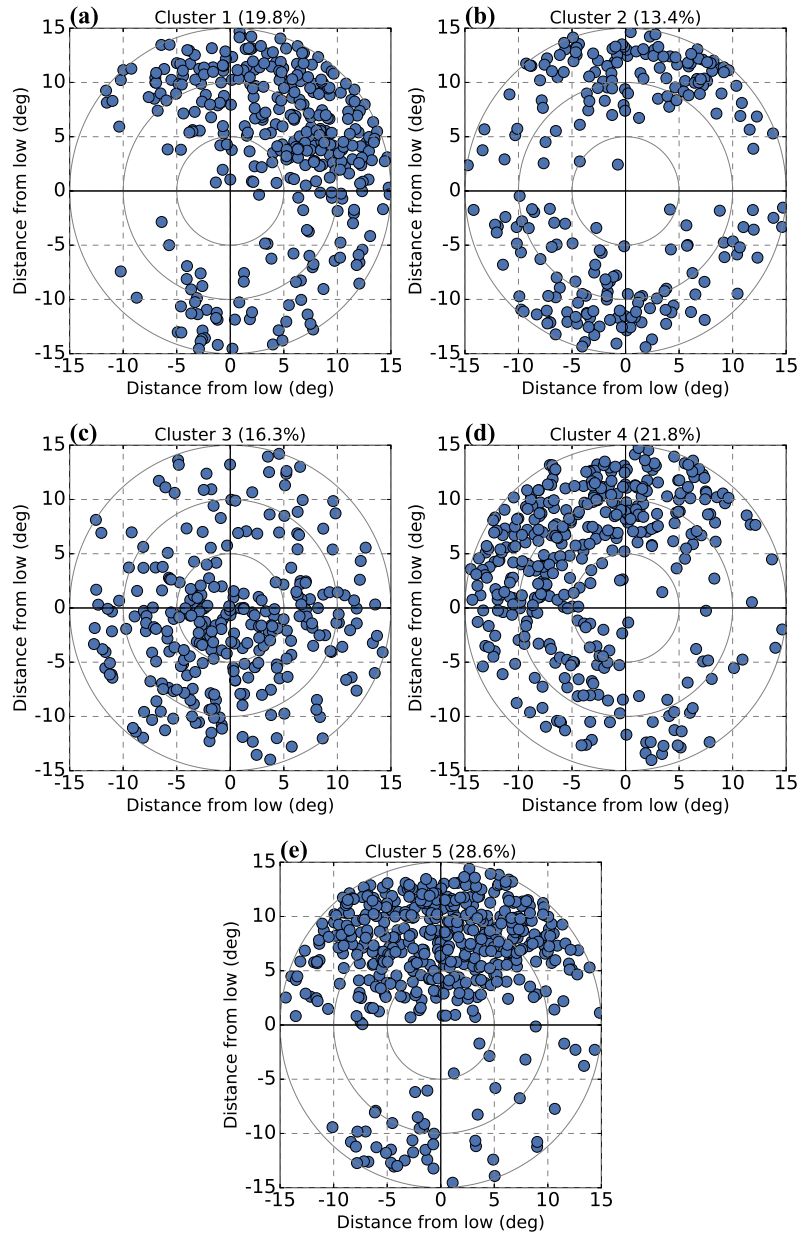
Figure 3.5: Distribution of soundings grouped using cluster analysis in the context of the composite extratropical cyclone (a) Cluster 1, (b) Cluster 2, (c) Cluster 3, (d) Cluster 4, and (e) Cluster 5. Concentric circles indicate distances of 5, 10 and 15° from cyclone center.
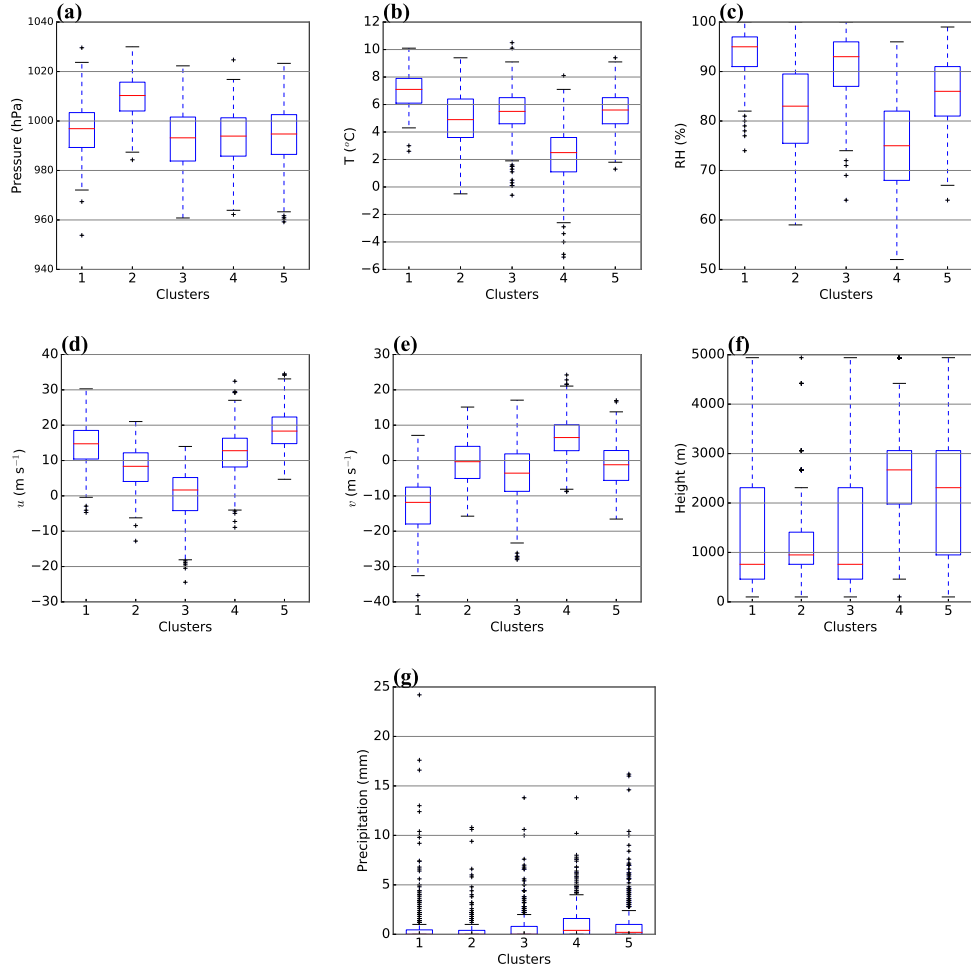
Figure 3.6: Box-and-whisker plots for each cluster of (a) surface pressure, (b) surface temperature, (c) surface relative humidity, (d) zonal wind (u), (e) meridional wind (v) at 925 hPa, (f) calculated inversion height and (g) 6-hr accumulated precipitation.

(a)

(b)

(c)

(d)

(e)
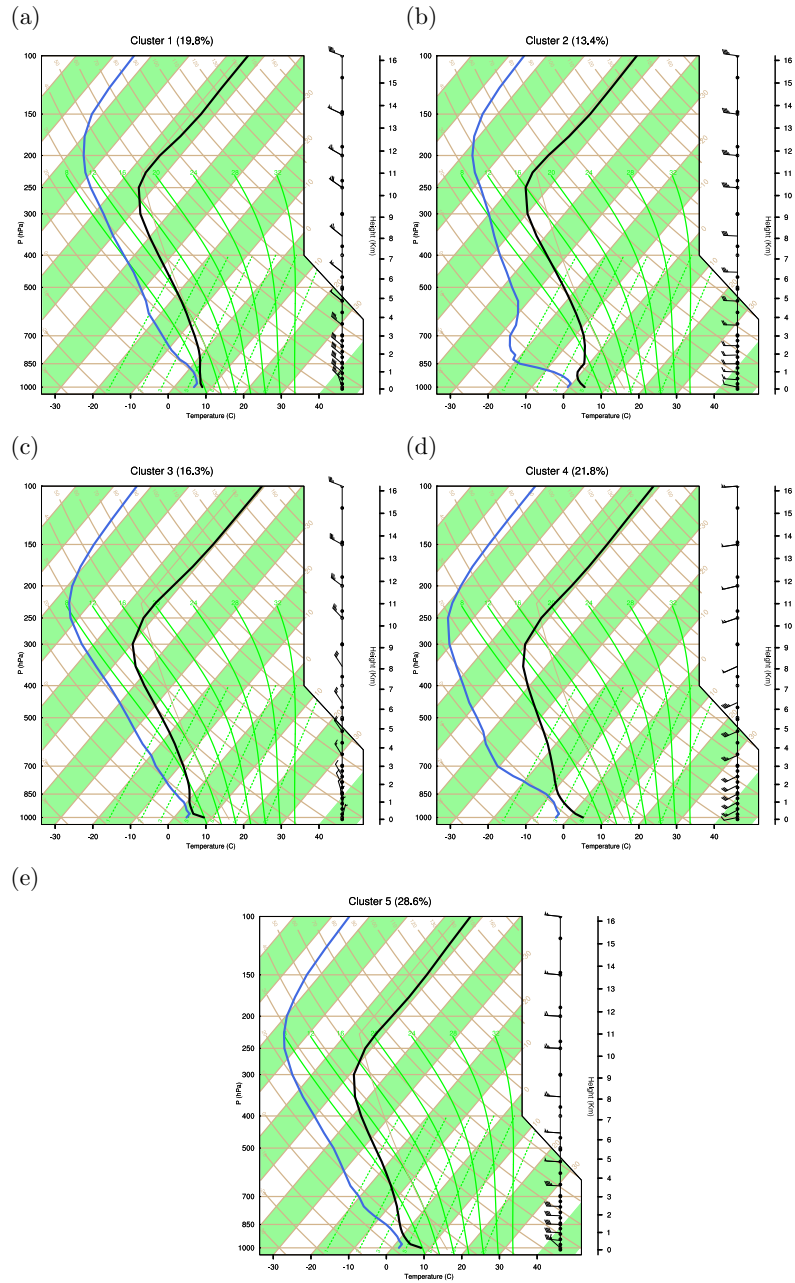
Figure 3.7: (a–e)Mean profiles of temperature and dew point temperature for each cluster, displayed as a skew T-logp diagram and wind profiles.

The most common cluster is Cluster 5, which is identified 28.6% of the time. This cluster is characterized by westerly winds extending throughout the entire atmosphere with a maximum wind speed present at ~650 hPa. Soundings are located mostly at the intersection of the northeast and the northwest quadrants. This cluster exhibits similar characteristics than Cluster 4, yet some differences highlight such as stronger westerly winds (Fig. 3.6d and 3.6e), slightly lower MABL height and accumulated precipitation (Fig. 3.6f and 3.6g). These features and the location of soundings around the cyclone core (Fig. 3.5e) might be associated with a weak postfrontal condition or a frontal zone.

The distribution of MABL height grouped into the five clusters is shown in Fig. 3.6f. Overall, the MABL structure for each cluster is consistent with the corresponding synoptic characteristics as shown in Fig. 3.6a-e. For instance, Cluster 2 is characterized by a low MABL height and smallest variability, which is in response to the large-scale subsidence associated with a high pressure system. In contrast, Cluster 4 (i.e., the cold sector cluster) has the highest MABL, hence deeper mixing and measurably different from Clusters 1 to 3.

Precipitation grouped into the clusters is shown in Fig. 3.6g; values correspond to the accumulated precipitation during the 3 hr before and after each sounding time. Highest values of precipitation are found in Cluster 4, associated with the cold front passage with an average of 1.2 mm and a median of 0.4 mm. Followed by the Cluster 5 (average of 0.9 mm), possibly due to its location within the frontal zone. Lowest distribution values are found in Cluster 2, consistent with the influence of high pressure systems.

3.4 MABL Characteristics and Precipitation in Relation to Cold Fronts

In this section, we investigate the main characteristics of the MABL relative to the distance from a cold front. As mentioned above, during the period from 1995 to 2010, a total of 2,806 upper air soundings is paired with a cold front within 10°. In 2,469 MAC soundings, it is possible to detect a significant inversion related to a cold front. The matching ERA-Interim presents only 791 soundings with a significant inversion (Table 3.1). Figure
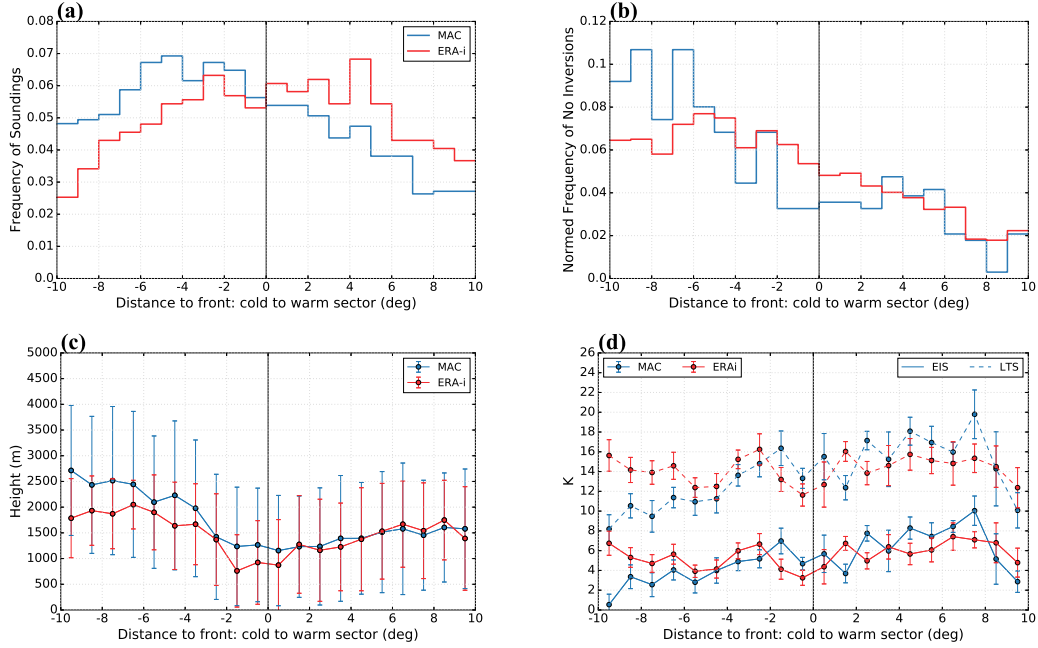
Figure 3.8: (a) Relative frequencies of soundings with a significant inversion across cold fronts related to the total number of sounding available, (b) relative frequency of no significant inversion (c) marine atmospheric boundary layer height across cold fronts and, (d) lower troposphere stability and estimated inversion strength parameters. All graphs are sorted by distance with 1° bins. Error bars show ± one standard deviation.

3.8a shows the relative frequencies of the soundings with a significant inversion across cold fronts. Under prefrontal conditions the frequencies for MAC are lower than for the ERA-Interim, and they decrease as they move away from the front. An opposite behavior can be observed on the postfrontal side, MAC frequencies are higher than for the ERA-Interim soundings, and the distribution of MAC is skewed after the cold front.

Hande et al. (2012b) suggested that profiles with no significant inversions in MAC sounding are related to cases where a front has passed over Macquarie Island. Figure 3.8b shows the relative frequencies of soundings with no significant inversions under cold front passages. The frequency of no significant inversion is higher in both data sets once the front has passed, within the cold sector. At about 5° on the postfrontal side, the frequency of ERA-Interim no significant inversions decreases, which seems to be related to the recovery of the MABL once the cold front has passed. However, the frequency for MAC observations continues to increase to 10°; this behavior is sensitive to the definition of the MABL inversion. We tested the sensitivity of the results to the defined threshold of a significant inversion (not shown). If the inversion threshold was relaxed to values

Table 3.4: Average of MABL height and EIS/LTS parameters by 5° of distance, postcold and precold Front for MAC observations and ERA-Interim profiles.

Zone	Distance cold front	Mean MABL height (m)		EIS/LTS (K)	
		MAC	ERA-Interim	MAC	ERA-Interim
Prefrontal	0–5°	1,547	1,578	2.6/10.1	5.2/14.1
	5–10°	1,275	1,186	5.1/13.8	4.8/13.8
Postfrontal	0–5°	1,640	1,272	6.2/15.6	5.6/14.6
	5–10°	2,420	1,917	6.7/15.4	6.4/14.4

≤ 0.007 K m^{-1}, the MAC distribution of no significant inversions begins to decrease at approximately 5° on the postfrontal side, due to the expected recovery of the MABL and as seen in the ERA-Interim distribution (Fig. 3.8b). Moving the threshold from 0.01 to 0.007 K m^{-1}, the median height shifted from 1,410 m to 1,421 m. Hande et al. (2012b) also tested changes of this threshold, if the inversion threshold was changed to 0.008 K m^{-1}, the median differs by only 1.1%. However, while there are some detailed sensitivities to the inversion threshold, changing the threshold does not change the conclusions of this study.

3.4.1 MABL Height across Cold Fronts

First, we examine the variability of the MABL height across cold fronts using the composites. Figure 3.8c shows the mean height sorted by distance into 1° bins for MAC and ERA-Interim. Along the warm zone (pre-cold-front condition) ERA-Interim is quite consistent with the MAC observations. This can also be seen in Table 3.4 that shows that the difference between the mean MABL heights of the two data sets is less than 100 m. In the postfrontal zone, however, the difference is noticeable. ERA-Interim underestimates the mean MABL height by ∼22%, and the difference increases as the distance from the front increases. Consideration of the MABL height transition from a pre-cold-front to post-cold-front conditions shows a slight decrease of the MABL height as the front approaches the island, once behind the front, in the region of subsidence, the height is initially maintained, then the height grows reaching a higher MABL than in prefrontal conditions. These differences are consistent with the results obtained for cyclones, where the northwest quadrant exhibits the higher MABL inversions (Fig. 3.2a), which corresponds to the cold-air sector following the theoretical schematic in Fig 3.1c.

EIS and LTS are also estimated across cold fronts for all matched cases, with or without significant inversion. As above, the averages of EIS and LTS are sorted by distance into 1° bins for MAC and ERA-Interim (Fig 3.8d). The result of EIS and LTS for MAC shows a clear decreasing transition from the warm sector to the cold sector. Table 3.4 shows a variation of EIS from 6.7 to 2.6 K. The EIS and LTS for cases with a significant inversion show similar characteristics; the results are not sensitive to the cases chosen. Figures 3.8d and Table 3.4 also reveal that unlike the observations, ERA-Interim EIS and LTS do not decrease through the cold front, and their variability is much smaller. Overall, the postfrontal region in MAC has a stronger inversion (more stable conditions) compared with the prefrontal region, which is favorable for the generation of shallow convection. An increase in the inversion strength once the cold front has passed is not evident in ERA-Interim, which may suggest that ERA-Interim features stronger subsidence in the lower troposphere within the postfrontal environment. However, in-situ observations are required to better support this hypothesis, and to further understand the potential link with cloud errors.

3.4.2 Vertical Distribution of Water Content across Cold Fronts

Vertical composite profiles (0–5 km) of specific humidity (q) across a cold front are shown in Fig. 3.9. Unlike the MABL height, the vertical composite profiles are estimated using the total of 2,806 soundings available. The specific humidity is greater along the frontal line and in the prefrontal sector at low levels. To test the significance of the differences when comparing MAC and ERA-Interim profiles, we use a Monte Carlo method by which 90 profiles (the minimum number of soundings available for a given bin from either data set) are randomly selected in each of the one-degree bin from either MAC or the ERA-Interim profiles to produce an across-front vertical profile mean climatology for both data sets. For both MAC and ERA-Interim, this experiment is repeated 1,000 times. The 16-year statistics for the two types of sounding are then compared with the 1,000 trials. The results presented are statistically significant at the 95% confidence level.

The prefrontal zone is clearly observable in both MAC and ERA-Interim composites (Fig. 3.9a and 3.9b), with an increase of specific humidity from approximately 5°
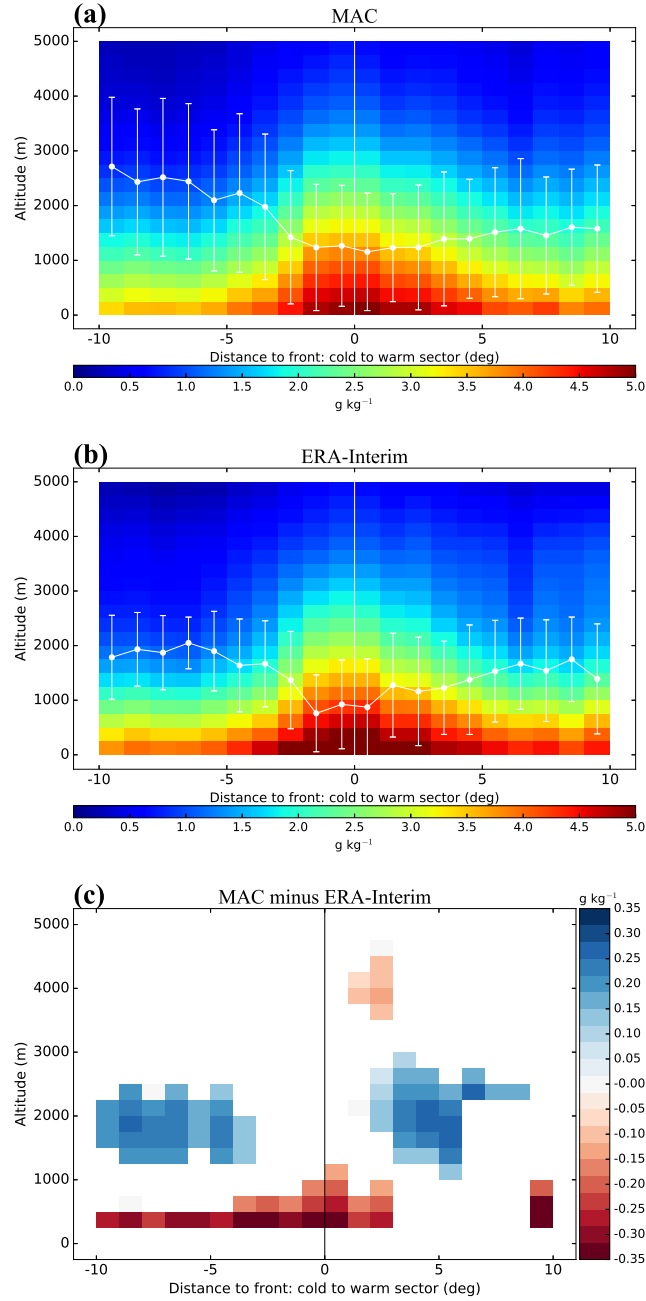
Figure 3.9: Altitude profiles of specific (a) MAC observations, (b) ERA-Interim and (c) statistically significant difference. Distance from cold front is average into 1° bins. Significant differences at 95% confidence level between MAC and ERA-Interim. White lines represent inversion height as Fig. 3.8c.

prefront. Within the cold sector, after the front passage, on average the specify humidity and the precipitation are lower compared with the prefrontal sector (e.g., Bauer and Genio 2006). Qualitatively, ERA-Interim captures the observed variations in humidity. However, significant quantitative differences are found in the moisture profiles within the MABL between the observations and ERA-Interim soundings under both prefront and postfront conditions. Between about 1,000 and 2,000 m, the observed specific humidity is on average 0.3 g kg^{-1} higher than ERA-Interim; in contrast, within the lowest kilometer, the average specific humidity from ERA-Interim is higher by approximately 0.35 g kg^{-1}. Both pre-cold-frontal and post-cold-frontal differences in the amount of water may be too confined in the MABL. Complementary, Fig. 3.10 shows the mean profiles of the potential temperature (θ) and specific humidity for pre- and post-frontal conditions. The y axis is normalized to the height of the main inversion, following Norris (1998a) and Hande et al. (2012b). The largest differences are found for the postfrontal environment (Fig. 3.10b), consistent with Fig 3.9.

The differences between MAC and ERA-Interim suggest that the MABL in the reanalysis data set is too shallow compared to the observations. Accordingly, a lower boundary layer inversion in ERA-Interim indicates that cloud heights are too low compared with observations (e.g., Bodas-Salcedo et al. 2014; Trenberth and Fasullo 2010).

3.4.3 Precipitation in SO Cold Fronts

As with the cyclone analysis, the 6-hr accumulated precipitation is computed for all soundings within 10° of MAC, independently of whether a significant inversion is detected. Figure 3.11 shows the surface precipitation associated with cold fronts. The overall spatial distribution in post-cold-front conditions is very similar for both observations and ERA-Interim. In the midlatitudes, a very high proportion of the precipitation is associated with fronts (Naud et al. 2014). Over the SO, cold fronts contribute over 40% of precipitation, with the largest proportion occurring in spring and winter (Catto et al. 2012). The peak in precipitation under the influence of frontal passages is well represented by the ERA-Interim data set. However, precipitation in pre-cold-front conditions is overestimated by approximate 0.3 mm hr^{-1} by the reanalysis. Under post-cold-front conditions MAC and
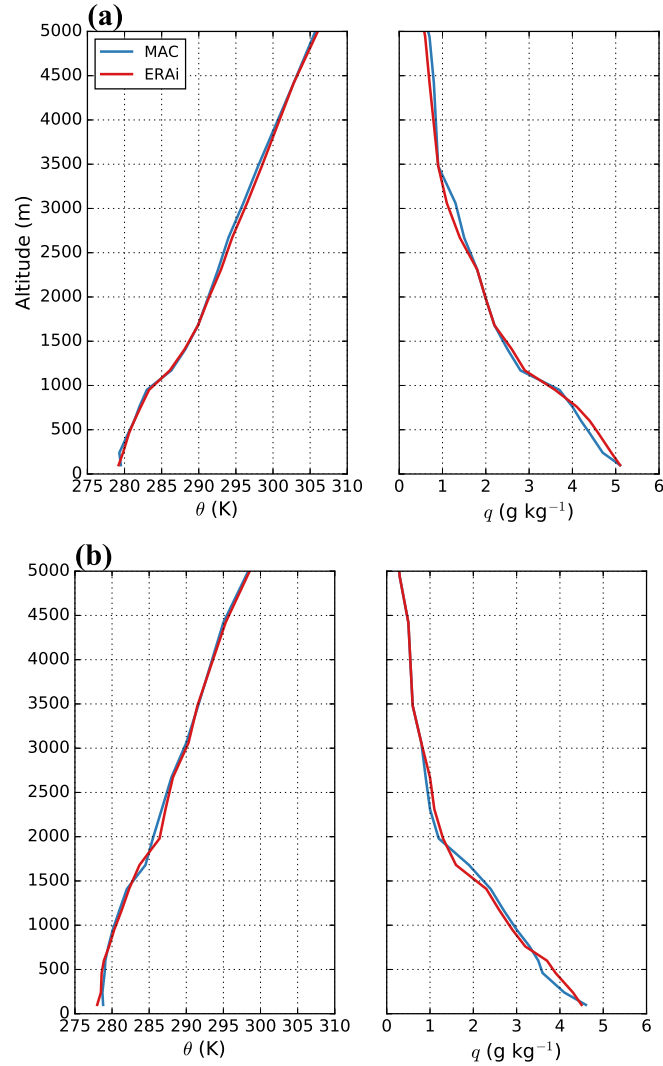
Figure 3.10: (a) Prefrontal and (b) postfrontal mean profiles of potential temperature (θ) and specific humidity (q) normalized to the main inversion height.
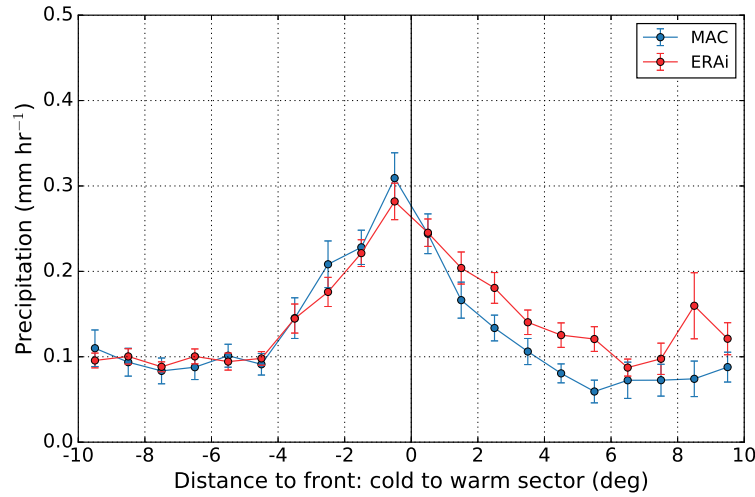
Figure 3.11: Composites of precipitation distribution across cold fronts for MAC and ERA-Interim precipitation records. Values corresponds to the mean accumulated precipitation (3 hr before to 3 hr after) of the cold front. Error bars show ± one standard deviation.

ERA-Interim do not exhibit significant differences in the precipitation, which seem to be unrelated to the differences found in the vertical distribution of specific humidity.

As with the cyclone-centered analysis, the precipitation is overestimated in ERA-Interim near the front; however, as mentioned above, Wang et al. (2015) found that ERA-Interim climatology underestimated the precipitation. Therefore, it is inferred that outside of this 10° frontal zone, ERA-Interim is underestimating the amount of precipitation.

3.5 Discussion and Conclusions

We have employed upper-air sounding and surface precipitation observations from Macquarie Island to examine the thermodynamic structure of the MABL in relation the synoptic meteorology. Specifically we have examined the structure with respect to the displacement from a cyclonic core, as defined by the MCMS data set, and a cold front, as defined by Berry et al. (2011). This analysis has been extended to surface precipitation, too. Thermodynamic profiles and precipitation from the ECMWF ERA-Interim reanalysis were compared with observations to evaluate their representation.

The analysis of cyclones and cold fronts follows a schematic representation of the warm and cold sectors associated with warm and cold fronts in Southern Hemisphere

extratropical cyclones (Fig. 3.1c), consistent with the observational analysis of Govekar et al. (2011). For both cyclones and fronts, a difference is found in the number of significant inversions detected between observations and ERA-Interim reanalysis. This suggests that the reanalysis does not commonly produce a sharp inversion (i.e., "no significant inversion"), even when the MAC observations were interpolated to the same vertical resolution, consistent with the analysis of Hande et al. (2012b). These deficiencies in the detection of significant inversions may have implications for the amount of clouds in the ERA-Interim.

In both observations and the reanalysis, the mean (and median) MABL inversion is higher northward of the MCMS cyclonic core and under postcold front conditions (i.e. the northwest quadrant). Both Naud et al. (2014) and Bodas-Salcedo et al. (2014) characterize the northeast quadrant as predominantly prefrontal, that is, a region of large-scale ascent, dominated by high, thick, and highly reflective cloud. The northwest quadrant is characterized as a postfrontal region of large-scale subsidence. The MABL height decreases slightly as the cold front approaches the island and just behind the cold front the subsidence lowers the top of the atmospheric boundary layer (Bodas-Salcedo et al. 2014).

The evaluation of MABL height has revealed that under cold frontal passages, main inversions are not well represented by ERA-Interim, which underestimates the MABL height by 22%. This result complements the analysis made by Williams et al. (2013). They found that all the models of the Transpose-Atmospheric Model Intercomparison Project II experiment (T-AMIP2; Gates et al. 1999) have an inversion that is too low compared with the ECMWF analyses. These models have large biases on the cold-air side of cyclones (postfrontal) and/or on the leading side of transient ridges, where simulations reveal that, in the T-AMIP2 models, clouds are optically and physically too thin, and inversion heights are typically too low. Our results show that compared with the observations at Macquarie Island, the representation of the MABL in ECMWF ERA-Interim on the postfrontal side is even lower, indicating that bias in the models analyzed by Williams et al. (2013) may even be larger than reported. An accurate representation of the boundary layer structure is directly dependent on the vertical resolution in models and reanalysis data sets, and

the resolution of T-AMIP2 models and ERA-Interim is too coarse to resolve the details of the inversion.

The EIS and LTS parameters were estimated across cold fronts. A relationship between the occurrence of marine low clouds and the static stability of the lower troposphere has been suggested previously. For instance, Naud et al. (2016) examined the relationship between low-level cloud cover and EIS distributions in the post-cold-frontal region at midlatitudes for the two hemispheres (20°–60° N-S). They found that regional and seasonal averages of the cloud cover and EIS are generally well correlated in post-cold-frontal regions. This result is in line with the findings in Wood and Bretherton (2006) regarding the effectiveness of the relationship between cloud amount and EIS at midlatitudes. Similarly, a comparison made in Yue et al. (2011) found that the spatial distributions of LTS and EIS from satellite data agree well with those from ECMWF model analyses in the tropics and subtropics. In this study, we found that the MAC EIS and LTS exhibit striking differences compared with ERA-Interim within the post-cold-frontal area, the MAC EIS is, on average, 23% lower compared with ERA-Interim and MAC LTS 15% lower. This difference is intriguing, because the greater values of the EIS and LTS from ERA-Interim seem to suggest a more stable boundary layer, which could potentially result in a greater cloud cover. On the other hand, however, it could be argued that the observed unstable condition in the cold sector could favor active shallow convection processes for the generation of low-level clouds, although these clouds may be more broken in nature. The higher values of EIS and LTS parameters in ERA-Interim within the lower troposphere may suppress the triggering of shallow convection processes, which may lead to a reduced cloud cover/cloud thinning (Naud et al. 2014). As pointed out in Bodas-Salcedo et al. (2014), the limited skill in representing the MABL could lead to a poor representation of the boundary layer clouds, the radiative cooling at the top of the boundary layer, the evolution of the MABL and the feedbacks into the strength of the inversion (EIS), which generates a shallower boundary layer and thinner clouds. This situation, with reflected shortwave radiation biases, is even less well understood under a multiple-layer structure (Bodas-Salcedo et al. 2014), which has commonly been observed over the SO (e.g., Bates et al. 1998; Boers et al. 1998; Hande et al. 2012b; Russell et al. 1998).

3.5. Discussion and Conclusions

Statistically significant differences were found in the specific humidity within the MABL between the observations and ERA-Interim soundings as influenced by cold frontal passages. Between about 1,000 and 2,000 m above the surface, the observed values are found to be generally higher than ERA-Interim. Within the lowest kilometer, on the other hand, the average specific humidity from ERA-Interim is higher by approximately 0.35 g kg^{-1}, primarily under postfrontal conditions. This high bias in specific humidity near the surface, however, does not lead to higher surface precipitation intensities in ERA-Interim. This disconnection may suggest that ERA-Interim possibly produces too much virga (i.e., where precipitation is produced at cloud base but evaporates before reaching the surface) under postfrontal conditions, as discussed in Ahlgrimm and Forbes (2014) where the ECMWF model was examined, although the compensating effect of other possible errors (e.g., errors in rain-evaporation, autoconversion/accretion parameterizations) cannot be ruled out. Unfortunately, observations needed to further examine these processes, such as cloud and precipitation vertical profiles measured by active remote sensors, are not available at Macquarie Island at the time of this study. As such, our speculation is subject to future investigations where such observations will be obtained from several recent field campaigns. Nevertheless, the presented results suggest that the moisture in the ERA-Interim is too confined to the surface layer, which is consistent with the shallower MABL represented by the ERA-Interim. The observed deficiencies in the ERA-Interim precipitation, added to errors in MABL structure, may be attributed to problems with the parameterizations (e.g., cloud, boundary layer and convection schemes) as suggested in Naud et al. (2014).

The moisture profile differences are consistent with MABL height differences in post-cold frontal conditions. These deficiencies of moisture in the MABL in ERA-Interim reanalysis may be linked with the low cloud amounts in midlatitude oceans in current climate models and atmospheric reanalyses over the SO (Naud et al. 2016; Trenberth and Fasullo 2010). Our findings confirm that there is bias in the MABL structure, with an inversion being too shallow in ERA-Interim. As (Williams et al. 2013) point out, the biases in the MABL structure are consistent with the cloud biases and directly related to the cloud being lower than observed.

Composites across cold fronts and cyclones show an overestimation of precipitation in ERA-Interim (Fig. 3.4 and 3.10); in particular, ERA-Interim precipitation near cyclones and cold fronts is consistently higher than MAC precipitation. However, Wang et al. (2015) found that ERA-Interim precipitation underestimated the annual averaged precipitation as observed at MAC by approximately 6.8%. Precipitation unrelated with cold fronts passages (outside 10°) shows that the annual average of MAC observations during the period 1995–2010 is higher than ERA-Interim by 11%.

Although our findings are heavily dependent on the observations from a single point measurements at Macquarie Island, this study establishes an analytical framework that can be applied to similar data sets available over the SO. In future work, we will extend our current analysis to include recent dedicated field campaigns where observations are made over a more extensive area of the SO.

Chapter 4

Diurnal Cycle of Precipitation and the Marine Atmospheric Boundary Layer over Macquarie Island

4.1 Introduction

With strong winds and waves generated by the Southern Ocean (SO) storm track (Young et al. 2011) and the absence of significant land masses, it is not surprising that the SO has the greatest fractional cloud cover (e.g., Mace et al. 2009) and frequency of precipitation (Behrangi et al. 2012, 2014), zonally averaged, on Earth. These clouds are a fundamental component of the SO energy budget, which is known to have large biases in reanalysis products and climate simulations (e.g., Trenberth and Fasullo 2010). Similarly, the precipitation is a major component of the water budget over the SO, has large uncertainties (Behrangi et al. 2014), and is linked to the energy budget through latent heat fluxes. The uncertainty in the amount of precipitation over the SO can be broken into frequency, intensity (e.g., Stephens et al. 2010; Wang et al. 2015) and location relative to synoptic conditions (e.g., Lang et al. 2018). Catto et al. (2012) coupled the daily Global Precipitation Climatology Project (GPCP, Huffman et al. 2001) precipitation product with a climatology of fronts (Berry et al. 2011) to conclude that 70-90% of the precipitation across the SO was associated with frontal passages. Wang et al. (2015) employed one of the few long-term, precipitation records available over the SO (i.e., Macquarie Island) to

estimate that only ∼60% of the precipitation was associated with frontal passages. Presumably the remaining precipitation comes from the shallow boundary layer clouds found between fronts. Wang et al. (2015) also noted that the ERA-Interim precipitation product underestimated the historic surface observations by ∼7%. High resolution numerical simulations (Wang et al. 2016) suggest that this bias is not likely to be a consequence of orographic processes given the placement of the station and its exposure to common precipitating systems. More recent in-situ observations at the lower latitudes of the SO (Ahn et al. 2017) have found that the shallow post-frontal clouds are commonly lightly precipitating, especially if the clouds are organized as open mesoscale cellular convection.

Shallow maritime boundary layer clouds have been studied extensively across the globe (Wood 2012) given their fundamental importance in the Earth's radiation and water budgets. Some of the earliest studies of these clouds identified a strong diurnal cycle (e.g., Nicholls 1984) whereby the clouds commonly thin throughout the daytime when incoming solar radiation warms the cloud deck. At night, in the absence of solar forcing, the boundary layer can once again becomes well-mixed, and the cloud deck commonly thickens with the renewed access to moisture from the ocean surface. While a diurnal cycle in marine boundary layer clouds has commonly been observed across the globe (e.g., Hignett 1991; Rémillard et al. 2012), it has not been specifically identified over the SO. This is hardly surprising given the lack of suitable long-term observations across the region, a consequence of its harsh environment and remote location.

The presence of a diurnal cycle in the clouds and precipitation over the SO has two immediate consequences. The first consequence is that any diurnal cycle in precipitation provides further insight into the nature of precipitation (frequency, intensity and distribution) over the SO. A diurnal cycle in precipitation may induce a diurnal cycle in surface fluxes. An appreciation of any diurnal cycle in precipitation may be necessary to help resolve its large uncertainty in the widely used precipitation products over the SO (Behrangi et al. 2014). Second, and most importantly, it identifies likely limitations found in virtually any climatology or product that employs the A-train satellite products. The "afternoon train" constellation, by its solar synchronized orbit, passes over the SO in the mid-afternoon, near the peak of any diurnal cycle. Fundamental research over the past

decade on the A-train passive sensors has identified that the fractional cloud cover (e.g., Mace 2010), cloud-top thermodynamic phase (e.g., Hu et al. 2009; Huang et al. 2012a; Morrison et al. 2010) and cloud-droplet number concentration (Bennartz 2007) over the SO may be subject to some unappreciated diurnal cycle. Similarly modelling studies that have used A-train products for evaluation purposes (e.g., Bodas-Salcedo et al. 2012; Huang et al. 2015, 2014) may also have implicit biases. Many of these authors (e.g., Bennartz 2007) readily recognize this potential bias, but there is still no confirmation of its presence or its magnitude.

Macquarie Island (54.62°S, 158.85°E, referred to hereinafter as MAC) is an isolated island in the midst of the SO and provides one of a few long-term observation records in this region; the station is maintained by the Australian Antarctic Division and Bureau of Meteorology. In recent years these records have become quite valuable in improving understanding of the atmospheric conditions over the SO. Adams (2009) examined the trends in the surface precipitation, highlighting a 35% increase in the annual MAC precipitation over the period from 1971 to 2008. The increasing trend in rainfall over Macquarie Island was partially attributed to an increase in cyclonic activity. Such a trend was not evident in the European Centre for Medium-Range Weather Forecasts (ECMWF) ERA-40 reanalysis. Wang et al. (2015) found that a majority ($\sim$30%) of the surface precipitation is relatively weak ($<$0.5 mm hr^{-1}) and arrives predominantly from the west, southwest, and northwest with precipitation from the southwest commonly being drizzle. Heavy precipitation is more likely to be associated with cold fronts, which contribute to more than 50% of the precipitation above 1.5 mm hr^{-1}. They used the MAC observations to "evaluate" CloudSat and ECMWF ERA-Interim reanalysis precipitation products, finding that the frequency of light precipitation is underestimated in both of these products.

In this chapter, we employ long-term MAC field observations to identify the diurnal cycle of the surface precipitation and its relationship with the marine atmospheric boundary layer (MABL) at this site. The analysis is broken into seasons to further reveal its nature. Surface precipitation and thermodynamic profiles from the ECMWF ERA-Interim reanalyses are compared with the observations to evaluate their representation of the diurnal cycle.

4.2 Macquarie Island Observations and ERA-Interim Dataset

Macquarie Island is uniquely situated in the midst of the SO (54.62°S, 158.85°E), approximately half way between Australia and Antarctica. The island is about 34 km long and 5 km wide, primarily north-south-oriented with a peak elevation of 410 m located on the southern part of the island (Jovanovic et al. 2012). A meteorological station, located at the northern end of the island, has been maintained by the Australian Antarctic Division since 1948. Standard surface hourly precipitation and temperature observations are recorded along with twice-daily high resolution upper-air soundings (10-s temporal resolution). The dataset of hourly precipitation and temperature records are available for the period from 1998 through to 2016. Using high-resolution simulations, Wang et al. (2016) demonstrated that the orographic influence of the island on the precipitation records is not significant under the most common synoptic conditions. The minimum detected precipitation is 0.2 mm for the hourly records, values below this threshold are not measured. Consistent with Wang et al. (2015), we define three categories for the precipitation records: "light" precipitation as $0.2 \leq P < 0.5$ mm hr^{-1}, "moderate precipitation" as $0.5 \leq P < 1.5$ mm hr^{-1} and "heavy" precipitation as $P \geq 1.5$ mm hr^{-1}. MAC heavy precipitation is encountered only 1.1% of the time (Wang et al. 2015).

ECMWF ERA-Interim precipitation product is available at a 3-hr temporal resolution and $0.75° \times 0.75°$ spatial resolution and represents a mean precipitation amount over a grid box. For comparison purposes with ERA-Interim, MAC observations are accumulated into 3 hr intervals and used to examine the diurnal cycles of precipitation and temperature. Using typical surface wind speeds of 12-16 m s^{-1}, a 3-hr window of the observed surface precipitation spans ~140 km, which is on the same order of magnitude as ERA-Interim 0.75° (Lang et al. 2018; Wang et al. 2015). Three-hour means (the detection threshold is 0.067 mm hr^{-1}) for annual and seasons are estimated for an inter-seasonal comparison. The magnitude of the diurnal cycle at Macquarie Island is defined as maximum minus minimum 3-hr precipitation rate. This magnitude is tested to be statistically significant at the 95% confidence level, via a Monte Carlo methodology with 10,000 random simulations

to ensure that the diurnal cycles are statistically robust.

The elevation of the sounding launch site is at 8 m above sea level and has a direct exposure to the prevailing westerly winds (Hande et al. 2012b; Wang et al. 2015). The upper-air data set utilised in this analysis covers the period from 1995 through to 2011. During this period, the upper-air soundings were launched twice per day for 95% of all days, comprising 11,610 soundings in total. Consistent with Lang et al. (2018), the high resolution soundings are initially smoothed using a 5-point running average to remove small scale variability. The smoothed profiles are then interpolated on to standard pressure levels (37 pressure levels) for a comparison with ERA-Interim. Via sensitivity tests (not shown), the 5-point smoothing was found to have a minor impact relative to the interpolation on to the 37 pressure levels. Note that no smoothing or interpolation is required for the ERA-Interim profiles.

4.3 Diurnal Cycle of Precipitation

For the time period of 1998-2016, the average annual precipitation was 1,140 mm year^{-1} at MAC and the overall frequency of 3-hr surface precipitation is 34.6%. Looking at the annual average, the 3-hr mean diurnal cycle of surface precipitation over Macquarie Island (Fig. 4.1a) exhibits a maximum during night and early morning, with a peak before sunrise at 0500 local standard time (LST) with a mean of 0.121 mm hr^{-1}. The magnitude of the diurnal cycle is 0.023 mm hr^{-1}, with the minimum at 1400 LST (0.098 mm hr^{-1}); the diurnal magnitude is statistically significantly different from zero at the 95% level. The ERA-Interim reanalysis is able to reproduce many features of the diurnal variations such as the peak at 0500 LST with a mean of 0.130 mm hr^{-1}, yet mean values are overestimated and the diurnal variation is weaker than MAC. The range during the day in ERA-Interim is 0.040 mm hr^{-1} and it is statistically significantly different from zero at the 95% level.

The hourly anomalies for the diurnal cycle of precipitation are estimated from the mean of 1998-2016. Figure 4.1e shows the diurnal anomalies for both observations and ERA-Interim. After sunset the mean observed precipitation anomalies become positive and increase during night until approximately sunrise, during the early morning the sit-
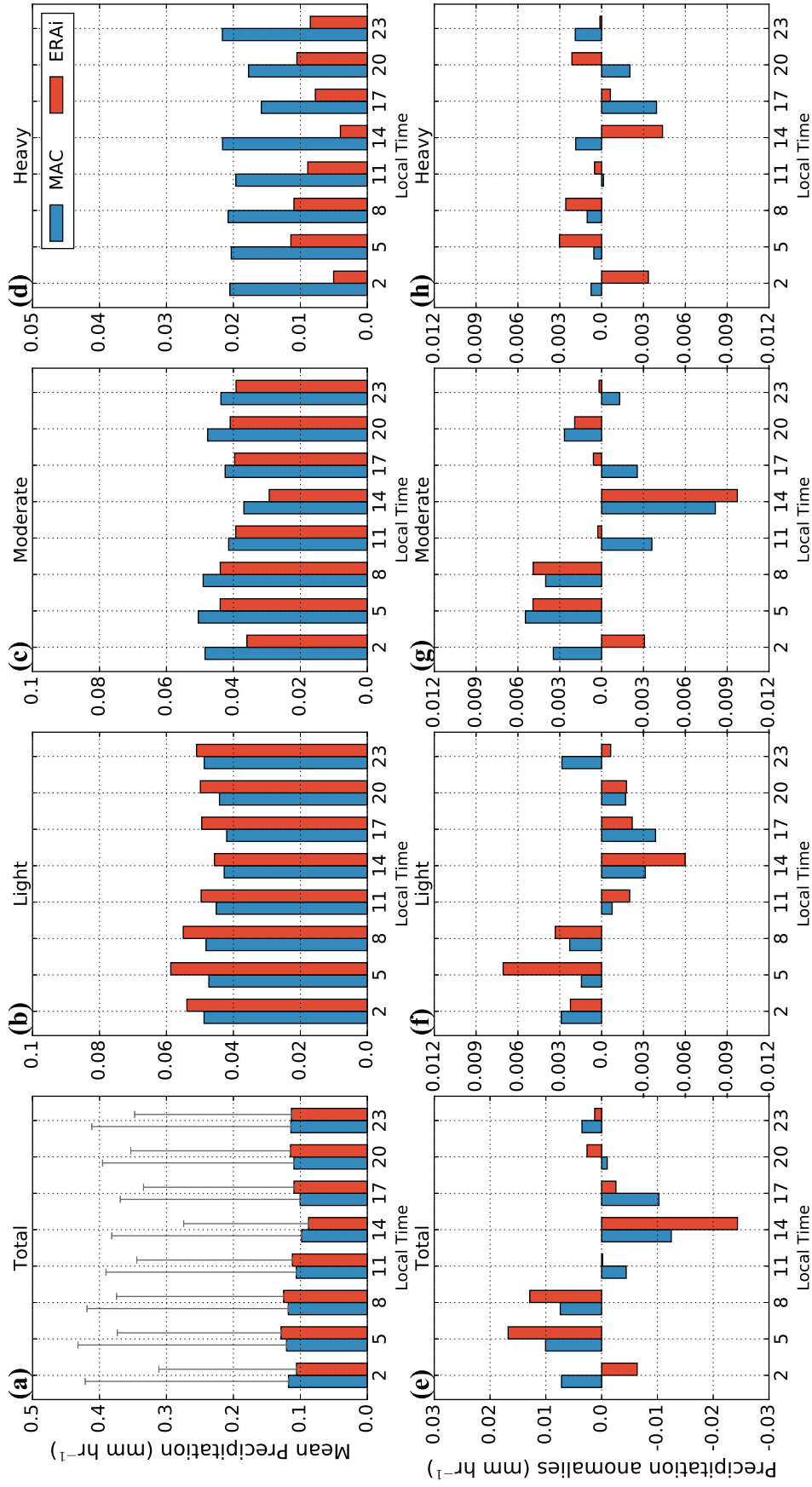
Figure 4.1: Diurnal cycle of precipitation and anomalies for both observations and ERA-Interim profiles, for total precipitation and separated by frequency rates of light ($0.2 \leq P < 0.5$ mm hr^{-1}), moderate ($0.5 \leq P < 1.5$ mm hr^{-1}) and heavy precipitation ($P \geq 1.5$ mm hr^{-1}). Light, moderate and heavy precipitation are normalized by total mean. (a-d) Mean precipitation and (e-h) precipitation anomalies. Error bars show one standard deviation.

uation changes and values decrease below the daily mean.

Despite a reasonable agreement in the mean diurnal precipitation, ERA-Interim does not completely capture the diurnal variation of anomalies, with positive and negative peaks higher than observations. Further, compared with the observations, the magnitude in ERA-Interim is twice as high. We speculate that these biases in the reanalysis dataset might be influenced by the twice-daily initialization of the forecasts at 00:00 and 12:00 UTC (11 and 23 hours LST), which produces a double peak during the cycle and increases the magnitude within a day.

4.3.1 Precipitation Categories

As noted in Wang et al. (2015), light precipitation is commonly present over the SO, contributing approximately 82% of the total precipitation. Our results show that, from 1998 to 2016, light precipitation is recorded 28.3% and 28.8% of the time in MAC observations and ERA-Interim (Table 4.1), respectively. These values are slightly lower than the frequency of 36.4% found in Wang et al. (2015) from 2003 to 2011 for MAC.

The results of the diurnal cycles for each category have been normalized by the total number of hourly measurements for each 3-hr bin. Figures 4.1b,c shows the mean normalized diurnal cycle of light and moderate precipitation for both MAC and ERA-Interim. Compared with the annual diurnal cycle for all precipitation, the magnitude of the diurnal cycle of light precipitation is lower for both MAC and ERA-Interim. The magnitude of the diurnal cycle for MAC light precipitation is 0.007 mm hr^{-1}. For moderate precipitation, the diurnal cycle exhibits similar characteristics compared with the light category, yet ERA-Interim magnitude is lower throughout the day. The observed magnitude is 0.013 mm hr^{-1} for moderate precipitation, and its frequency of occurrence is 5.4% for MAC and 4.5% for ERA-Interim. Both categories present the minimum anomalies at 1400 LST and the maximum at 0500 LST (Fig. 4.1f,g), both consistent with pattern of the total precipitation.

The frequency of the observed heavy precipitation is 0.9%, consistent with Wang et al. (2015); ERA-Interim heavy precipitation represents only 0.4% of the time. The mean normalized diurnal cycle (Fig. 4.1d) and anomalies (Fig. 4.1h) of heavy precipitation for

Table 4.1: Frequency of occurrence for the 3-hr surface precipitation decomposed into the categories defined for MAC and ERA-Interim. Statistics are separated by annual, winter and summer. The categories for the precipitation are defined as Wang et al. (2015).

	Precipitation Category	MAC (%)	ERA-Interim (%)
	Light	28.3	28.7
Annual	Moderate	5.4	4.9
	Heavy	0.9	0.4
	Light	28.2	31.3
Winter	Moderate	4.9	4.3
	Heavy	0.6	0.2
	Light	26.0	24.5
Summer	Moderate	5.1	4.8
	Heavy	1.3	0.8

MAC do not show a clear tendency through of the day. The magnitude of the diurnal cycle at MAC is 0.006 mm hr^{-1} and for ERA-Interim is 0.007 mm hr^{-1}.

Overall, while both light and moderate categories exhibit a noticeable diurnal cycle, heavy precipitation does not. The ERA-Interim is able to reproduce the diurnal cycle, yet the mean normalized diurnal variations for moderate and heavy precipitation are slightly underestimated, while light precipitation is overestimated. The anomalies show that ERA-Interim exhibits a double peak during the cycle for moderate and heavy precipitation, likely due to the twice-daily initialization of the forecasts.

4.3.2 Seasonality

The inter-seasonal variation between Austral summer (Dec-Feb), autumn (Mar-May), winter (Jul-Aug) and spring (Sep-Nov) in both observations and ERA-Interim diurnal cycles is shown in Figure 4.2. A diurnal cycle is appreciated for most of the year; although, as the anomalies show, the diurnal cycle during summer (Fig. 4.2e) is larger compared to the other seasons, and with a magnitude in the same range as the annual diurnal cycle (0.04 mm hr^{-1}), while the ERA-Interim magnitude is slightly higher than observed (0.06 mm hr^{-1}) in summer. Anomalies show larger differences between observations and reanalysis in summer and autumn (Fig. 4.2e,f), specially during early morning and the evening, where ERA-Interim anomalies reach values above 0.01 mm hr^{-1}, while observations only exceed 0.01 mm hr^{-1} once at 0500 LST during summer. Compared

with the other seasons, the wintertime diurnal cycle is relatively flat through much of the day and its magnitude is not statistically significantly different from zero (Fig. 4.2c,d). Consistently, the magnitude of winter diurnal cycle and mean precipitation are lower compared to summer, the climatological monthly precipitation at MAC peaks in early autumn (March and April, ~100 mm month^{-1}) and has a minimum in winter with approximately 78 mm month^{-1} (Wang et al. 2015).

Table 4.1 shows the frequency of precipitation decomposed into the categories defined for winter and summer. Light precipitation is slightly more frequent in winter compared with summer (28.2% and 26.0% of the time respectively). Similarly, ERA-Interim light precipitation is more frequent in winter with 31.3% and 24.5% in summer. For both observations and ERA-Interim, the frequencies show that heavy precipitations is more frequent in summer (1.3% and 0.8%) than winter (0.6% and 0.2%).

4.4 Characteristics of Surface Temperature and MABL

In this section, we analyzed the diurnal signal of surface temperature and MABL to find patterns that could be related with the diurnal cycle of precipitation.

4.4.1 Surface Temperature

The annual diurnal cycle of surface temperature is shown in Fig. 4.3a, the ERA-Interim temperature varies little during the day and does not capture the maximum peak of the temperature observed at 1400 LST. The mean and median values of the observed temperature vary approximately 1.0°C during the day and the mean has a peak of 5.6°C at 1400 LST. The observed temperature peaks coincide with the minimum observed precipitation (Fig. 4.3a). During summer, the observed temperature peaks with a median of 7.8°C at 1400 LST (Fig. 4.3b), consistent with the annual diurnal temperature peak, and the magnitude of the diurnal cycle is 1.6°C. Autumn and spring also show a diurnal cycle as summer, yet the magnitude is lower (Fig. 4.3c,e). No significant variation of diurnal temperature cycle is present during winter (Fig. 4.3d). Overall, the ERA-interim reanalysis is not able to detect a diurnal cycle of temperature as the observed through the year. Sea surface temperature (SST)over the SO does not experience a detectable diurnal
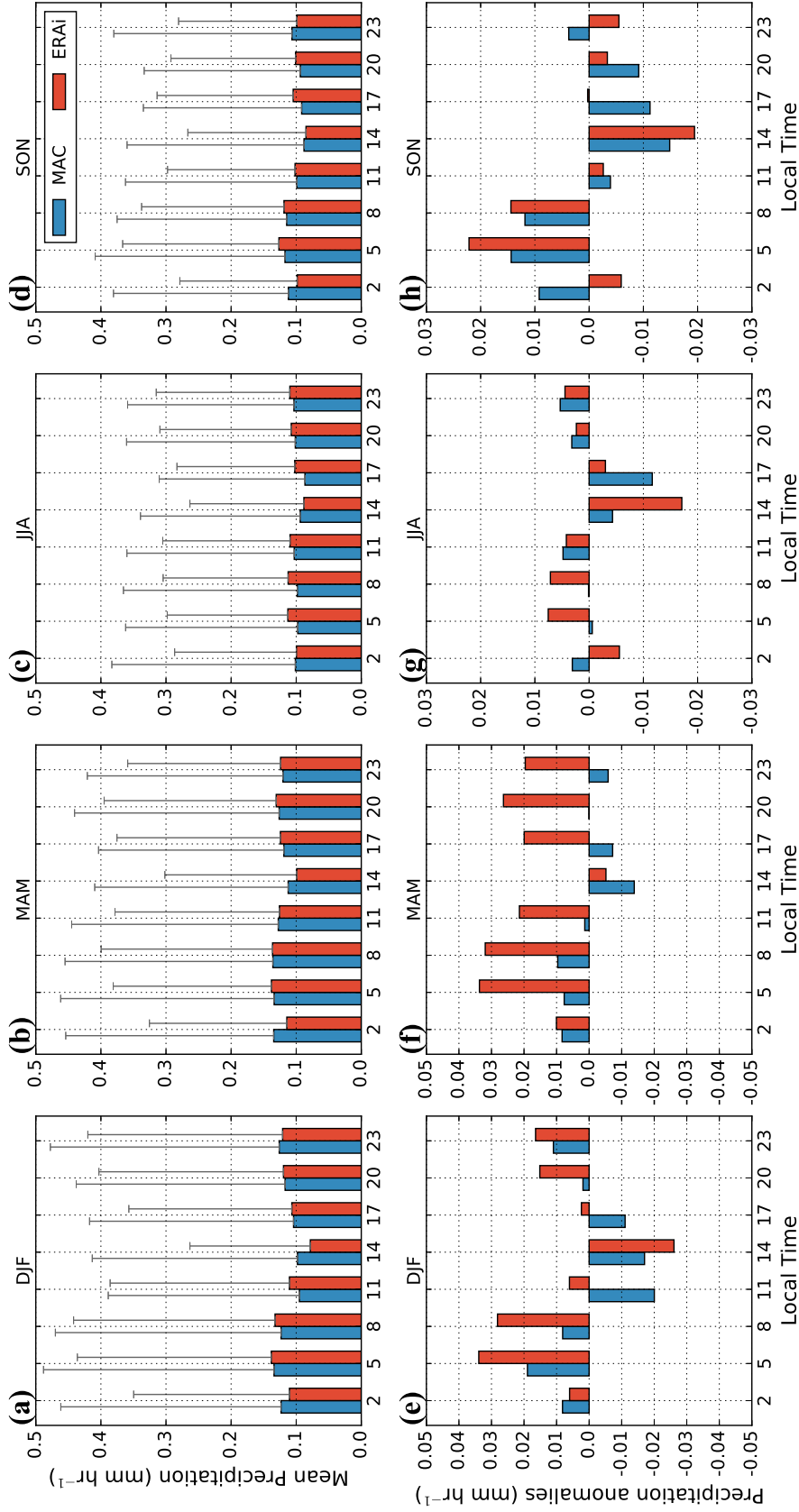
Figure 4.2: Diurnal cycle of precipitation and anomalies for both observations and ERA-Interim profiles, for total precipitation during summer (DJF), autumn (MAM), winter (JJA) and spring (SON). (a-d) Mean precipitation and (e-h) precipitation anomalies. Error bars show one standard deviation.

signal (While et al. 2017), consistently with the lack of diurnal variation of ERA-Interim temperature . This suggest that the diurnal cycles observed both annual and seasonal are likely due to local solar heating at the surface.

4.4.2 MABL

To analyse the relationship of the MABL and the precipitation over Macquarie Island, the mean thermodynamic profiles are compared with the diurnal cycle of precipitation. Figure 4.4 compares the inter-seasonal mean profiles of potential temperature θ and specific humidity q, between the reanalysis and observations. Note that these MAC soundings are only available twice-daily at approximately 0000 and 1200 UTC (11 and 23 hour LST), which may limit the interpretation of the daily signal. Overall, the ERA-Interim bias of θ is rather small, reproducing quite well the profiles. Moisture profiles of q, on the other hand, present significant differences between the surface and ~700 m. The ERA-Interim q during summer is on average 0.3 g kg^{-1} higher than observations. The inter-seasonal comparison shows greater differences in q, with ~1 g kg^{-1} higher during summer and autumn than winter.

Figure 4.4 also shows the mean profiles separated by the launch time, at 0000 UTC and 1200 UTC. For summer, autumn and winter, the observed θ does not show differences between day and nighttime, while during spring, observations shows significant differences between 0000 and 1200 UTC . The observed q is higher at nighttime, on average ~4% in summer and ~2% in winter; statistically significant differences are found in the specific humidity above 2,000 m in summer. Unlike the observations, ERA-Interim reanalysis is not able to reproduce a diurnal variation for q profiles.

4.5 Discussion and Conclusions

A climatology of the diurnal cycle of precipitation has been produced from Macquarie Island surface precipitation observations and the ERA-Interim reanalysis dataset. The main goal of our study is to better understand the nature of the precipitation over the SO and its variability. Our results reveal that over Macquarie Island, the annual and summer diurnal cycles of precipitation exhibit a marked variation throughout the day (20% and
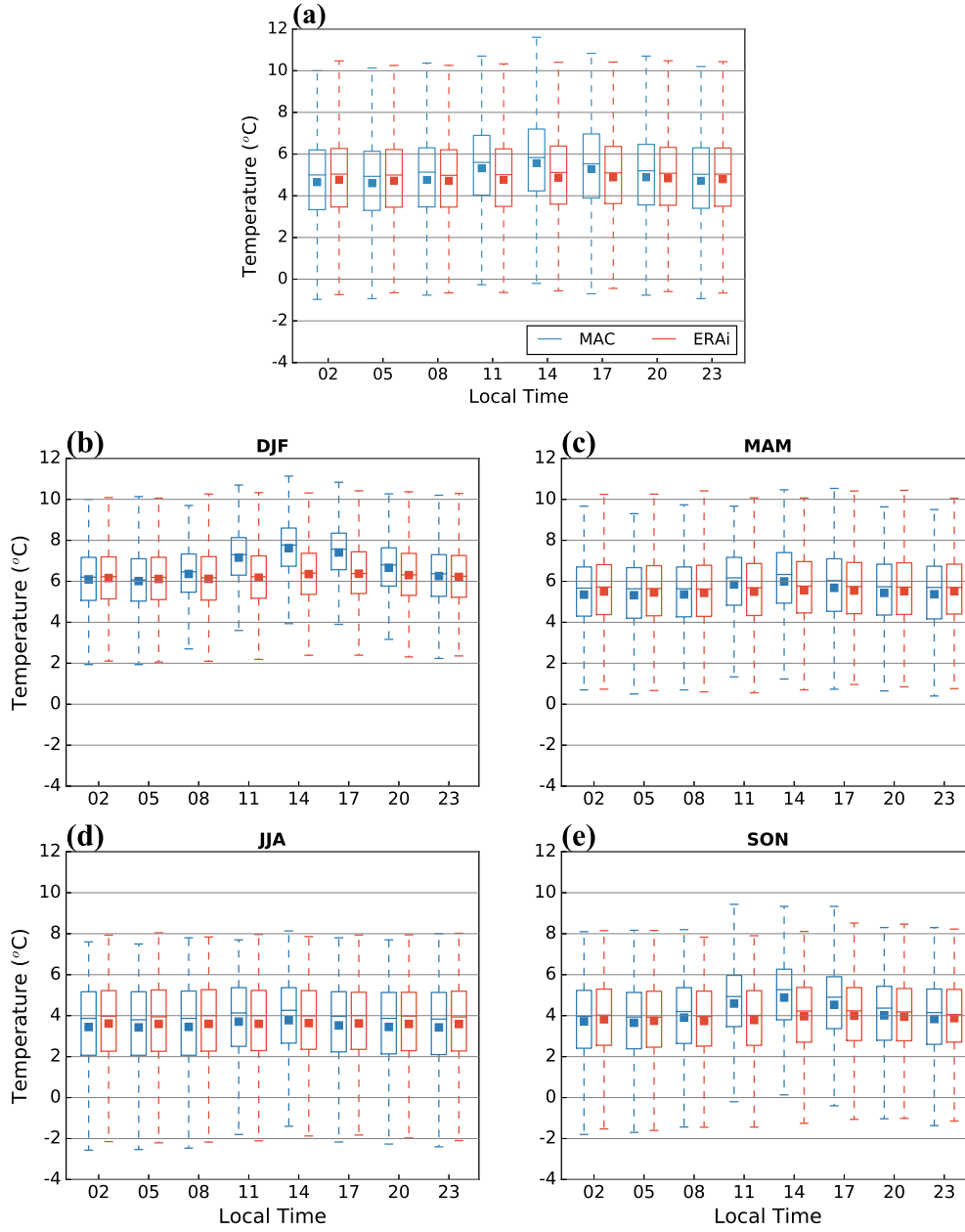
Figure 4.3: Box-and-whisker plots of the diurnal cycle of temperature for observations and ERA-Interim profiles (a) annual, (b) summer (DJF), (c) autumn (MAM), (c) winter (JJA) and (d) spring (SON). The median values are shown as horizontal lines and the mean values as squares. Boxes indicate the interquartile range (25th to 75th percentile) and the whiskers extend to $\pm 2\sigma$ of the standard normal distribution.
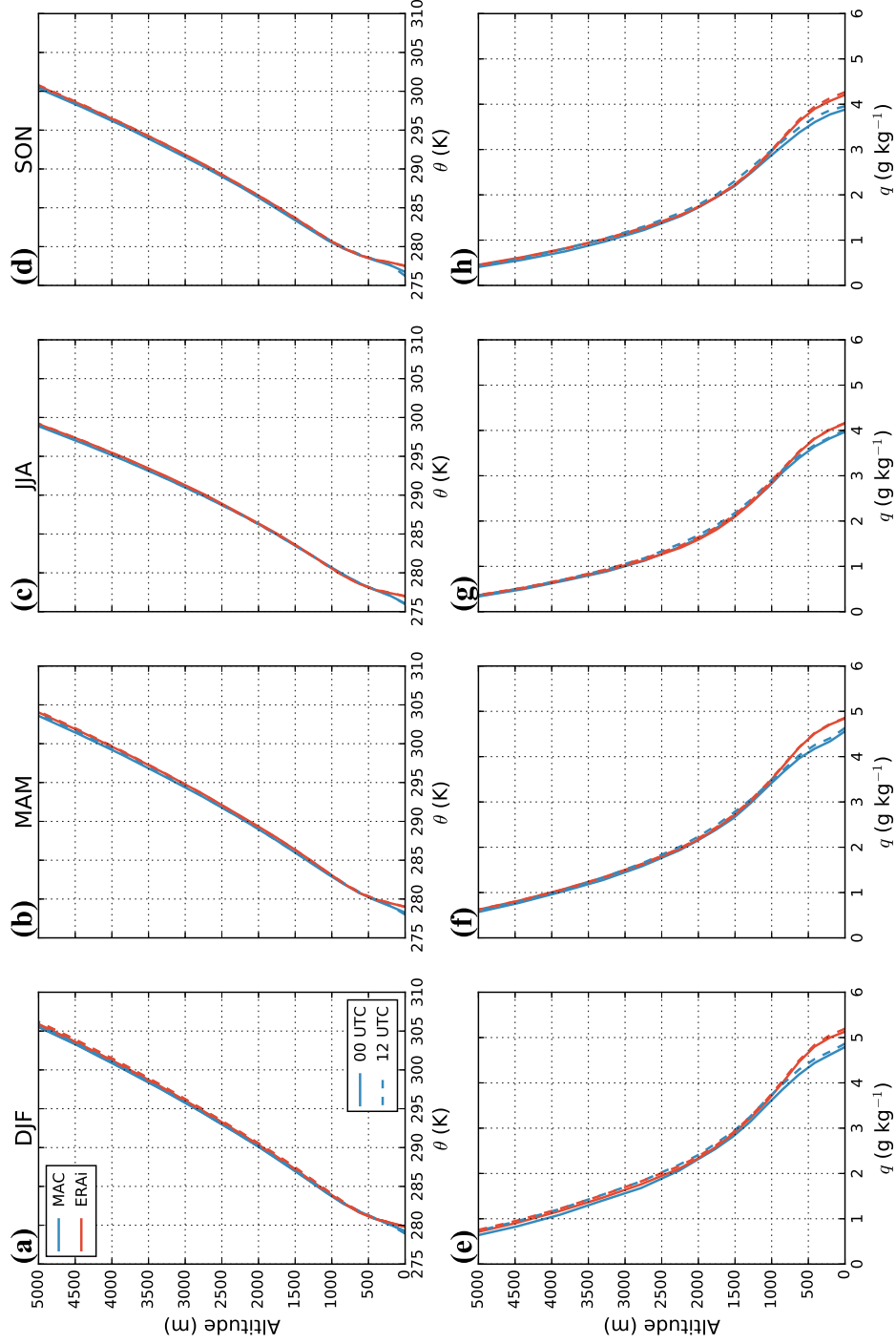
Figure 4.4: Inter-seasonal mean thermodynamic profiles for observations and ERA-Interim reanalysis (a-d) potential temperature (θ) and (e-h) specific humidity (q) at 00:00 UTC (solid lines) and 12:00 UTC (dashed lines)

35% of the mean precipitation respectively), the 3-hr mean precipitation increases after sunset and during night reaching a maximum before sunrise, shortly before dawn at 0500 LST and then decreases until approximately 1400 LST (Fig. 4.1 and 4.2). Such a diurnal cycle is consistent with in situ observations over the oceans between 35°S and 50°S, where precipitation is significantly more frequent at night (Dai 2001; Dai et al. 2007); although, the specific mechanisms that influence the precipitation diurnal cycle over the oceans remain unclear.

Anomalies of light and moderate precipitation show a similar behavior compared with the total precipitation; unlike heavy precipitation, which does not systematically vary though the day. During summer, MAC shows a strong diurnal signal, with a peak before sunrise at 0500 LST, which coincides with the minimum value of daily temperature, such a diurnal cycle during winter time is not evident. Anomalies of heavy precipitation does not exhibit a systematic variation through of the day, which might be due to a diurnal variation of frontal clouds not commonly observed. Wang et al. (2015) estimated that heavy precipitation is not associated with frontal system approximately 20% of the time. Hence, a diurnal cycle in precipitation over the SO suggests that a significant portion of the precipitation might come from non-frontal clouds. Thermodynamic profiles from MAC do not show significant differences between day and nighttime below 2,000 m.

Overall, the mean precipitation and anomalies shows that ERA-Interim has limited skill reproducing a cycle as observed, which may be a consequence of the twice-daily initialization of forecasts. Thermodynamic profiles from ERA-Interim do not show significant differences of θ compared with MAC observations,reproducing the profiles quite well, yet q profiles present significant differences between the surface and $\sim$700 m for both summer and winter seasons. Lang et al. (2018) found similar biases between ERA-Interim and MAC below 1,000 m, under post-cold frontal conditions, where the observed values were found to be generally lower than ERA-Interim; however, a bias between 1,000 and 2,000 m is not noticed. Further, this bias in q near the surface produces higher surface precipitation intensities in ERA-Interim. They suggest that this disconnection between the surface precipitation and the MABL over Macquarie Island may be because ERA-Interim produces too much virga (i.e., where precipitation is produced at cloud base but

evaporates before reaching the surface). Differences over the day within the MABL that could affect the diurnal cycle of surface precipitation are not evident. This results suggest that precipitation differences are possible in response to shallow clouds, which are commonly observed over the SO (Haynes et al. 2011; Huang et al. 2012a).

Our findings shows that a diurnal cycle of precipitation over Macquarie Island exits and it is evident in surface temperature; however, night and daytime soundings do not show temperature differences through the MABL. This cycle peaks in the early morning, so that, A-train products from passive sensors are not able to capture maximum in precipitation when only overpass the SO in the afternoon, restricting any climatology or product that employs these products. In future work, we will extend our current analysis to a more extensive area over the SO, including recent dedicated field campaigns and model simulations.

Chapter 5

Evaluation of WRF Simulations of the Marine Atmospheric Boundary Layer over the Southern Ocean with Shipborne Observations

5.1 Introduction

The Southern Ocean (SO) is covered by extensive areas of marine stratocumulus clouds (e.g, Haynes et al. 2011; Holz et al. 2008; Naud et al. 2014, 2015; Norris and Iacobellis 2005). These marine stratocumulus clouds are generally thin clouds that typically occupy the upper few hundred meters of the boundary layer (Wood 2012), and they play a key role as an important contributors to the global radiation budget because of their high albedo, reflecting incoming solar radiation, thus exerting a strong negative shortwave radiative effect (e.g, Klein and Hartmann 1993). Marine stratocumulus clouds are commonly observed in post-frontal environments (Haynes et al. 2011). Bodas-Salcedo et al. (2012) examined the UK Met Office Unified Model (MetUM) and highlighted that the underprediction of the low- and mid-level clouds in the cold sector of mid-latitude cyclones over the SO contributes to the largest reflected short-wave radiation biases in this region. Naud et al. (2014) found that the European Centre for Medium-Range Weather Forecasts (ECMWF) ERA-Interim reanalysis (Dee et al. 2011) and the NASA Modern-Era Retrospective Analysis for Research and Applications (MERRA) do not produce enough cloud cover in the cold sector of cyclones. In order to better understand biases in the

boundary layer clouds, it is necessary to understand if the boundary layer structure is properly represented in models.

Mesoscale numerical weather prediction (NWP) models have been widely used to study boundary layer clouds (e.g, Huang et al. 2014; Morrison et al. 2010) and precipitation (e.g, Wang et al. 2016) over the SO. Morrison et al. (2010) simulated mixed-phase clouds off the coast of Tasmania and found that a major difficulty in modeling clouds containing supercooled liquid water (SLW) is because the inability of the reanalysis products employed for model initialization, to reproduce the wind shear and temperature inversion through the marine atmospheric boundary layer (MABL). Huang et al. (2014) used the WRF model to simulate boundary layer clouds over the SO and Tasmania. They suggested that the model deficiency to simulated boundary layer clouds in this region may be associated with the insufficient surface moisture flux.

A major impediment in the evaluation of model simulations of MABL structure over the SO has been the absence of in situ observations (Hande et al. 2012b; Huang et al. 2014). Field experiments with in situ observations of MABL and low-altitude clouds over the SO such as the Aerosol Characterization Experiment (ACE-1, Bates et al. 1998) and the Southern Ocean Cloud Experiments (SOCEX I and II, Boers et al. 1998) date back to 1995 and earlier. Other observations have generally been limited to infrequent and isolated, such as on board local ships (e.g, Kanitz et al. 2011) and aircraft with limited instrumentation (e.g, Ahn et al. 2017; Chubb et al. 2016, 2013; Huang et al. 2015). In recent years, new projects such as the Clouds, Aerosols, Precipitation, Radiation, and atmospherIc Composition Over the southeRn oceaN (CAPRICORN), which involved two one-month cruises into the SO during austral summer 2015-2016 and the Southern Ocean Cloud Radiation and Aerosol Transport Experimental Studies (SOCRATES) during early 2018, have provided new in situ observations to understanding the unique nature of the atmospheric processes over the SO.

The aims of this study are first, to present the recent in situ observations from the 2016 CAPRICORN field campaign and characterize the boundary layer clouds and the MABL structure over the remote SO. Second, to evaluate the Weather Research and Forecasting (WRF) NWP model employing these in situ observations together with selected satellite

observations. The present study is a detailed investigation of two case studies: a rapid succession of two cold fronts on 21-23 March 2016 characterized by shallow convective warm clouds and light precipitation originating from the pre-frontal shallow convection; and a sustained period of open mesoscale cellular convection (MCC) in a post-frontal environment on 26-28 March 2016 with mixed phase cloud in a sub-freezing temperature range and relatively heavy precipitation. The first case corresponds to the longest cold front observed during the cruise and with the highest number of radiosonde launches; while the second cases corresponds the longest period of open MCC.

5.2 Data and Methods

5.2.1 Shipborne Observations

From 14 March to 16 April 2016, the MNF Research Vessel (R/V) Investigator conducted a research voyage in the SO as part of the Clouds, Aerosols, Precipitation, Radiation, and atmospherIc Composition Over the southeRn oceaN (CAPRICORN) project. The scientific goals of CAPRICORN are: (i) characterize the cloud, aerosol, and precipitation properties, boundary layer structure, atmospheric composition, and surface energy budget, as well as their latitudinal variability; (ii) evaluate and improve satellite estimations of these properties, and (iii) evaluate and improve the representation of these properties in the Australian Community Climate and Earth-System Simulator (ACCESS) regional and global model. The CAPRICORN 2016 observations span latitudes from 43°S to 53°S and longitudes from 141°E to 151°E.

5.2.1.1 Shipborne Instrumentation

The R/V Investigator collects 10-min and 1-hr averaged meteorological observations with the NOAA ESRL PSD's flux system. NOAA's flux system is an instrument package that makes direct measurements of the exchange or flux of heat, water, and momentum between the atmosphere and the ocean. The system also measures meteorological variables such temperature, relative humidity, wind, pressure, precipitation, short- and long-wave down-welling radiation, and sea surface temperature. Cloud radar reflectivity measurements

are collected with the 95-GHz Doppler cloud radar called the Bistatic Radar System for Atmospheric Studies (BASTA, Delanoë et al. 2016) from 0 to 12 km height in clouds and precipitation, at a temporal resolution of 12 s and four vertical resolutions (12.5, 25, 100 and 200 m). Lidar backscatter and linear depolarization vertical profiles from 0 to 12 km height are collected with the RMAN-511 cloud and aerosol lidar. The horizontal and temporal resolutions are 15 m and 1 min. Profiles of pressure, temperature, humidity and horizontal winds are measured with radiosondes launched approximately once daily, except in cases of front and severe weather, where more are launched. During the voyage, 31 upper-air radiosondes were launched.

5.2.1.2 Case Studies

Two cases are examined in this study with a focus on shallow convective clouds that were commonly observed during the cruise. First (case A), an elongated cold front approaches Tasmania from the west on 22 March 2016 (Fig. 5.1a,b) with a secondary weaker cold front immediately after. The shipborne observations of winds and pressure suggest that the major shift arrived at approximately 1800 UTC. The low pressure center of the secondary front is situated at ∼54°S, while the main front occupies a wide latitude band with the low pressure center situated beyond 55°S, far to the south of Tasmania near the Antarctic coast. For a period of approximately 26 hours during the front passages, eight soundings were launched to analyse the atmospheric structure across the fronts. This case study offers an ideal cold-frontal passage characterized by shallow convective warm clouds and light precipitation originating from the pre-frontal shallow convection.

The second case (case B) focuses on a sustained period of open mesoscale cellular convection (MCC) in a post-frontal environment (Fig. 5.1c,d). Figure 5.1d shows that a cold front has passed through Tasmania on 26 March 2016, leaving Tasmania and its surrounding ocean exposed in a post-frontal field of open MCC. Mixed-phase cloud fields, primarily below 2.5 km, were observed by the shipborne radar-lidar, with relatively heavy precipitation. Three soundings were launched during the period of open MCC.

(a)

Channel 13-IR1 22-03-2016 12:00:00

(b)

(c)

Channel 13-IR1 2016-03-26 00:00:00

(d)

—
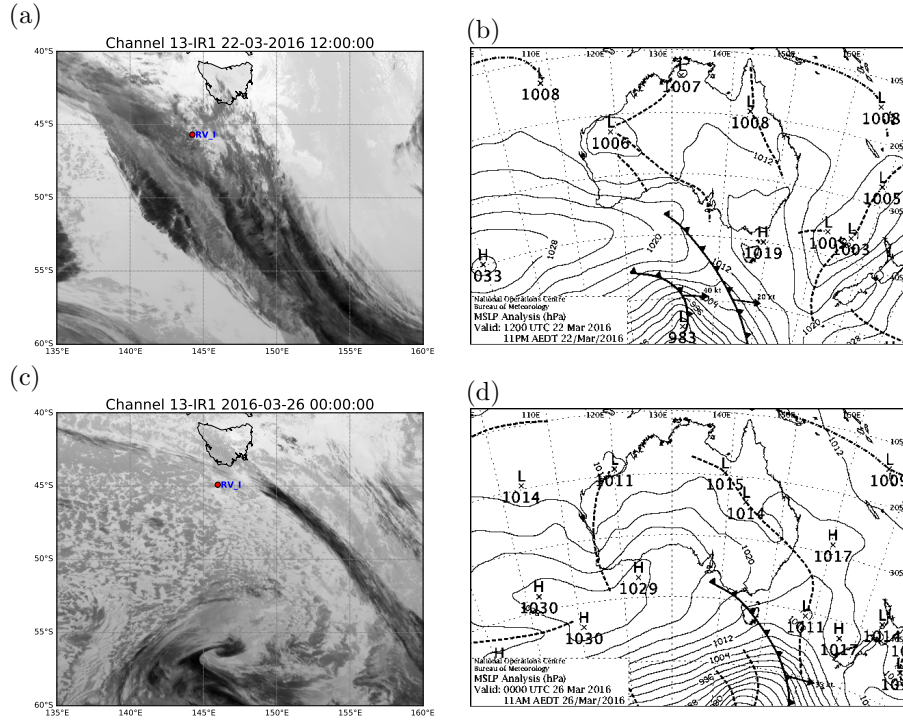
Figure 5.1: The HIMAWARI-8 Infrared Channel 13 and the mean sea level pressure (MSLP) analysis provided by the Australian Bureau of Meteorology for both cases. (a,b) at 1200 UTC 22 March and (c,d) at 0000 UTC 26 March. Location of R/V Investigator (RV_I) is show in (a) and (c)

5.2.2 Himawari-8 Products

Himawari-8 is a geostationary member of the Multifunction Transport Satellite series (Da 2015) designed for meteorological applications and is administered by the Japan Meteorological Agency. The Advanced Himawari Imager (AHI) on Himawari-8 measures radiances at 16 wavelengths ranging from 0.47 μm to 13.3 μm (16 channels including visible and infrared bands), at a spatial resolution of 0.5 km-2 km and a temporal resolution of 10 min-2.5 min. The Himawari-8 cloud products are used in this study to evaluate WRF simulations.

Data sets employed in this study include the cloud-top phase (CTP) and the cloud-top temperature (CTT). These cloud products are based on the GOES-R Advanced Baseline Imager (ABI) cloud algorithm of the National Oceanic and Atmospheric Administration (NOAA) and the National Environmental Satellite, Data, and Information Service (NESDIS, Pavolonis 2010). The cloud type/phase algorithm utilizes several spectral and spatial tests to determine the cloud type (liquid water, supercooled water, mixed phase and ice)

through infrared channels: 10 (7.4 μm), 11 (8.5 μm), 14 (11 μm), and 15 (12 μm). A simple diagnostic scheme is used to enable a direct comparison between Himawari-8 satellite observations and the simulations. The scheme is based on the relative fraction of liquid water to total water (RLW) was employed to define the simulated cloud phase as liquid ($RLW > 0.7$), mixed phase ($0.3 \leq RLW \leq 0.7$), or glaciated ($RLW < 0.3$) (Huang et al. 2018, 2014). Cloud top defined at 0.1 cloud optical thickness from the top of the model is employed to examine cloud-top properties (Huang et al. 2014).

5.2.3 Experimental Design of Numerical Simulations

The case studies described above are used to evaluate the WRF model over the SO. The dynamical core used was the Advanced Research WRF (ARW) version 3.9.1, which is based on non-hydrostatic Euler equations, designed for both mesoscale atmospheric research and operational forecasting needs (Skamarock et al. 2008). In this work, for both case studies, the model is configured with an outer domain and three one-way nested domains, which were applied with a horizontal spacing of 27, 9, 3, and 1 km, and with 64 η-levels, with approximately 30 levels below 2.5 km. For both cases, the outer domain covers a broad area of the SO between approximately 35° and 60° S, and the first nested domain incorporated Tasmania and its surrounding west and south oceans. The two inner domains are centered to capture the ship tracks during each case (Fig. 5.2). The initial and lateral boundary conditions in all experiments for the simulations were derived from the Interim European Centre for Medium-Range Weather Forecasts (ECMWF) ERA-Interim reanalysis (0.75° x 0.75° grid, 37 pressure levels, and 6-hourly updates) (Dee et al. 2011). For case A, the simulation was initialized at 0600 UTC 21 March 2016 and ran for a period of 60 h. The simulation for case B is 72 h and was initialized at 0000 UTC 25 March 2016. A 12-h spin-up period is used to prevent any noisy outputs during the period of model stabilization for both cases.

For the base simulation, we used the WRF configuration employed in previous studies over the SO (e.g., Huang et al. 2014; Wang et al. 2016). This configuration includes the Rapid Radiative Transfer Model for GCMs (RRTMG) shortwave and longwave radiation scheme (Iacono et al. 2008; Mlawer et al. 1997), the Noah land surface model (Chen and
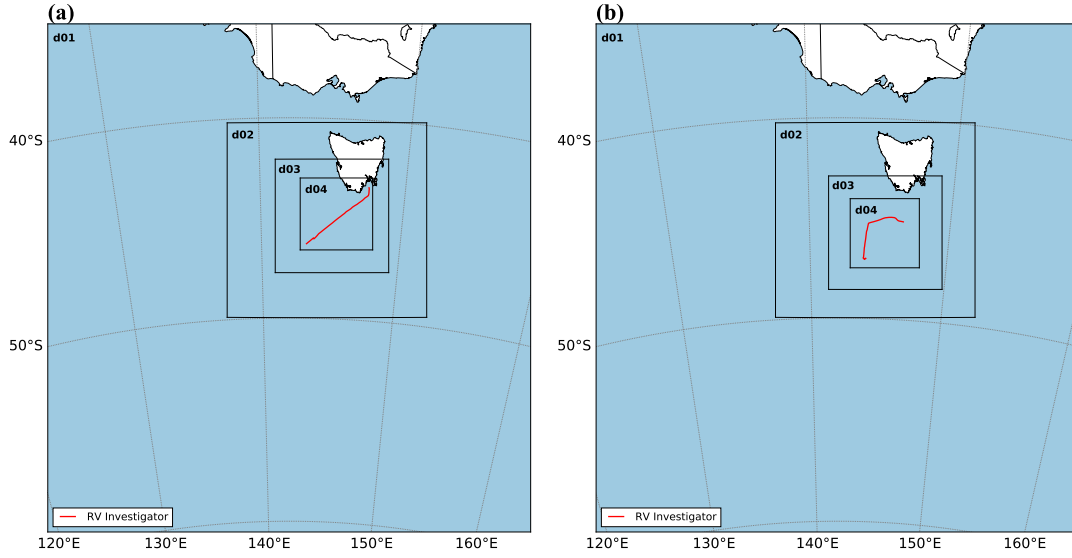
Figure 5.2: Maps showing WRF domain settings with R/V Investigator tracks for (a) case A and (b) case B.

Dudhia 2001), Yonsei University (YSU, Hong et al. 2006) planetary boundary layer (PBL) scheme, the new Thompson (Thompson et al. 2008) microphysical (MP) scheme, and the Simplified Arakawa-Schubert (SAS) cumulus scheme (Pan and Wu 1995), which is used only on the two coarsest domains (27 and 9 km).

Different parameterizations were used in the model run for each case to examine the sensitivity of the simulations to PBL and MP schemes. Table 5.1 details the different schemes that were combined, varying the PBL: Yonsei University (YSU), Mellor-Yamada-Janjic (MYJ, Mellor and Yamada 1982) and the asymmetric convective model, version 2, (ACM2, Pleim 2007); and the MP: new Thompson, Morrison 2-mom (Morrison et al. 2009), the WRF Double-Moment 6-class (WDM6, Lim and Hong 2010) and the WRF Single-Moment 5-class (WSM5, Hong et al. 2004). We identify differences in model performances with possible consequences for marine atmospheric boundary layer (MABL) clouds simulations and seek an understanding of those differences. Table 5.2 shows the different combinations of schemes tested and their respective nomenclatures.

The three PBL schemes are used to parameterize the unresolved turbulent vertical fluxes of momentum, heat, and constituents such as moisture within the PBL. Closure schemes are used to estimated the mean values of turbulent fluxes (Holt and Raman 1988). The YSU and ACM2 schemes are first-order closure schemes, since they do not require any

Table 5.1: Planetary boundary layer (PBL) and microphysical (MP) schemes used for the numerical simulations

Scheme	Main features	Reference
PBL schemes:		
Yonsei University (YSU)	Non-local, first order closure	Hong et al. (2006)
Mellor-Yamada-Janjic (MYJ)	TKE, 1.5 order closure	Mellor and Yamada (1982)
Asymetric Convective Model, version 2 (ACM2)	Non-local, first order closure	Pleim (2007)
MP schemes:		
New Thompson	Double-moment ice, snow, rain and graupel for cloud-resolving simulations, 6-class	Thompson et al. (2008)
Morrison 2-mom	Double-moment rain, ice, snow and grapel.	Morrison et al. (2009)
WRF Double-Moment 6-class (WDM6)	Double-moment rain. Cloud and CCN for warm processes, 6-class.	Lim and Hong (2010)
WRF Single-Moment 5-class (WSM5)	Single-moment with ice and snow, 5-class.	Hong et al. (2004)

Table 5.2: Parameterization combinations and nomenclature to perform the physics for numerical simulations of the two cases.

Case	ID	PBL scheme	MP scheme
A	CA_C	YSU	New Thompson
	CA_C_WDM6	YSU	WDM6
	CA_C_MOR	YSU	Morrison
	CA_C_WSM5	YSU	WSM5
	CA_MYJ_C	MYJ	New Thompson
	CA_ACM2_C	ACM2	New Thompson
B	CB_C	YSU	New Thompson
	CB_C_WDM6	YSU	WDM6
	CB_C_MOR	YSU	Morrison
	CB_C_WSM5	YSU	WSM5
	CB_MYJ_C	MYJ	New Thompson
	CB_ACM2_C	ACM2	New Thompson

additional prognostic equations to express the effects of turbulence on mean variables. The YSU is characterized as a non-local closure scheme and uses the Monin-Obukhov surface layer scheme (Hu et al. 2010). The most important characteristic of the YSU algorithm is the explicit treatment of entrainment processes at the top of the PBL; at the inversion layer an asymptotic entrainment flux term proportional to the surface flux is included. The selection of this scheme is based on its use as default model configuration in studies over the SO (e.g., Huang et al. 2014; Wang et al. 2016). The ACM2 scheme is a modified version of the original ACM1 scheme (Pleim and Chang 1992), which includes a first-order eddy-diffusion component to improve the shape of vertical profiles near the surface, which may offer some insights simulating shallow convective clouds. The ACM2 treats non-local fluxes using a transilient matrix. This definition for non-local fluxes intended to be more applicable to other quantities such as humidity, winds, or trace chemical mixing ratios in addition to heat components (Pleim 2007). Unlike YSU and ACM2, the MYJ scheme is a local closure model. This scheme uses the Janjic Eta Monin-Obukhov surface layer scheme and the 1.5-order turbulence closure model of Mellor and Yamada (1982) to represent turbulence above the surface layer (Janić 2001). Local closure schemes like MYJ estimate the turbulent fluxes at each grid point from the mean values of atmospheric variables and/or their gradients at that grid point. This type of PBL schemes determines eddy diffusion coefficients from prognostic turbulent kinetic energy (TKE), they are also called TKE closure schemes. This scheme was previously used over the SO by Morrison et al. (2010).

5.3   Results

5.3.1   Case A: MABL Clouds Under Cold-frontal Passages

A succession of two fronts is approaching Tasmania from the west on 22 March 2016 (Fig. 5.1b). Figure 3 shows the pre-frontal area for case A at 0000 UTC 22 March over domain 3 of the WRF simulation and its respective area from Himawari-8 satellite products.
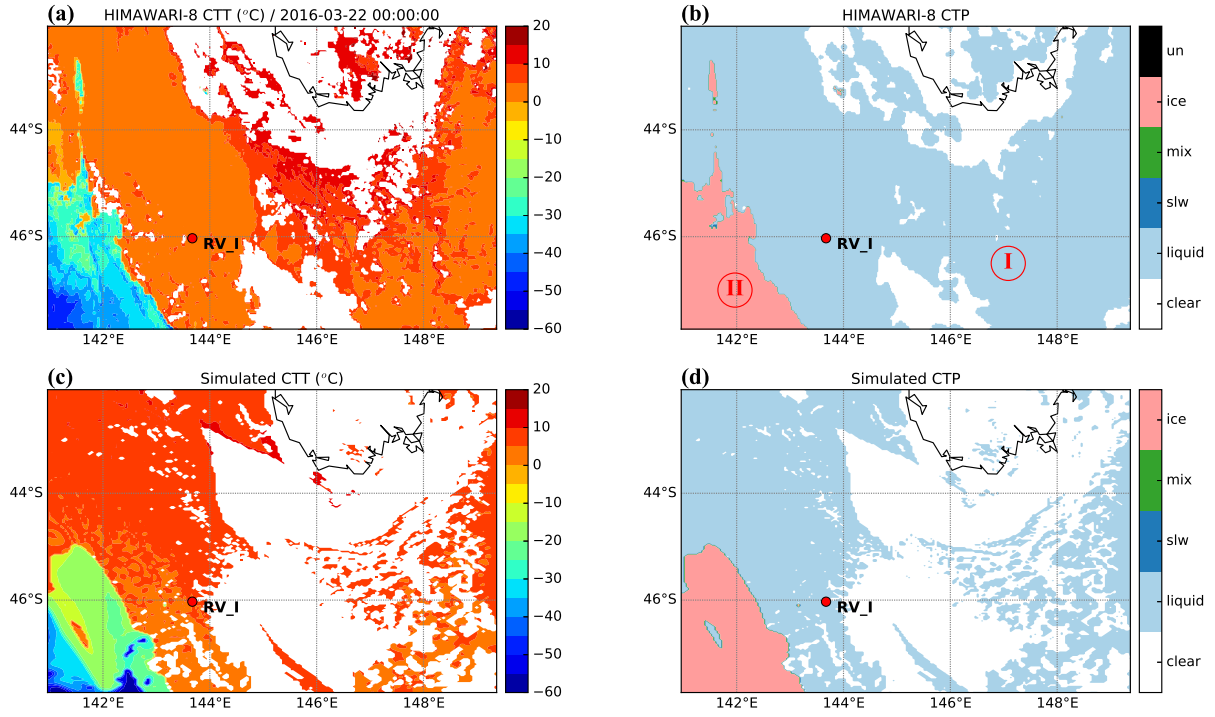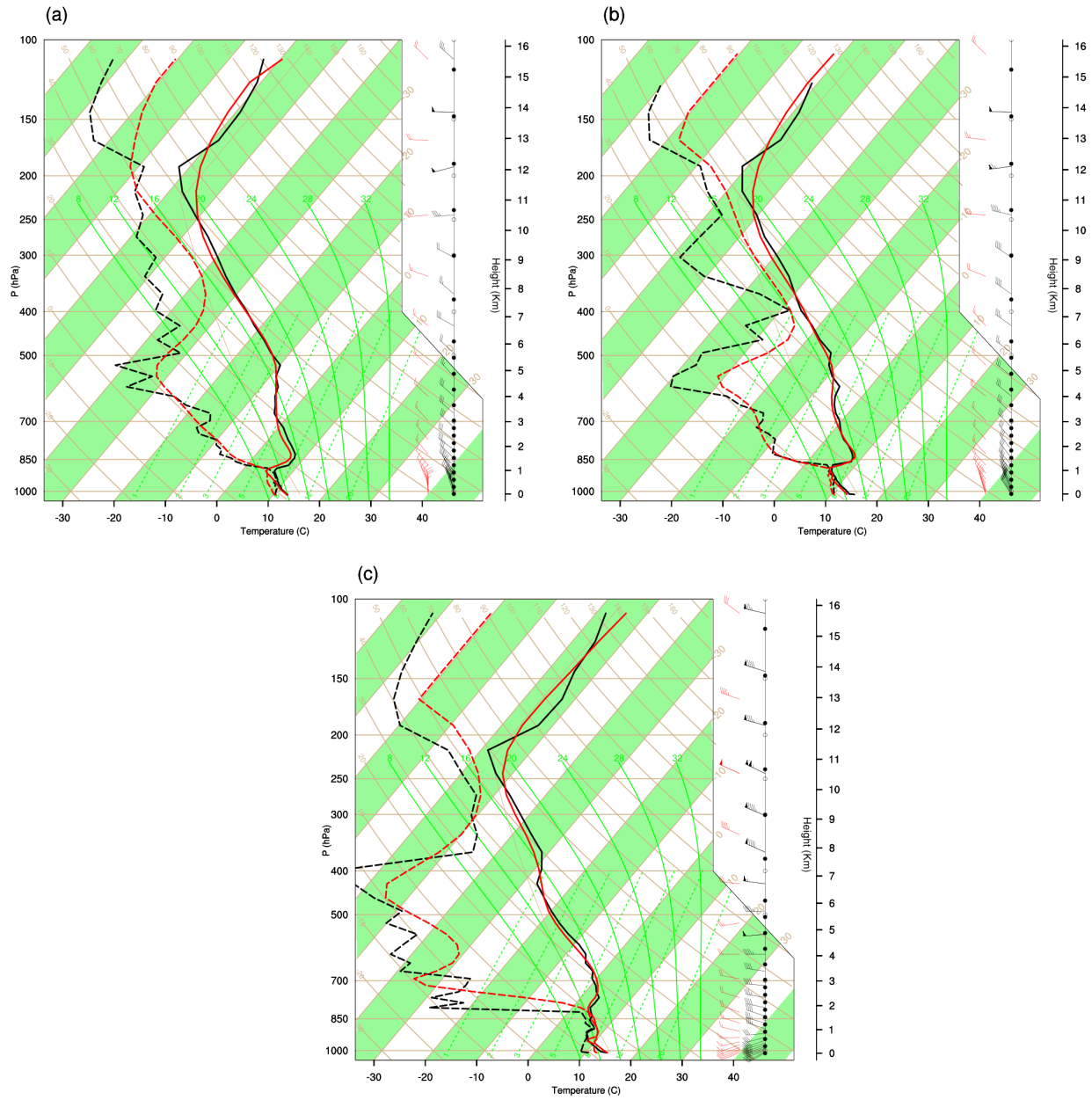
Figure 5.3: Himawari-8 observations and simulated cloud properties for case A, pre-frontal at 0000 UTC 22 March 2016. (a) Himawari-8 cloud-top temperature (CTT), (b) Himawari-8 cloud-top phase (CTP), (c) simulated CTT and (d) simulated CTP. Roman numerals in red circles indicate different regions within the domain.

5.3.1.1   Evaluation of the Base Simulation

Himawari-8 observations show the pre-frontal area roughly 24 hours before the first front has passed over the ship. The Himawari-8 CTT is shown in Fig. 5.3a, this reveals thin and warm pre-frontal clouds within the temperature range between 0° and 20°C, while much higher and colder clouds are found across the frontal band. The CTP (Fig. 5.3b) reveals extensive cloud cover in the pre-frontal zone over the ocean with the CTP being exclusively composed by liquid water (region I) and the frontal band of clouds composed by ice water (region II). These frontal glaciated clouds account for a 12% of the total cloud cover over this region (Mace et al. 2007). The corresponding simulations are displayed in Fig. 5.3c,d. Overall, the simulated CTP of glaciated and liquid water are well represent by WRF compared with Himawari-8 observations. At this time, the simulations underestimate the prevalence of the marine cloud fields by 27%, which results in widespread cloud-free areas southward Tasmania. The simulated CTT (Fig 5.3d) shows that the model produces warmer temperatures that do not match Himawari-8 CTT ranges, overestimating the CTT by ∼5°C.

Two of the upper-air soundings were launched in the pre-frontal area. Both are compared against the simulated profiles to evaluate the simulation of the thermodynamic structures. The first sounding is at the time of the Himawari-8 images of Fig. 5.3. The second was launched at 0236 UTC 22 March (Fig. 5.4). The simulated sounding generally agrees with the observations, although a lack of variability is noticed for both profiles. The simulated winds are quite well reproduced across the complete profiles through the free troposphere. Both the simulation and the observation suggest a moist layer up to ∼925 hPa, and a strong temperature inversion at ∼900 hPa. For the first sounding (Fig. 5.4a), the simulation produces high-level clouds between approximately 375 and 250 hPa, which can only be observed in the second sounding (Fig. 5.4b), simulating in advance the generation of these clouds. Further, the modeled temperature is slightly colder until 700 hPa and dewpoint temperature is drier within the MABL. For the second sounding, the profiles of temperature and dewpoint temperature are better reproduced across the MABL.

The Himawari-8 observations for the post-frontal environment is shown in Fig. 5.5 (0200 UTC 23 March). The sounding shows in Fig. 5.4c was launched at approximately the same time as this Himawari-8 image (0151 UTC 23 March). Figure 5.5 shows that the ship is under the edge of the frontal band; however, the vertical profile and surface observations show that the satellite image occurs about 3 h after the frontal passage. The CTP shows a main frontal band over Tasmania, which is dominated by glaciated clouds (region I, Fig. 5.5a). Immediately behind the second front is a band of supercooled liquid water (SLW, region III), separating fields of shallow convective warm liquid clouds (regions II and IV), within the temperature range between 5° and 15°C (Fig. 5.5b). The simulation (Fig. 5.5c,d) manages to replicate the cloud pattern seen by Himawari-8, however, the timing location of the second front is poorly represented. The simulated CTP shows that the glaciated cloud field over Tasmania is associated with the first front and the secondary band of SLW clouds (Fig. 5.5c). However, the fields of shallow convective liquid clouds are underrepresented in the simulation with a cloud fraction appreciably low (50%) compared to Himawari-8 observation (91%). The simulation also fails to adequately represent the CTT ranges (Fig. 5.5d), the low-level clouds are ∼5°C colder than the observed by

Figure 5.4: Thermodynamic profiles obtained from shipborne upper-air sounding (black lines) and simulated temperature and dewpoint profiles (red lines) at the same grid point for case A. (a) Upper-air sounding at 0003 UTC, model profile at 0000 UTC 22 March 2016, (b) upper-air sounding at 0236 UTC, model profile at 0230 UTC 22 March 2016, and (c) upper-air sounding at 0151 UTC, model profile at 0200 UTC 23 March 2016.
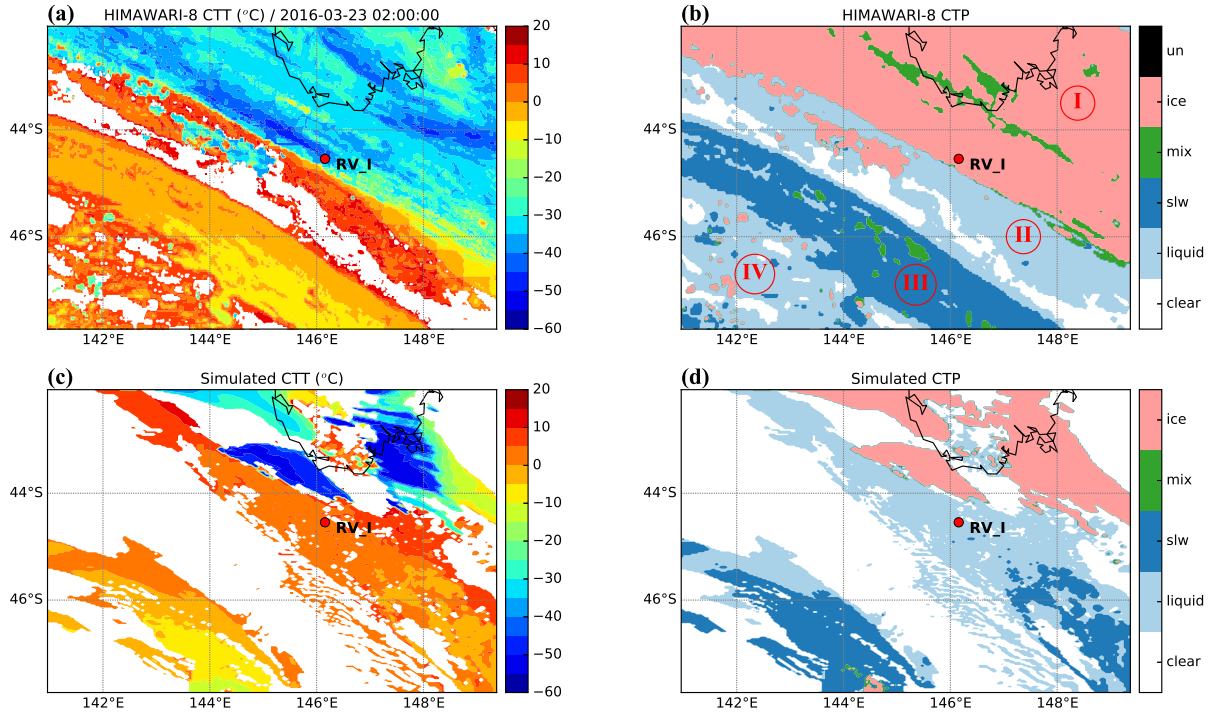
Figure 5.5: Himawari-8 observations and simulated cloud properties for case A, post-frontal at 0200 UTC 23 March 2016. (a) Himawari-8 cloud-top temperature (CTT), (b) Himawari-8 cloud-top phase (CTP), (c) simulated CTT and (d) simulated CTP. Roman numerals in red circles indicate different regions within the domain.

Himawari-8.

The vertical profile (Fig. 5.4c) shows that the model again displays a reasonable skill in simulating the post-frontal environment of the thermodynamic structure and the southwesterly winds within the MABL. However, the cloud top height is overpredicted by ~30 hPa and a temperature inversion at 900 hPa is simulated at a lower height. Further, the simulated dewpoint and temperature between the surface and 800 hPa are ~2°C higher that the observed. The sounding also indicates a decoupled structure at ~875 hPa with wind shear, which is not fully captured by the WRF simulation.

Figure 5.6 shows the profiles of observed and simulated thermodynamic variables under pre- and post-frontal conditions. As discussed above, for both pre- and post-frontal profiles, the simulation is able to reproduce the capping inversion. For instance, the simulation is able to reproduce the strong inversion in the temperature θ between 1 and 1.5 km in the pre-frontal area (Fig. 5.6a). However, the largest differences are found under post-frontal conditions for specific humidity q, where the strong shift at ~1300 m is simulated too weak and too high (Fig. 5.6b).
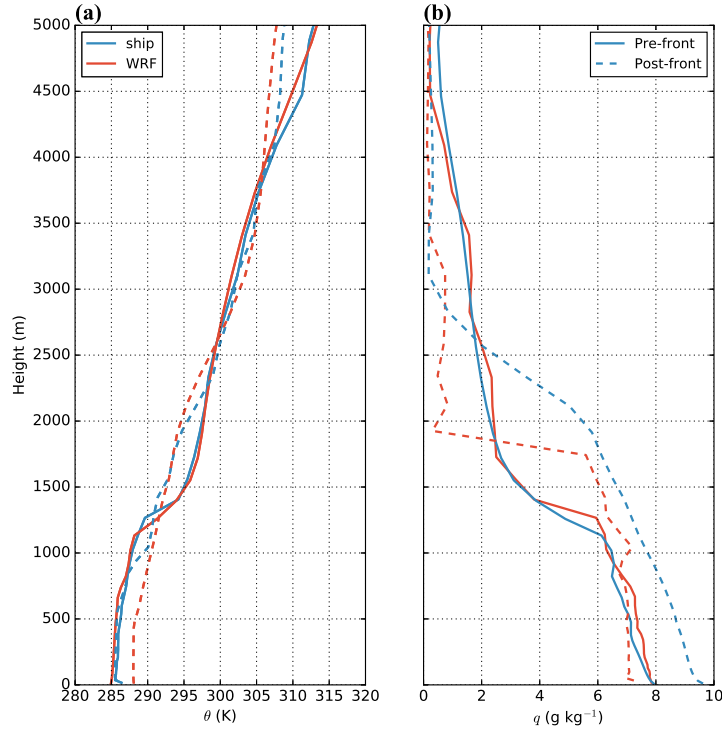
Figure 5.6: Profiles of observed (red lines) and simulated (blue lines) thermodynamic variables under pre- (solid lines) and post-frontal (dashed lines) conditions. (a) Potential temperature θ, and (b) specific humidity q.

5.3.1.2 Meteorological Time Series and Cloud Mask

Focusing on the shipborne observations, time series of wind and temperature suggest that the first cold front arrived at ~2300 UTC on 22 March and the second cold front fourteen hours later with a weaker secondary shift at approximately 0800 UTC 23 March (Fig. 5.7). The specific humidity q (Fig. 5.7d) is increasing in the pre-frontal area and during the frontal passage reaches a peak of 9.5 g kg^{-1} at ~2300 UTC 22 March, then decreases dramatically between fronts and increases again at the secondary front (7.5 g kg^{-1}).

Figure 5.8a shows the cloud mask from radar-lidar merged observations and Fig. 5.8b the cloud mask derived from the simulation. The observed frontal band is separating fields of shallow convective warm clouds. The pre-frontal shallow convection (cloud-top height below 1 km) produces light precipitation, with 1.2 mm of accumulated precipitation at 1800 UTC 22 March, while the simulated precipitation is much lower with only 0.2 mm accumulated during the same period (Fig. 5.7f). The precipitation is underrepresented in the simulations, likely because it is linked to the deficit of the low-cloud cover as shown in Fig. 5.8b. In the post-frontal conditions, on the other hand, the simulations
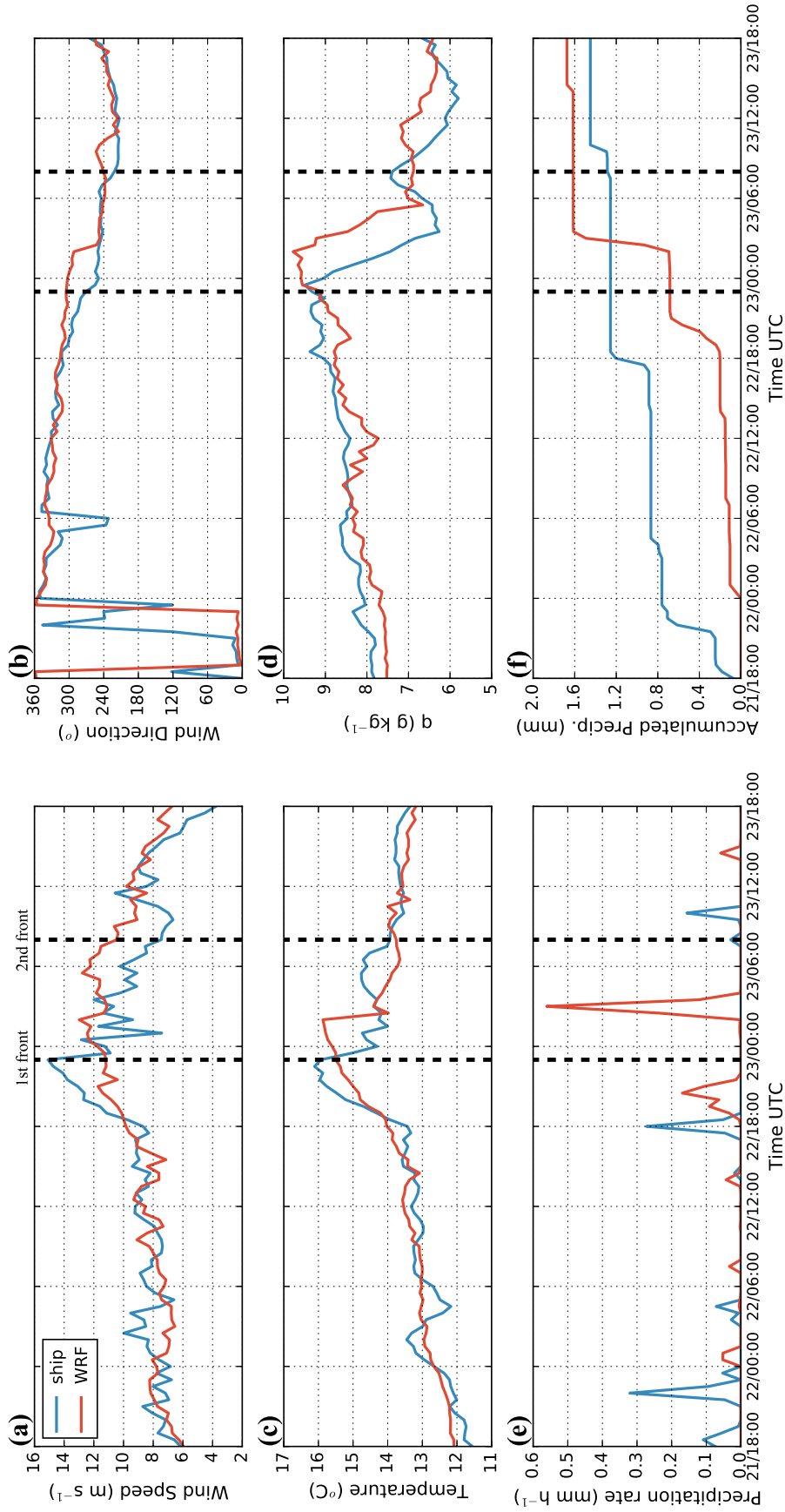
Figure 5.7: Time series of meteorological variables for case A, shipborne observations (red lines) and WRF simulation (blue lines). (a) wind speed (m s^{-1}), (b) wind direction (°), (c) air temperature (°C), (d) specific humidity q (g kg^{-1}), (e) precipitation rate (mm hr^{-1}), and (f) accumulated precipitation (mm). Dashed lines indicate the approximate time of the two fronts.
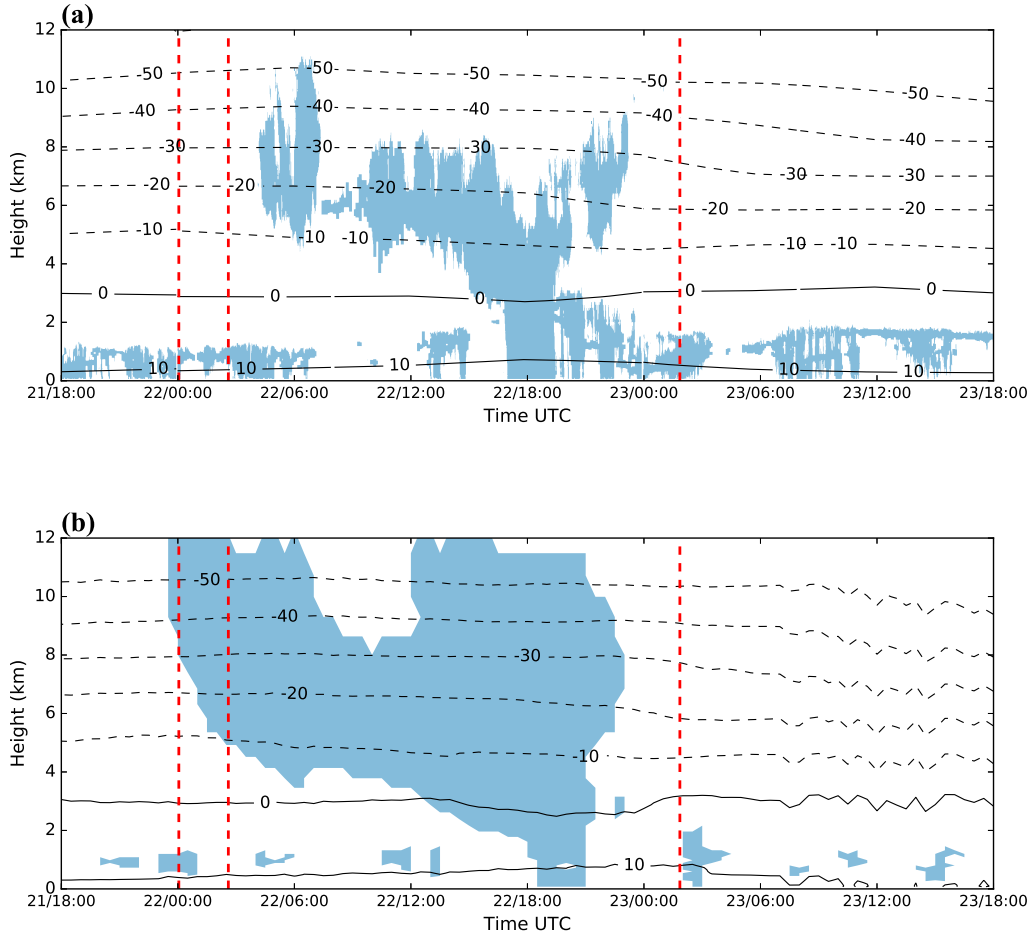
Figure 5.8: The cross sections of the cloud mask (shading) and temperature (contours) for case A. (a) Observations and (b) WRF simulation. Dashed red lines indicate the approximate launch time of the soundings in Fig. 5.4.

overestimated the precipitation, however, a deficit in the production of boundary layer clouds is also seen. Huang et al. (2014) and Wang et al. (2016) reported similar results, the WRF simulations showed a limited representation of the post-frontal low-level cloud band over the SO, in the neighborhood of Tasmania and Macquarie Island.

Overall, the simulation of the surface time series shows that the model is able to reproduce the frontal passage, although an error in the timing is observed in temperature, precipitation and q (Fig 5.7c,d,e). Wind speed and direction are consistent with the observations, but the intensity of the simulated wind speed drop at ~2300 UTC 22 March is weaker than observed. The greatest deficiency of the simulations corresponds to precipitation (Fig. 5.7e,f).
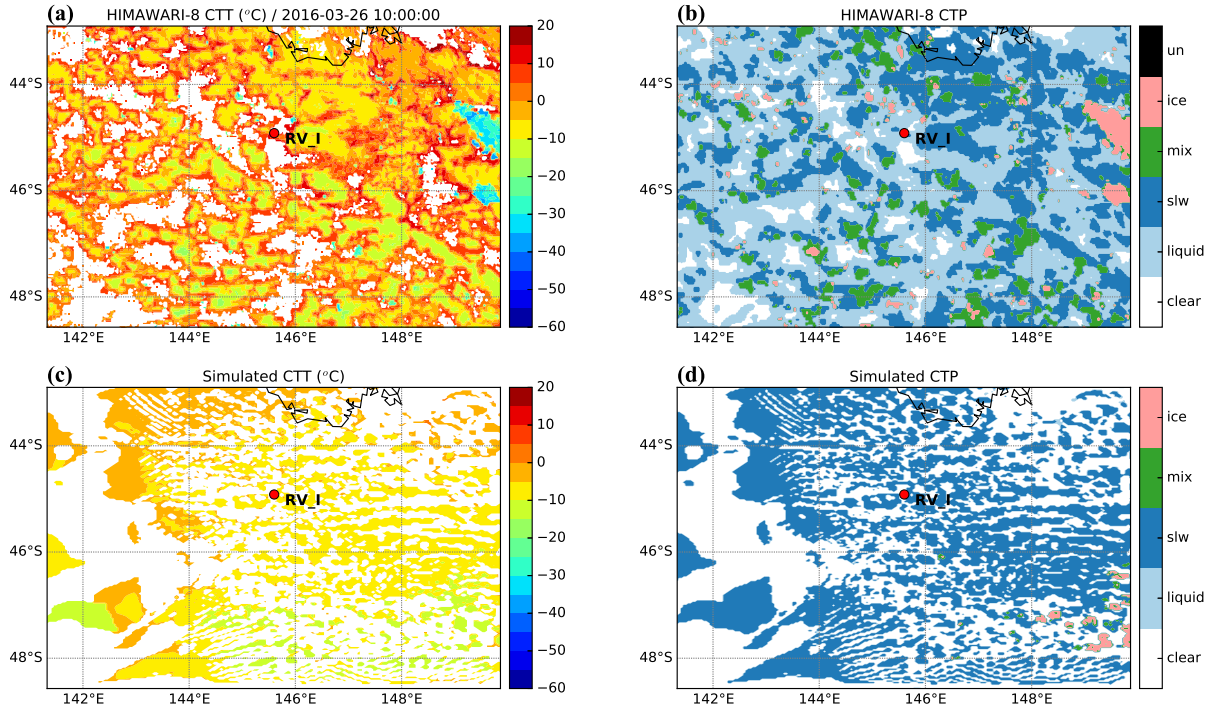
Figure 5.9: Himawari-8 observations and simulated cloud properties for case B prefrontal at 1000 UTC 26 March 2016. (a) Himawari-8 cloud-top temperature (CTT), (b) Himawari-8 cloud-top phase (CTP), (c) simulated CTT and (d) simulated CTP.

5.3.2 Case B: Open MCC and Mixed-phase Clouds Under Post-frontal Conditions

A cold front crossed Tasmania on 25 March 2016, arriving from the west roughly at 1500 UTC (Fig. 5.1d). Once the front passed the ship, a sustained period of open MCC in a post-frontal environment is maintained for approximately 48 hours.

5.3.2.1 Evaluation of the Base Simulation

The Himawari-8 images (Fig. 5.9a,b; 1000 UTC 25 March 2016) reveal an extensive field dominated by liquid, SLW and mixed-phase clouds. The CTT shows warmer temperatures above 5°C associated with liquid clouds and temperature below -5°C dominated by SLW and mixed clouds. The simulation (Fig. 5.9c,d) is not able to fully reproduce liquid or mixed clouds and has difficult to reproduce the cloud patterns. Figure 5.9d shows that the model overestimated the prevalence of SLW clouds and the CTT (Fig. 5.9c) is much less variable compared with Himawari-8 observations, on a limited range between 0° and -10°C.

Three of the upper-air soundings were launched at the beginning of the open MCC period. The launch times were at 2157, 0142 UTC on 25 March and 0624 UTC on 26 March. Figure 5.10 shows the soundings against the simulated profiles, the comparison shows that temperature and wind profiles generally agree with the observations; although, in the first and third profiles, the simulation fails to reproduce properly the height of the inversion. Further, the decoupled and multilayer structure in the MABL is not fully captured by the WRF simulation. For instance, the first sounding shows a multilayer structure between approximately 900 and 800 hPa; however the simulation does not capture these layers. The MABL evolution is observed through the soundings, where the depth of the main inversion grows from approximately 1500 m to 2300 m. For the first and the second soundings, both the simulation and the observation suggest a deep moist layer between 850 and 830 hPa (Fig. 5.10a,b), which increases up to ∼815 hPa in the third sounding (Fig. 5.10c). However, the simulations overestimated the dewpoint within the MABL for all the soundings, specially in the first one, where the dewpoint is overestimated by ∼3°C and the moist layer height is ∼50 hPa higher compared with the observed.

5.3.2.2   Meteorological Time Series and Cloud Mask

The time series of the shipborne observations for case B are shown in Fig. 5.11. Winds and temperature shows that the cold front passed the ship at approximately 1700 UTC on 25 March and the precipitation rate associated to the front has a peak of 2.4 mm hr^{-1} (Fig. 5.11e). Once the ship is in a post-frontal environment, temperature, wind speed and q decrease quickly between 1800 UTC 25 March and 1200 UTC 26 March, until a second period of high precipitation rate is reached.

The simulations shows skills in reproducing the surface winds (Fig. 5.11a,b), the model simulated the shift of winds from northwest to southwest at ∼1800 UTC 25 March and to west at ∼1800 UTC 26 March; however, the model is not able to reproduces the sudden decreases of wind speed at 0900 UTC and 1500 UTC on 26 March. Both the temperature and q from the simulation and observations match reasonably well (Fig. 5.11c,d); although, in the case of temperature, the model has difficulty reproducing the variability of the observations between 0000 UTC 26 March and 0000 UTC on 27 March.
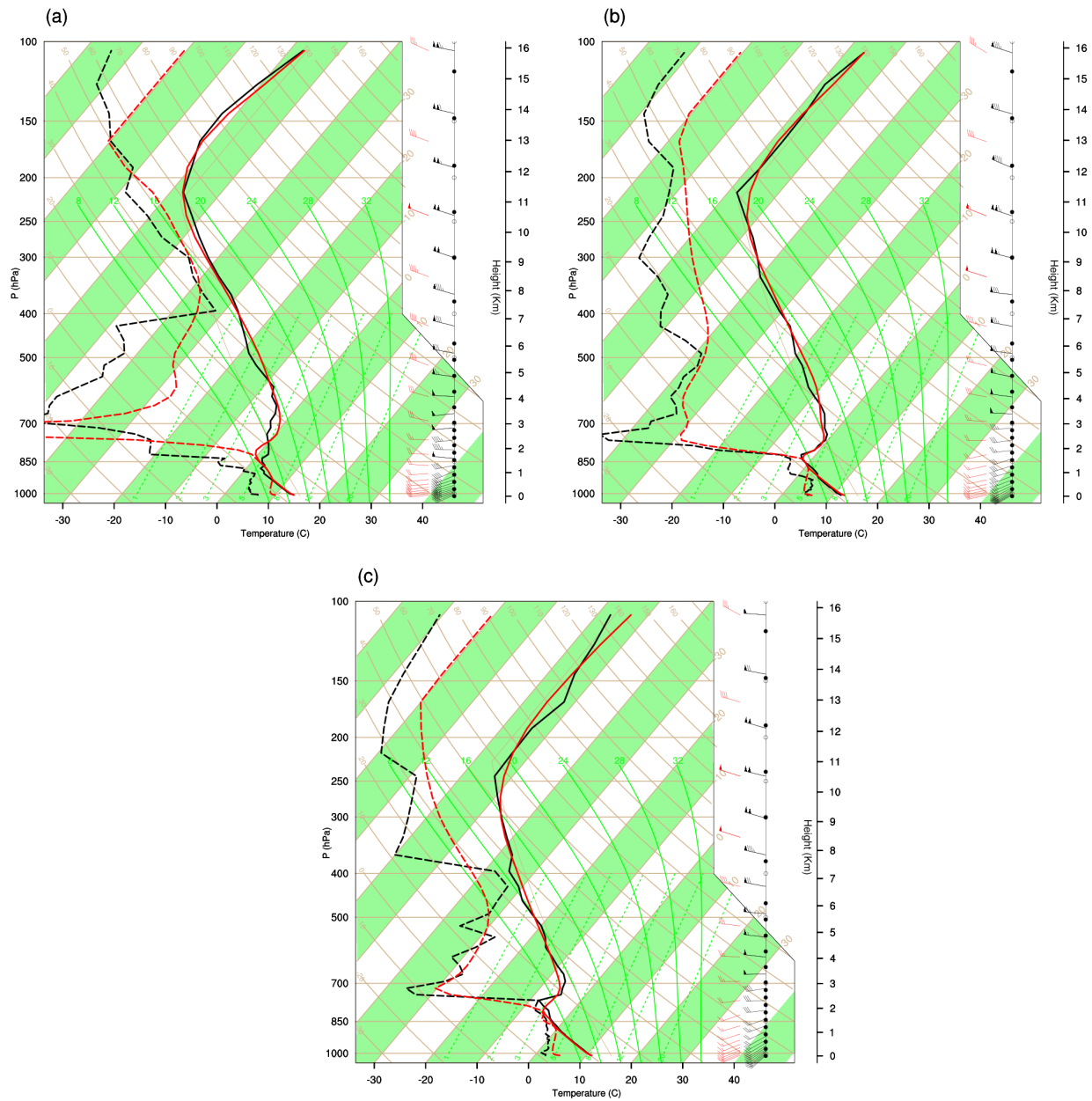
Figure 5.10: Thermodynamic profiles obtained from shipborne upper-air sounding (black lines) and simulated temperature and dewpoint profiles (red lines) at the same grid point for case B. (a) Upper-air sounding at 2157 UTC, model profile at 2200 UTC 25 March 2016, (b) upper-air sounding at 0142 UTC, model profile at 0130 UTC 26 March 2016, and (c) upper-air sounding at 0624 UTC, model profile at 0630 UTC 26 March 2016.

107
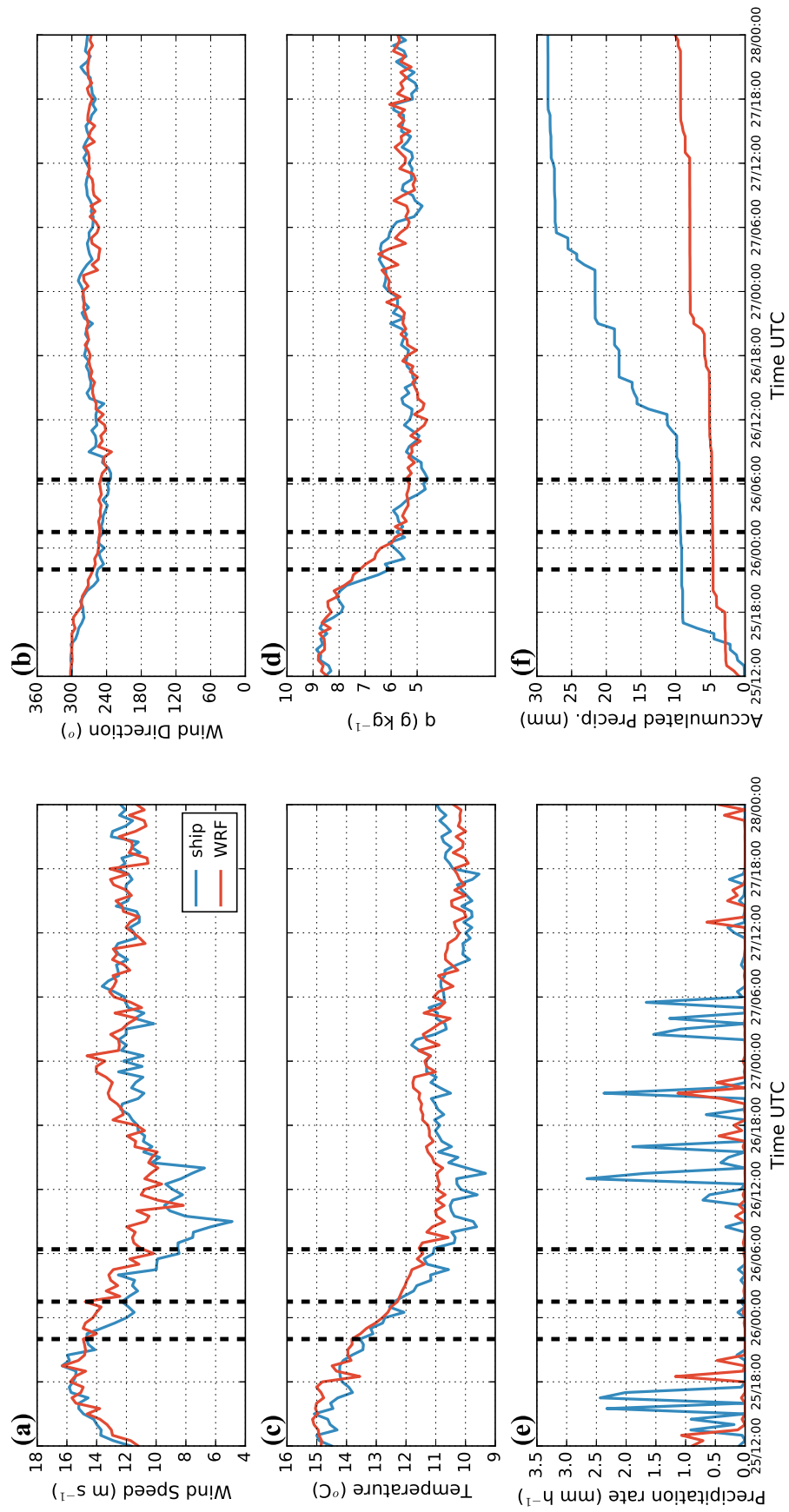
**Figure 5.11:** As Fig. 5.7, but for case B. Dashed lines indicate the approximate launch time of the soundings in Fig. 5.10.

Different from the case A, the observed cloud field resides primarily below 2.5 km and in the sub-freezing temperature range (0 to -10°C, Fig. 5.12a), where SLW and mixed phase cloud tops were suggested by both the shipborne radar-lidar and the Himawari-8 products. A multilayer structure is appreciable between 1 and 2.5 km, where at least two layers are observed and separated by the freezing level, consistent with what is suggested by the soundings. Figure 5.12b shows the cloud mask derived from the simulation, the post-frontal shallow clouds of open MCC are simulated reasonably well and within a similar range of temperature than observations. However, the simulation underestimates the mixed phase between 0 to -10°C, producing more SLW clouds. The simulation also is not able to capture the multilayer clouds observed. Given the coarse horizontal resolution of the WRF simulations (finest resolution domain of 1 km) compared with radar-lidar products (25 m), it is unsurprising that differences exist, as shown in Fig. 5.8b, large groups of clouds are simulated, unlike what the observations show.

The highest differences of time series are found in the precipitation. Observations show relatively heavy precipitation (> 1.5 mm hr^{-1}) during the period of open MCC and an accumulation of 18 mm over 24 hours. However, the simulations fails in reproducing this amount, underestimating by $\sim 70\%$ the total accumulated over the period simulated. The precipitation rate shows (Fig. 5.11e) that the model has errors in the timing and intensity of the precipitation, which rarely exceeds 1 mm hr^{-1}. The evaluation of the thermodynamic profiles using the sounding suggests that the model does not simulate the collapse of the MABL depth prior to the onset of precipitation (Fig. 5.10a,c), where the dewpoint break down at ~ 900 hPa.

5.3.2.3 Cloud-top Phase Properties

Histograms of the relative frequencies of the CTP decomposed as a function of temperature are calculated for both Himawari-8 observations and WRF simulations (Fig. 5.13a,b). These histograms are made across the full duration of the simulation after the 12-h spin up. The Himawari-8 histogram shows primarily clouds at temperatures above -10°C (Fig. 5.13a). The peak at warm temperatures (from 0° to 10°C) highlights the prevalence of boundary layer cloud, which are primarily liquid and decoupled from the layers above.
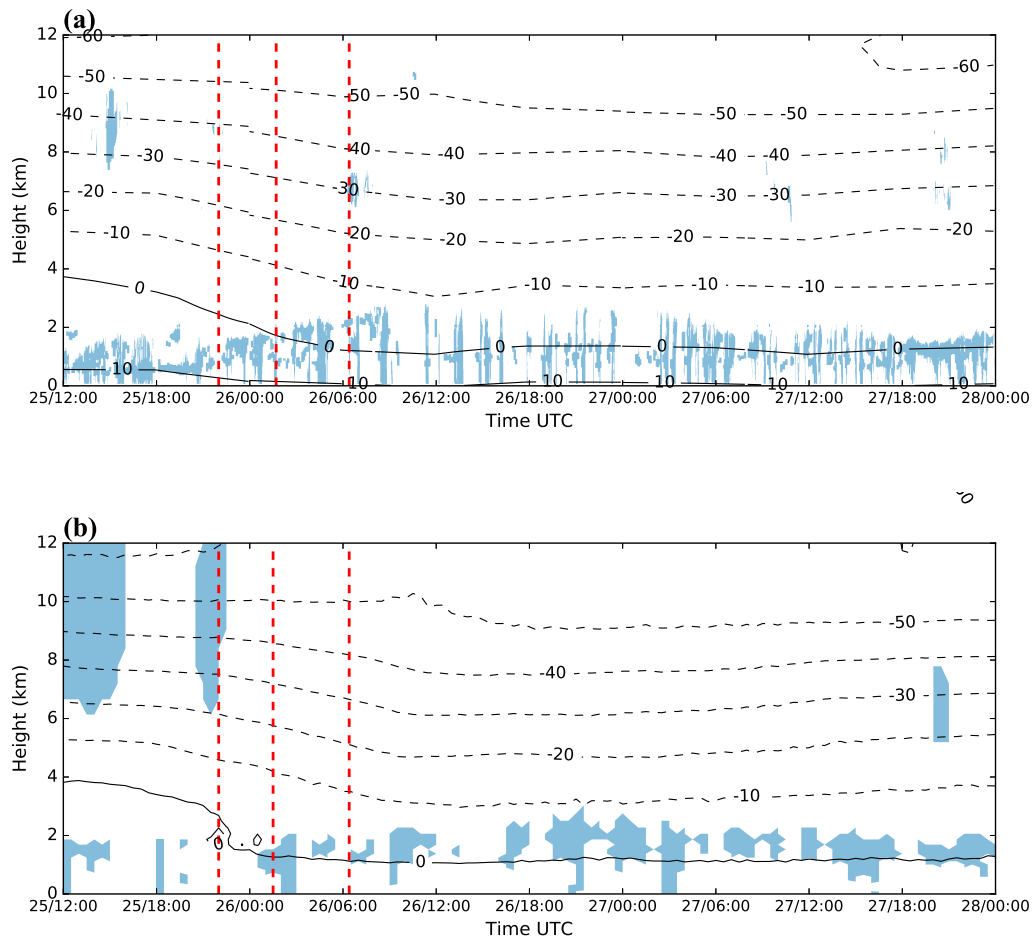
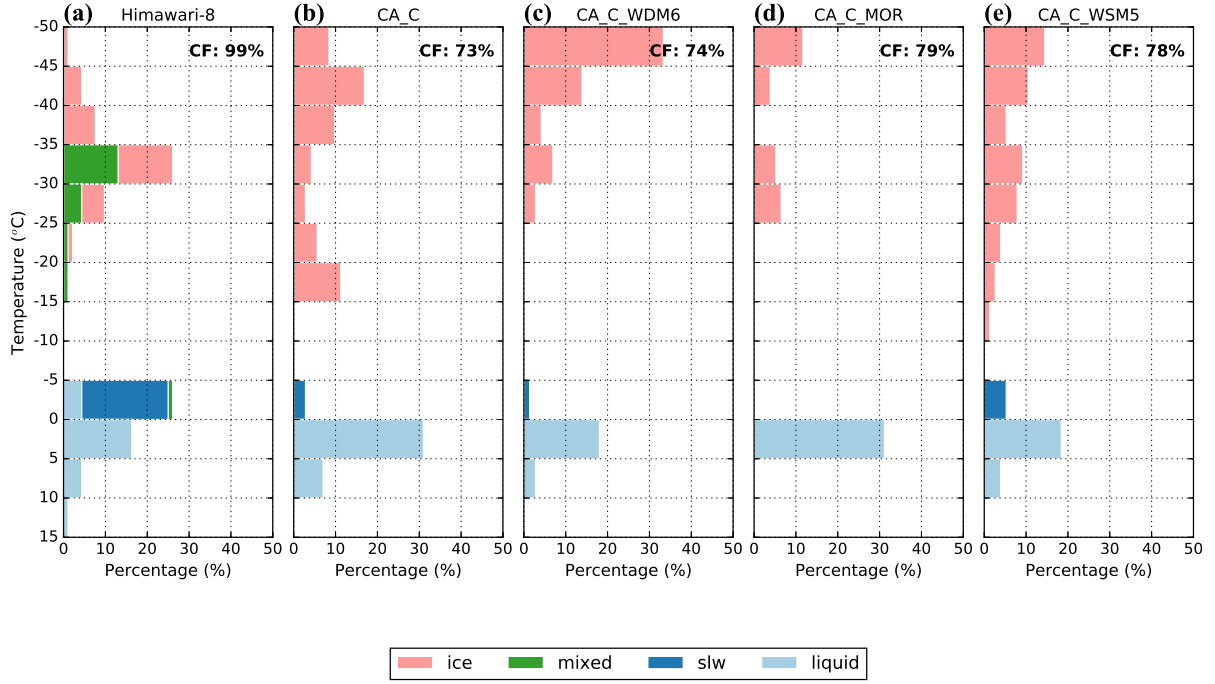**Figure 5.12:** As Fig. 5.8, but for case B.
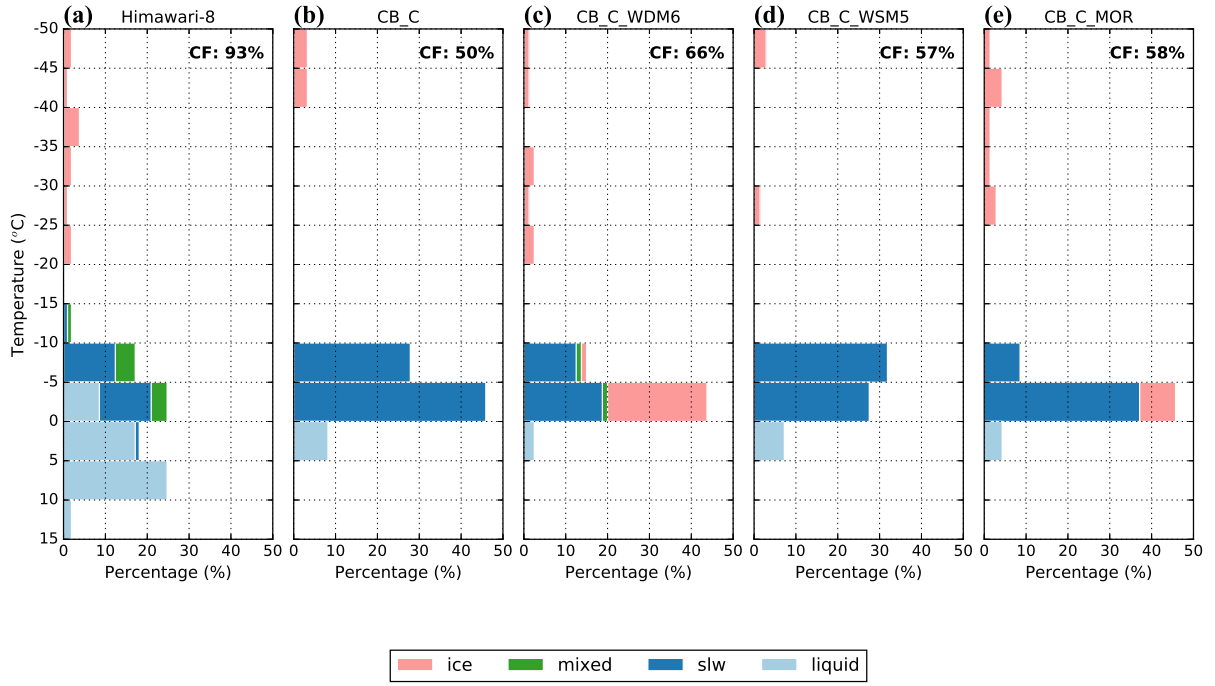
Figure 5.13: Histograms of relative frequencies of CTP (ice, mixed phase, supercooled and liquid water) descomposed into 5°C temperature bins for the complete period of case B. The cloud fraction (CF) is displayed in each panel. (a) Himawari-8 products, and (b-e) WRF simulations (Base, WDM6, Morrison and WSM5 schemes). The class of uncertain is not considered in the simulated CTP.

The observed cloud tops are dominated by liquid along the whole range of temperatures, where the cumulative frequency of warm clouds is approximately 54%. In temperature ranges between 0° and -10°C, the relative frequencies of liquid clouds decrease with the increased of SLW and mixed phase clouds. Overall, the temperature ranges between 10°C and -10°C reveal a decoupled and multilayer structure in the MABL, as shown by the soundings and the cloud mask. Low relative frequencies of ice clouds are found below -20°C (11% of the total cloud cover), which are mainly associated with the frontal passages at the beginning of the period modeled.

The simulated histograms for cloud top are defined at 0.1 cloud optical thickness (Fig 5.13b). The simulated cloud fraction (CF) remains appreciably low (50%), compared to Himawari-8 observation (93%). The simulated distribution shows the highest cumulative frequency at temperatures between 0° and -10°C is for SLW clouds (74%). Considering the CTT as an altitude proxy, the low-level clouds are reproduced, but they are at colder temperatures than observations. Above 0°C (warm clouds) the relative frequency of the liquid class is largely underestimated compared with the observations (8% of the total

Figure 5.14: As Fig. 5.13, but for case A.

cloud cover), which is, in part, compensated by the larger frequencies of SLW clouds between 0° and -10°C. These differences in captured low-level clouds and a low CF of simulations might be linked to the deficit of precipitation.

5.4 Sensitivity Study

5.4.1 Case A

5.4.1.1 Cloud-top Phase Properties

The relative frequencies of the CTP, decomposed as a function of temperature, are calculated with different MP schemes. Figure 5.14 presents the results for case A of all MP schemes analyzed, including Himawari-8 and the base simulation. The observed cloud histogram for case A shows a bimodal distribution with the second peak occurring between -30° and -35°C. The observed low-level clouds are dominated by liquid and SLW between 15 and -5°C. The simulation fails in reproduce the relative frequencies of SLW, which are largely underestimated and compensated by the increased low-level warm cloud tops. The CF observed by Himawari-8 is 99%; however, all the schemes simulated a cloud fraction significantly lower.

Among the double-moment schemes, Morrison exhibits the largest differences with the observations (Fig. 5.14d), having a high relative frequency of liquid clouds between 0° and 5°C (31%) and no clouds tops at temperature above 5°C; further, no mixed and SLW clouds are simulated. Conversely, the WSM5 single-moment scheme presents better results (Fig. 5.14e), the SLW relative frequency is higher compared with double-moment schemes and there are some notable similarities to that observed in terms of the shape of the distribution, although mixed-phase clouds are not simulated.

5.4.1.2 Vertical Profiles

Focusing on the PBL schemes and changes pre- and post-frontal passage, Fig. 5.15 shows the profiles of θ, q and relative humidity for observations, CA_C, CA_MYJ_C and CA_ACM2_C. Under post-frontal conditions (Fig. 5.15d,e,f), the three schemes have similar overall values and similar vertical structure, while the differences with the observations are maintained and the decoupling at 1000 m is not produced by any scheme (Fig. 5.15d). In the pre-frontal environment (Fig. 5.15a,b,c), q and relative humidity profiles show that the MABL height simulated by the MYJ scheme is lower compared to the YSU and ACM2 schemes and observations, and θ profile from the MYJ scheme is colder than observations. Overall, local closure schemes, such as MYJ, are found to produce insufficient mixing in the convective boundary layer (Brown 1996). Essentially, the MYJ and ACM2 schemes are not able to substantially improve the simulation of case A.

5.4.1.3 Precipitation

Figure 5.16 shows the time series for precipitation rate and accumulated over the period modeled. Both the MP and PBL schemes exhibit similar characteristics in the precipitation rate (Fig 5.16a), the pre-frontal shallow convection precipitation is underestimated for all the schemes likely due to the deficit of the low-cloud cover within this sector, and the frontal passage precipitation together with the post-frontal precipitation are overestimated in different magnitudes. Accumulated precipitation (Fig. 5.16b) shows that Morrison and the WSM5 schemes largely overestimated the amount of precipitation (over three times the observed). In the case of the WDM6 scheme, the simulation sightly overestimated the accumulated precipitation, with a peak of heavy precipitation (2.8 mm
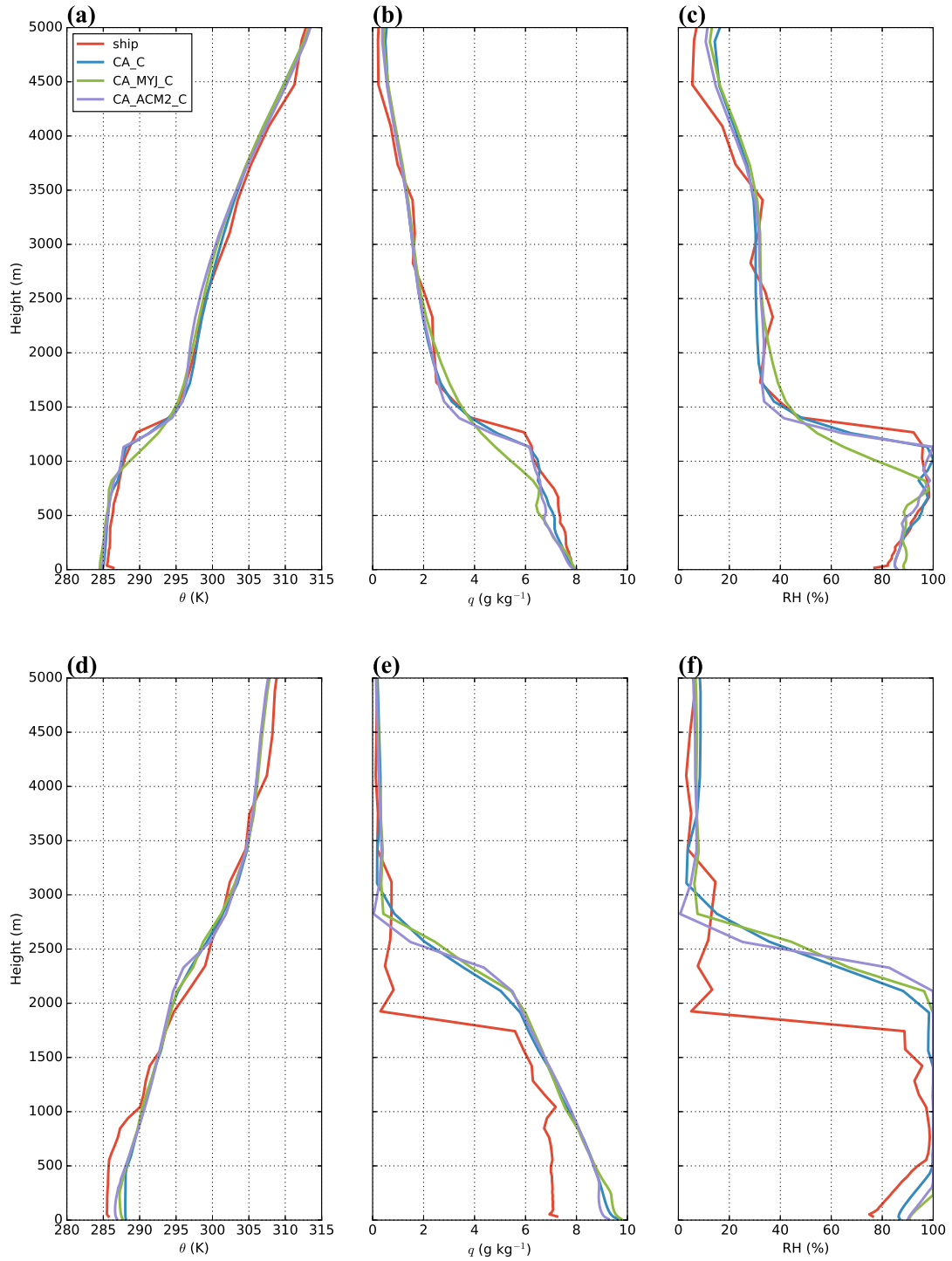
Figure 5.15: Profiles of observed and simulated thermodynamic variables under pre- and post-frontal conditions for the PBL schemes simulated. (a,d) Potential temperature θ, (b,e) specific humidity q, and (c,d) relative humidity.
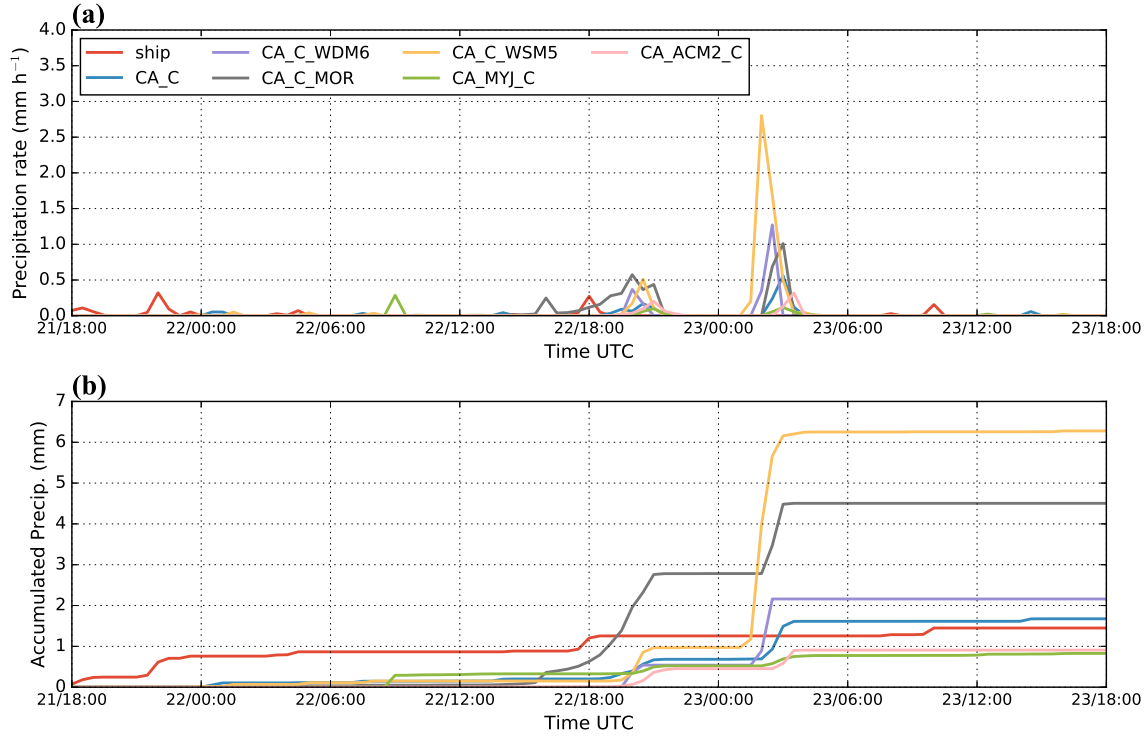
Figure 5.16: Time series of precipitation for shipborne observations and WRF simulations for sensitivity test. (a) precipitation rate (mm hr^{-1}), (b) accumulated precipitation (mm) for case A.

hr^{-1}) at $\sim$0230 UTC 23 March. The PBL scheme test shows that the precipitation rates in the MYJ and ACM2 schemes are light over the complete period with the accumulated precipitation half of the observed (0.9 mm).

5.4.2   Case B

5.4.2.1   Cloud-top Phase Properties

For case B, the relative frequencies of the CTP, decomposed as a function of temperature for all MP schemes, are shown in Fig. 5.13. Comparing simulations CB_WDM6_C and CB_WSM5_C to CB_C, a peak of ice clouds is found between 0° and 5°C in both simulations (19% and 9% respectively). These differences could be due to how each scheme considers snow, the Thompson scheme considers snow as primarily composed by fractal-like aggregated crystals (Thompson et al. 2008), which is conceptually more realistic compared with the approach of the WSM5 and WDM6 schemes with spherical constant snow crystals (Galligani et al. 2017). None of the MP schemes predict warm clouds above 5°C and in the range of 0° and 5°C the relative frequency of liquid clouds is

underestimated.

5.4.2.2 Vertical Profiles

The evaluation of the thermodynamic profiles using soundings suggests that the different PBL schemes do not simulate the growth of the MABL depth prior to the onset of precipitation below the open MCC (Fig. 5.17). The soundings at 2157 UTC March 25 and 0142 UTC March 26 show a decoupled and multilayer structure, which decreased between soundings from ~1,200 to 700 m (Fig. 5.17a). The YSU and ACM2 schemes both lead to predictions of a well-mixed boundary layer and higher moisture. Conversely, the MYJ scheme tried to produce the decoupling; however, the simulation is not able to reproduce the magnitude as observed, with a higher amount of moisture and lower precipitation.

5.4.2.3 Precipitation

Different from case A, the behaviour between different MP schemes is very dissimilar. The WDM6 and WSM5 schemes are delayed in the generation of precipitation with respect to the other schemes and observations (Fig. 5.18a). The WDM6 scheme accumulated approximately only 5 mm over 60 hours of simulation, half of the other schemes, such as Thompson and WSM5 (Fig. 5.18b). Compared with the observations, all the schemes shows a large deficit in the production of precipitation during the period of open MCC in the post-frontal environment. Testing a different PBL scheme, such as MYJ and ACM2, does not show an improvement in the simulation of case B, and such as some of the MP schemes, the generation of precipitation is delayed.

In summary, both the MP and PBL schemes show that the representation of marine stratocumulus clouds within the MABL is largely underestimated and remains as a challenge for the simulations. As a direct consequence of the lack of simulated low-level clouds, the simulated precipitation presents large inconsistencies with observation and a high variability. Although, the simulations are able to reproduce other variables such as temperature, specific humidity and winds. The simulated CTP reveals that while liquid and SLW clouds are represented, their frequencies are lower compared to the observed
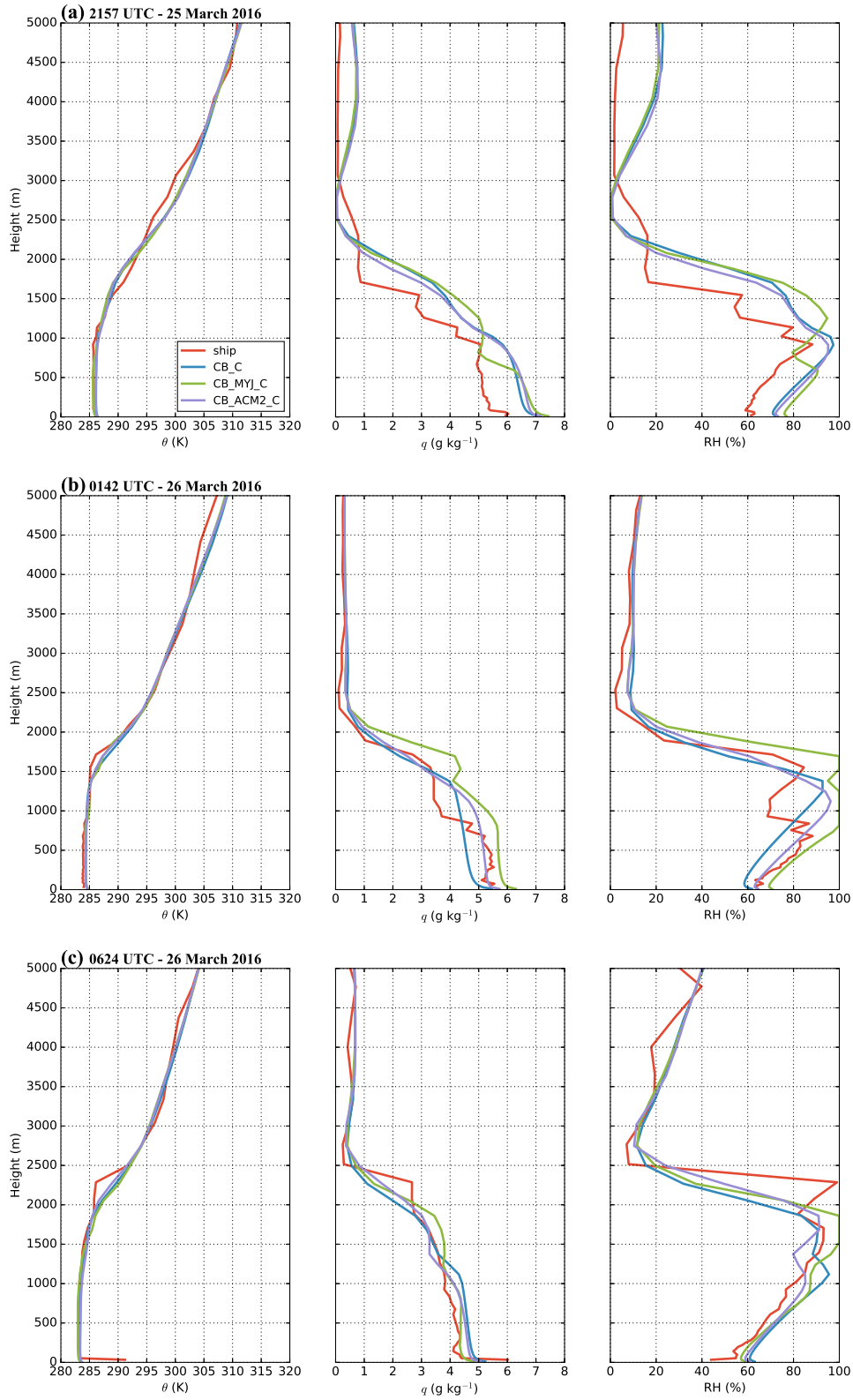
Figure 5.17: Profiles of observed and simulated potential temperature (θ), specific humidity (q) and relative humidity for different PBL schemes (case B). (a) 2157 UTC March 25, (b) 0142 UTC March 26 and (c) 0624 UTC March 26
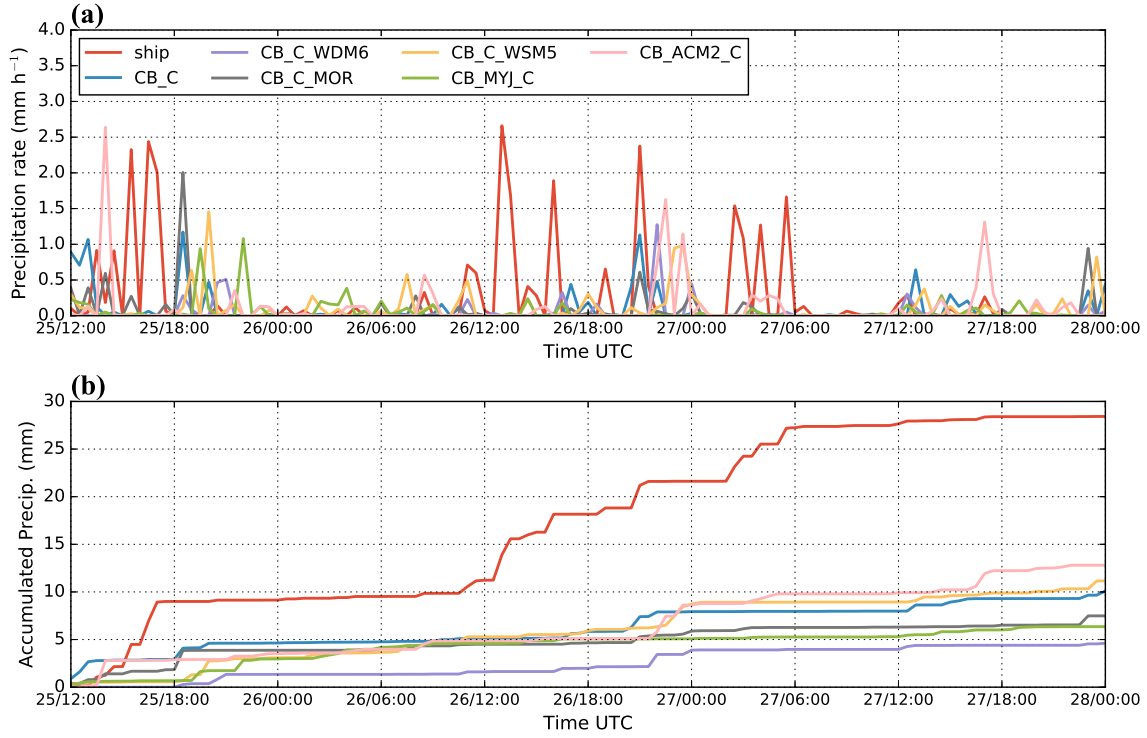
Figure 5.18: As Fig. 5.16, but for case B.

by Himawari-8. Both cases show that the simulations fail to produce the amount of mixed-phase clouds.

5.5 Discussion and Conclusions

Shipborne observations from 2016 CAPRICORN project and Himawari-8 products have been used to evaluate the WRF Model V3.9.1 in simulating marine stratocumulus clouds and MABL structure over the SO. Two cases during CAPRICORN field campaign were chosen. In case A (21-23 March 2016), a rapid succession of two fronts was encountered, separating fields of shallow convective warm clouds. The second case (case B, 25-27 March 2016) focusses on a sustained period of open mesoscale cellular convection in a post-frontal environment. An intercomparison of different PBL and MP schemes in the WRF model for marine cloudy boundary layers is presented to test the sensitivity of the simulations.

For both case studies, the simulations demonstrate a level of skill in representing surface meteorological variables such as temperature, humidity and winds. In the case of winds, Huang et al. (2014) and Morrison et al. (2010) reported that WRF simulations over Tasmania fail to develop wind shear near the surface. Upper-air soundings from

our cases do not display strong wind shear near the surface. Despite the relatively good representation of these surface meteorological variables, WRF simulations have difficulties in producing pre- and post-frontal low-level cloud fields, mixed-phase cloud tops, and surface precipitation. Previous works simulating the boundary layer clouds over the SO (e.g., Huang et al. 2014; Wang et al. 2016) highlight that WRF simulations have limited skill in generating boundary layer clouds, as observed by satellite products.

Both cases show high frequencies of observed low-level clouds in the range of temperatures between -10° and 10°C, yet simulations have difficulties producing these clouds. Regarding case A, the simulation with the Thompson scheme fails to reproduce SLW and frozen hydrometeors (mixed phase) between 0° and -5°C. The Thompson scheme uses the Cooper parameterization to initiate ice (Cooper 1986), which does not begin to move mass from the liquid to ice class until temperatures are below -8°C, or the supersaturation w.r.t. ice is greater than 8%. For case B, this seems to be a factor in the large quantities of SLW simulated clouds and the lack of mixed-phase clouds; essentially, the model parameterization can not transfer mass from the liquid to the frozen temperatures until ice is initiated at temperatures less than -8°C.

Himawari-8 images show high values of cloud fraction in both cases (Fig. 5.13 and 5.14); however, the frequency of cloud coverage varies widely among different MP schemes. In case A, the cloud fraction simulated by Thompson scheme is only 73% and underestimates the amount of stratocumulus while overestimating the cumulus clouds (glaciated clouds). For case B, cloud fraction is much lower than observed, with a minimum of 50% cloud cover simulated by Thompson scheme (Fig. 5.13b). In both cases, a deficit of the low-cloud cover is directly linked to an underproduction of precipitation.

Sensitivity experiments with different physical parameterization PBL schemes were performed to investigate the impact of the MABL thermodynamic structure on the simulations of the shallow convective clouds. The profiles of simulated thermodynamic variables for case A shows that the YSU and ACM2 schemes both lead to a better simulation of the moisture profiles in the pre-frontal environment. Conversely, the MYJ scheme provides shallower and drier profiles that YSU and ACM2 schemes within the boundary layer. This could be result of either strong entrainment, drying the boundary layer or weak

surface fluxes. Above the boundary layer, the MYJ scheme moisture is higher that other schemes and observations, this is consistent with simulations of non-local scheme, where more moisture is transport away from the surface and deposits at a higher level (e.g., Hu et al. 2010; Srinivas et al. 2007). In the post-frontal environment, the three schemes overpredicted the height of the capping inversion at heights between 2 and 2.5 km, which is much higher than the observed height at ∼1,700 m. This could be consequence of a stronger capping inversion, which inhibits turbulent mixing or entrainment of the warmer and drier overlying air into the boundary layer. This keeps the boundary layer moister compared with the observations. Similar to Huang et al. (2014), a higher inversion, without further mixing, should produce a deeper cloud, yet these post-frontal clouds were not simulated. Regarding case B, the decoupling observed indicates that the MABL is not well mixed, which is linked to a lack of turbulence mixing. None of the PBL schemes is able to fully produce the decoupling, and the three schemes predict higher moisture within the MABL, with a well-mixed boundary layer for YSU and ACM2 schemes. The higher amount of moisture simulated for the three schemes is likely because the shallow post-frontal clouds are not precipitating as show the precipitation deficit in Fig. 5.11f.

In both cases, during the post-frontal conditions the simulated thermodynamic profiles of moisture are higher compared to the observations and for both cases the shallow convective clouds were underestimated. Huang et al. (2014) suggested that the simplest explanation for the absence of simulated boundary layer clouds is a lack of moisture within the boundary layer, which might be due to either weak surface fluxes or a strong entrainment, which helps warm and dry the boundary layer. Nonetheless, they were not able to be evaluated the simulations against in situ observations. These biases are important over the SO, where precipitation processes are still poorly understood (Huang et al. 2017) and open MCC are typically observed in the cold sectors of frequent mid-latitude cyclones (Field and Wood 2007).

The recent dedicated field campaign CAPRICORN 20016 has contributed with comprehensive observations over the SO. These in situ observations have provided relevant information of the MABL structure, complementing satellites and Macquarie Island observations, and improving the evaluation of the WRF model in this region. Our findings

suggest that WRF simulations have significant difficulties in producing both the low-level cloud field and surface precipitation. These difficulties are due to a combination of factors resulting from the limitations of the PBL scheme in reproduces the boundary layer structure (e.g., no evidence of decoupling or wind shear); and the MP scheme in producing mixed phase conditions and moments of glaciation. Further research is needed to analyze the role of surface fluxes in the evolution of the MABL and the parameterization of low-level clouds and precipitation.

Chapter 6

Summary

This thesis has been principally concerned with the study of the atmospheric boundary layer at different scales of motions, with an emphasis on the largest contributions to the total turbulence kinetic energy. This chapter summarizes the major conclusions and findings that have been drawn on the research presented in Chapter 2, 3, 4 and 5.

6.1   The Summary of Important Results

6.1.1   Observations of Wind-direction Variability in the Nocturnal Boundary Layer

The main characteristics of large sudden wind-direction shifts and submeso variability under nocturnal conditions are examined using a micrometeorological network of stations in north-western Victoria, Australia. The network was located in an area with mostly homogeneous and flat terrain. The research reveal that:

- The submeso motions at the study site exhibit behaviour typical of flat terrain, such as the lower relative mesovelocity scale and smaller cross-wind variances than that for complex terrain.

- The distribution of wind-direction shifts shows that there is a small but persistent preference for counter-clockwise rotation, occurring for 55% of the time.

- Large wind-direction shifts tend to be associated with a sharp decrease in air temper-

ature (74% of the time), which is associated with rising motion of cold air, followed by an increase in turbulent mixing.

- The horizontal propagation of events was analyzed using the cross-correlation function method. There is no preferred mean wind direction associated with the events nor is there any relationship between the mean wind and propagation directions.

- The lack of relationship between the mean wind vector and propagation vector indicates that the events are not local flow perturbations advected by the mean flow but are rather features of generally unknown origin.

6.1.2 Characteristics of the Marine Atmospheric Boundary Layer over the Southern Ocean in Response to the Synoptic Forcing

The characteristics of the marine atmospheric boundary layer (MABL) in relation to synoptic meteorology over the Southern Ocean (SO) are examine using upper-air soundings and surface precipitation at Macquarie Island (54.62°S, 158.85°E), with a primary focus on the post-cold-frontal environment where large cloud and radiative biases are presented in a multitude of climate models. Thermodynamic profiles from the ECMWF ERA-Interim reanalyses are compared with the observations to evaluate their representation of the MABL characteristics. Results show that:

- Observations confirm that boundary layer clouds over the SO commonly reside within a shallow MABL under the influence of frequent mid-latitude cyclones and fronts.

- The evaluation of MABL height shows that, for both observations and reanalysis, the MABL is higher northward of the low center and under post-cold front conditions. Under cold frontal passages, however, the main inversions are not well represented by ERA-Interim, which is featured by an underestimating of the MABL height by 22%.

- Significant differences are found in the moisture profiles within the MABL between the observations and ERA-Interim soundings within the context of cold frontal passages. The moisture in the ERA-Interim is found to be too confined to the surface layer, which is consistent with the shallower MABL represented by the ERA-Interim.

- Analysis of the surface precipitation shows that ERA-Interim overestimates the amount of precipitation over Macquarie Island in the vicinity of cyclone cores but underestimates the precipitation not immediately associated with cold fronts. An overall underestimate of the annual precipitation by 11% was observed.

6.1.3 Diurnal Cycle of Precipitation and the Marine Atmospheric Boundary Layer over Macquarie Island

Surface hourly Macquarie Island precipitation records have been used to examined the diurnal cycle and their relationship with the MABL over Macquarie Island. The analysis is broken into seasons to further reveal its nature. Surface precipitation and thermodynamic profiles from the ECMWF ERA-Interim reanalyses are compared with observations to evaluate their representation of the diurnal cycle. Results of the analysis show that:

- The annual diurnal cycle of precipitation exhibit a marked variation throughout the day, the mean precipitation increases after sunset and during night reaching a maximum before sunrise, shortly before dawn at 0500 LST and then decreases until approximately 1400 LST.

- The greatest variation of the diurnal precipitation cycle occurs during the austral summer, with a magnitude ~ 0.04 mm hr^{-1}.

- Heavy precipitation does not show a systematical variation through the day over Macquarie Island.

- ERA-Interim has limited skill reproducing a diurnal cycle as observed, which is likely to be a consequence of the twice-daily initialization of forecasts, at least in part.

- Variability of precipitation throughout the day is not reflected in changes of water content within the MABL.

6.1.4 Evaluation of WRF Simulations of the Marine Atmospheric Boundary Layer over the Southern Ocean with Shipborne Observations

In situ observations from the CAPRICORN (Clouds, Aerosols, Precipitation, Radiation, and atmospherIc Composition Over the southeRn oceaN) field campaign and Himawari-8 satellite products have been used to evaluate the Weather Research and Forecasting (WRFV3.9.1) NWP model in simulating the boundary layer clouds and the MABL structure over the SO. Two cases were examined in this study with a focus on shallow convective clouds that were commonly observed during the cruise. The simulated MABL structure, cloud-top temperature and phase are compared against the observations. Experiments have also been undertaken to test the sensitivity of the simulation to planetary boundary layer schemes and microphysical schemes. Results of the simulations show that:

- For both case studies, the WRF simulations demonstrate a level of skill in representing surface meteorological variables such as temperature, humidity and winds.

- The WRF simulations have difficulties in producing pre- and post-frontal low-level cloud fields, mixed-phase cloud tops, cloud fraction and surface precipitation.

- The thermodynamic profiles suggests that the model does not simulate the growth of the MABL depth prior to the onset of precipitation below the open mesoscale cellular convection.

- The simulations have great difficulties capturing the decoupled and multilayer structure. The MYJ scheme tried to produce this decoupling; however, the simulation is not able to reproduce the same magnitude as observed.

6.2 Final Remarks

The ABL corresponds to the portion of the atmosphere directly and strongly influenced by the underlying surface, where significant fluxes of momentum, heat and/or moisture are carried by turbulent motions. This thesis has explored two especially complex areas of the ABL behaviour: the very stable ABL over land under low winds in Chapter 2 and the ABL over the ocean in Chapters 3, 4 and 5.

The observational analysis of wind-direction shifts and submeso motions in Chapter 2 showed that the very stable ABL at study site exhibits behaviour typical of flat terrain. Sudden changes of wind direction are most likely not local flow perturbations advected by the mean flow but are rather features of generally unknown origin, which needs to be taken into account when developing parametrizations of the stable boundary layer in numerical models.

The analysis of the thermodynamic profiles over Macquarie Island in Chapter 3 and 4 found that ERA-Interim profiles present significant differences between the surface and ∼1,000 m, where the observed values were found to be generally lower than ERA-Interim. The evaluation of MABL height over the SO in Chapter 3 has revealed that under cold-frontal passages, main inversions are underestimated by ERA-Interim. However, the WRF simulations of two case studies over the SO in Chapter 5 showed higher MABL height under post-frontal conditions. These dissimilar results confirm that in general models have difficulties in simulating the MABL in the cold sector of extra-tropical cyclones over the SO.

6.3 Future Work

Several aspects of this research need further investigation. The following directions are of particular interest:

- The climatology study of the diurnal cycle of precipitation presented in Chapter 4 has exclusively focused on surface observation. This work should be extended to the evaluation and validation of the diurnal cycle of precipitation and clouds from

geostationary satellite products like Himawari-8.

- Results from Chapter 5 shows that WRF simulations have limited skill in capturing the decoupling and multilayer structure within the MABL, possibly because of the coarse vertical and horizontal resolution compared with upper-air soundings and radar-lidar products. Higher resolution simulations could be performed, where the decoupling of the MABL is found to be a frequent and wide-spread feature. Case studies with WRF simulations can also be made to gain a better understanding of the role of surface fluxes.

- Recent field experiments such as the 2018 Southern Ocean Cloud Radiation Aerosol Transport Experimental Study (SOCRATES) and the 2017/18 Measurements of Aerosols Radiation Clouds over the Southern Oceans (MARCUS) projects were held to make comprehensive measurements of boundary layer structure and vertical distributions of liquid and mixed-phase clouds. An analysis of these new observations should improve the understanding of the unique features of the atmospheric processes within the MABL over the SO and complement the analysis presented in Chapter 5.

Bibliography

Acevedo, O. C., F. D. Costa, P. E. S. Oliveira, F. S. Puhales, G.a Degrazia, and D. R. Roberti (2014). "The influence of submeso processes on stable boundary layer similarity relationships." In: *J. Atmos. Sci.* 71.1, pp. 207–225. DOI: 10.1175/JAS-D-13-0131.1.

Adams, N. (2009). "Climate trends at Macquarie Island and expectations of future climate change in the sub-Antarctic." In: *Papers and Proceedings of the Royal Society of Tasmania.* Vol. 143. 1, pp. 1–8.

Ahlgrimm, M. and R. Forbes (2014). "Improving the representation of low clouds and drizzle in the ECMWF model based on ARM observations from the Azores." In: *Mon. Wea. Rev.* 142.2, pp. 668–685. DOI: 10.1175/MWR-D-13-00153.1.

Ahn, E., Y. Huang, T. H. Chubb, D. Baumgardner, P. Isaac, M. de Hoog, S. T. Siems, and M. J. Manton (2017). "In situ observations of wintertime low-altitude clouds over the Southern Ocean." In: *Quart. J. Roy. Meteor. Soc.* 143.704, pp. 1381–1394. DOI: 10.1002/qj.3011.

Anderberg, M. R. (1973). *Cluster analysis for applications. Monographs and textbooks on probability and mathematical statistics.*

Anfossi, D., D. Oettl, G. Degrazia, and A. Goulart (2005). "An analysis of sonic anemometer observations in low wind speed conditions." In: *Boundary-Layer Meteorol.* 114.1, pp. 179–203. DOI: 10.1007/s10546-004-1984-4.

Bates, T. S., B. J. Huebert, J. L. Gras, F. B. Griffiths, and P. A. Durkee (1998). "International Global Atmospheric Chemistry (IGAC) project's first aerosol characterization experiment (ACE 1): Overview." In: *J. Geophys. Res.: Atmospheres* 103.D13, pp. 16297–16318. DOI: 10.1029/97JD03741.

Bauer, M. G. and A. D. Del Genio (2006). "Composite analysis of winter cyclones in a GCM: Influence on climatological humidity." In: *J. Climate* 19.9, pp. 1652–1672. DOI: 10.1175/JCLI3690.1.

Bauer, M. G., G. Tselioudis, and W. B. Rossow (2016). "A new climatology for investigating storm influences in and on the extratropics." In: *J. Climate Appl. Meteor.* 55.5, pp. 1287–1303. DOI: 10.1175/JAMC-D-15-0245.1.

Behrangi, A., M. Lebsock, S. Wong, and B. Lambrigtsen (2012). "On the quantification of oceanic rainfall using spaceborne sensors." In: *J. Geophys. Res.: Atmospheres* 117.D20. DOI: 10.1029/2012JD017979.

Behrangi, A., G. Stephens, R. F. Adler, G. J. Huffman, B. Lambrigtsen, and M. Lebsock (2014). "An update on the oceanic precipitation rate and its zonal distribution in light of advanced observations from space." In: *J. Climate* 27.11, pp. 3957–3965. DOI: `10.1175/JCLI-D-13-00679.1`.

Belušić, D. and I. Güttler (2010). "Can mesoscale models reproduce meandering motions?" In: *Q. J. R. Meteorol. Soc.* 136.648, pp. 553–565. DOI: `10.1002/qj.606`.

Belušić, D. and L. Mahrt (2008). "Estimation of length scales from mesoscale networks." In: *Tellus A.* 60.4, pp. 706–715. DOI: `10.1111/j.1600-0870.2008.00328.x`.

— (2012). "Is geometry more universal than physics in atmospheric boundary layer flow?" In: *J. Geophys. Res.: Atmospheres* 117. D09115. ISSN: 2156-2202. DOI: `10.1029/2011JD016987`.

Bennartz, R. (2007). "Global assessment of marine boundary layer cloud droplet number concentration from satellite." In: *J. Geophys. Res.: Atmospheres* 112.D2.

Berry, G., M. J. Reeder, and C. Jakob (2011). "A global climatology of atmospheric fronts." In: *Geophys. Res. Lett.* 38.4. DOI: `10.1029/2010GL046451`.

Billant, P. and J. Chomaz (2000). "Experimental evidence for a new instability of a vertical columnar vortex pair in a strongly stratified fluid." In: *J. Fluid. Mech.* 418, pp. 167–188. DOI: `10.1017/S0022112000001154`.

Bodas-Salcedo, A., P. G. Hill, K. Furtado, K. D. Williams, P. R. Field, J. C. Manners, P P. Hyder, and S. Kato (2016). "Large contribution of supercooled liquid clouds to the solar radiation budget of the Southern Ocean." In: *J. Climate* 29.11, pp. 4213–4228. DOI: `10.1175/JCLI-D-15-0564.1`.

Bodas-Salcedo, A., K. D. Williams, P. R.Field, and A. P. Lock (2012). "The surface downwelling solar radiation surplus over the Southern Ocean in the Met Office model: The role of midlatitude cyclone clouds." In: *J. Climate* 25.21, pp. 7467–7486. DOI: `10.1175/JCLI-D-11-00702.1`.

Bodas-Salcedo, A., K. D. Williams, M. A. Ringer, I. Beau, J. N. S. Cole, J.-L. Dufresne, T. Koshiro, B. Stevens, Z. Wang, and T. Yokohata (2014). "Origins of the solar radiation biases over the Southern Ocean in CFMIP2 models." In: *J. Climate* 27.1, pp. 41–56. DOI: `10.1175/JCLI-D-13-00169.1`.

Boers, R. (1995). "Influence of seasonal variation in cloud condensation nuclei, drizzle, and solar radiation, on marine stratocumulus optical depth." In: *Tellus B: Chem. Phys. Meteorol.* 47.5, pp. 578–586. DOI: `10.3402/tellusb.v47i5.16073`.

— (2001). "Thermodynamic structure of the boundary layer at Cape Grim during ACE-1." In: *Atmospheric Program Australia 1997-98*, p. 27.

Boers, R., J. B. Jensen, and P. B. Krummel (1998). "Microphysical and short-wave radiative structure of stratocumulus clouds over the Southern Ocean: Summer results and seasonal differences." In: *Quart. J. Roy. Meteor. Soc.* 124.545, pp. 151–168. DOI: `10.1002/qj.49712454507`.

Bolton, D. (1980). "The computation of equivalent potential temperature." In: *Mon. Wea. Rev.* 108.7, pp. 1046–1053. DOI: `10.1175/1520-0493(1980)108<1046:TCOEPT>2.0.CO;2`.

Bretherton, C. S. and M. C. Wyant (1997). "Moisture transport, lower-tropospheric stability, and decoupling of cloud-topped boundary layers." In: *J. Atmos. Sci.* 54.1, pp. 148–167. DOI: `10.1175/1520-0469(1997)054<0148:MTLTSA>2.0.CO\%3B2`.

Brown, A. R. (1996). "Evaluation of parametrization schemes for the convective boundary layer using large-eddy simulation results." In: *Boundary-Layer Meteorol.* 81.2, pp. 167–200. DOI: `10.1007/BF00119064`.

Catto, J. L., C. Jakob, G. Berry, and N. Nicholls (2012). "Relating global precipitation to atmospheric fronts." In: *Geophys. Res. Lett.* 39.10. DOI: `10.1029/2012GL051736`.

Cava, D., L. Mortarini, U. Giostra, R. Richiardone, and D. Anfossi (2016). "A wavelet analysis of low-wind-speed submeso motions in a nocturnal boundary layer." In: *Q. J. R. Meteorol. Soc.* DOI: `10.1002/qj.2954`.

Chan, M. A. and J. C. Comiso (2011). "Cloud features detected by MODIS but not by CloudSat and CALIOP." In: *Geophys. Res. Lett.* 38.24. DOI: `10.1029/2011GL050063`.

Chen, F. and J. Dudhia (2001). "Coupling an advanced land surface–hydrology model with the Penn State–NCAR MM5 modeling system. Part I: Model implementation and sensitivity." In: *Mon. Wea. Rev* 129.4, pp. 569–585. DOI: `10.1175/1520-0493(2001)129,0569:CAALSH.2.0.CO;2`.

Chubb, T. H., Y. Huang, J. Jensen, T. Campos, S. Siems, and M. Manton (2016). "Observations of high droplet number concentrations in Southern Ocean boundary layer clouds." In: *Atmos. Chem. Phys.* 16.2, pp. 971–987. DOI: `10.5194/acp-16-971-2016`.

Chubb, T. H., J. B. Jensen, S. T. Siems, and M. J. Manton (2013). "In situ observations of supercooled liquid clouds over the Southern Ocean during the HIAPER Pole-to-Pole Observation campaigns." In: *Geophys. Res. Lett.* 40.19, pp. 5280–5285. DOI: `10.1002/grl.50986`.

Cooper, W. A. (1986). "Ice initiation in natural clouds." In: *Precipitation Enhancement-A Scientific Challenge.* Springer, pp. 29–32.

Da, C. (2015). "Preliminary assessment of the Advanced Himawari Imager (AHI) measurement onboard Himawari-8 geostationary satellite." In: *Remote Sens. Lett.* 6.8, pp. 637–646. DOI: `10.1080/2150704X.2015.1066522`.

Dai, A. (2001). "Global precipitation and thunderstorm frequencies. Part II: Diurnal variations." In: *J. Climate* 14.6, pp. 1112–1128. DOI: `10.1175/1520-0442(2001)014<1112:GPATFP>2.0.CO;2`.

Dai, A., X. Lin, and K. Hsu (2007). "The frequency, intensity, and diurnal cycle of precipitation in surface and satellite observations over low-and mid-latitudes." In: *Clim. Dyn.* 29.7-8, pp. 727–744. DOI: `10.1007/s00382-007-0260-y`.

Dai, J., M. J. Manton, S. T. Siems, and E. E. Ebert (2014). "Estimation of daily winter precipitation in the Snowy Mountains of southeastern Australia." In: *J. Hydrometeor.* 15.3, pp. 909–920. DOI: 10.1175/JHM-D-13-081.1.

Dee, D. P., S. M. Uppala, A. J. Simmons, P. Berrisford, P. Poli, S. Kobayashi, U. Andrae, M. A. Balmaseda, G. Balsamo, P. Bauer, et al. (2011). "The ERA-Interim reanalysis: Configuration and performance of the data assimilation system." In: *Quart. J. Roy. Meteor. Soc.* 137.656, pp. 553–597. DOI: 10.1002/qj.828.

Delanoë, J. and R. J. Hogan (2008). "A variational scheme for retrieving ice cloud properties from combined radar, lidar, and infrared radiometer." In: *J. Geophys. Res.: Atmospheres* 113.D7. DOI: 10.1029/2007JD009000.

Delanoë, J., A. Protat, J. Vinson, W. Brett, C. Caudoux, F. Bertrand, J. Parent du Chatelet, R. Hallali, L. Barthes, M. Haeffelin, et al. (2016). "BASTA: A 95-GHz FMCW Doppler radar for cloud and fog studies." In: *J. Atmos. Oceanic Technol.* 33.5, pp. 1023–1038. DOI: 10.1175/JTECH-D-15-0104.1.

Dong, S., J. Sprintall, and S. T. Gille (2006). "Location of the Antarctic polar front from AMSR-E satellite sea surface temperature measurements." In: *J. Phys. Oceanogr.* 36.11, pp. 2075–2089. DOI: 10.1175/JPO2973.1.

Field, P. R. and R. Wood (2007). "Precipitation and cloud structure in midlatitude cyclones." In: *J. Climate* 20.2, pp. 233–254. DOI: 10.1175/JCLI3998.1.

Galligani, V. S., D. Wang, M. A. Imaz, P. Salio, and C. Prigent (2017). "Analysis and evaluation of WRF microphysical schemes for deep moist convection over south-eastern South America (SESA) using microwave satellite observations and radiative transfer simulations." In: *Atmos. Meas. Tech.* 10.10, p. 3627. DOI: 10.5194/amt-10-3627-2017.

Garratt, J. R. (1994). "The atmospheric boundary layer." In: *Earth. Sci. Rev.* 37.1-2, pp. 89–134. DOI: 10.1016/0012-8252(94)90026-4.

Gates, W. L., J. S. Boyle, C. Covey, C. G. Dease, C. M. Doutriaux, R. S. Drach, M. Fiorino, P. J. Gleckler, J. J. Hnilo, S. M. Marlais, et al. (1999). "An overview of the results of the Atmospheric Model Intercomparison Project (AMIP I)." In: *Bull. Amer. Meteor. Soc.* 80.1, pp. 29–55. DOI: 10.1175/1520-0477(1999)080<0029:AOOTRO>2.0.CO;2.

Govekar, P. D., C. Jakob, M. J. Reeder, and J. Haynes (2011). "The three-dimensional distribution of clouds around Southern Hemisphere extratropical cyclones." In: *Geophys. Res. Lett.* 21. DOI: 10.1029/2011GL049091.

Grachev, A. A., C. W. Fairall, P. O. G. Persson, E. L. Andreas, and P. S. Guest (2005). "Stable boundary-layer scaling regimes: the SHEBA data." In: *Boundary-Layer Meteorol.* 116.2, pp. 201–235. DOI: 10.1007/s10546-004-2729-0.

Güttler, I. and D. Belušić (2012). "The nature of small-scale non-turbulent variability in a mesoscale model." In: *Atmos. Sci. Lett.* 13.3, pp. 169–173. DOI: 10.1002/asl.382.

Hande, L. B., S. T. Siems, and M. J. Manton (2012a). "Observed trends in wind speed over the Southern Ocean." In: *Geophys. Res. Lett.* 39.11. DOI: 10.1029/2012GL051734.

Hande, L. B., S. T. Siems, M. J. Manton, and D. Belusic (2012b). "Observations of wind shear over the Southern Ocean." In: *J. Geophys. Res.: Atmospheres* 117.D12. DOI: 10.1029/2012JD017488.

Haynes, J. M., C. Jakob, W. B. Rossow, G. Tselioudis, and J. Brown (2011). "Major characteristics of Southern Ocean cloud regimes and their effects on the energy budget." In: *J. Climate* 24.19, pp. 5061–5080. DOI: 10.1175/2011JCLI4052.1.

Hewson, T. D. (1998). "Objective fronts." In: *Meteor. Appl.* 5.1, pp. 37–65.

Hignett, P. (1991). "Observations of diurnal variation in a cloud-capped marine boundary layer." In: *J Atmos Sci* 48.12, pp. 1474–1482. DOI: 10.1175/1520-0469(1991) 048<1474:OODVIA>2.0.CO;2.

Holt, T. and S. Raman (1988). "A review and comparative evaluation of multilevel boundary layer parameterizations for first-order and turbulent kinetic energy closure schemes." In: *Rev. Geophys.* 26.4, pp. 761–780. DOI: 10.1029/RG026i004p00761.

Holz, R. E., S. A. Ackerman, F. W. Nagle, R. Frey, S. Dutcher, R. E. Kuehn, M. A. Vaughan, and B. Baum (2008). "Global Moderate Resolution Imaging Spectroradiometer (MODIS) cloud detection and height evaluation using CALIOP." In: *J. Geophys. Res.: Atmospheres* 113.D8. DOI: 10.1029/2008JD009837.

Hong, S., J. Dudhia, and S. Chen (2004). "A revised approach to ice microphysical processes for the bulk parameterization of clouds and precipitation." In: *Mon. Wea. Rev.* 132.1, pp. 103–120. DOI: 10.1175/1520-0493(2004)132<0103:ARATIM>2.0.CO;2.

Hong, S., Y. Noh, and J. Dudhia (2006). "A new vertical diffusion package with an explicit treatment of entrainment processes." In: *Mon. Wea. Rev.* 134.9, pp. 2318–2341. DOI: 10.1175/MWR3199.1.

Hoskins, B. J. and K. I. Hodges (2005). "A new perspective on Southern Hemisphere storm tracks." In: *J. Climate* 18.20, pp. 4108–4129. DOI: 10.1175/JCLI3570.1.

Hu, X., J. W. Nielsen-Gammon, and F. Zhang (2010). "Evaluation of three planetary boundary layer schemes in the WRF model." In: *J. Appl. Meteor. Climatol.* 49.9, pp. 1831–1844. DOI: 10.1175/2010JAMC2432.1.

Hu, Y., D. Winker, M/ Vaughan, B. Lin, A. Omar, C. Trepte, D. Flittner, P. Yang, S. L. Nasiri, B. Baum, et al. (2009). "CALIPSO/CALIOP cloud phase discrimination algorithm." In: *J. Atmos. Ocean. Technol.* 26.11, pp. 2293–2309. DOI: 10.1175/ 2009JTECHA1280.1.

Huang, Y., T. Chubb, D. Baumgardner, M. DeHoog, S. T. Siems, and M. J. Manton (2017). "Evidence for secondary ice production in Southern Ocean open cellular convection." In: *Quart. J. Roy. Meteor. Soc.* 143.704, pp. 1685–1703. DOI: 10.1002/qj. 3041.

Huang, Y., T. Chubb, F. Sarmadi, S. T. Siems, M. J. Manton, C. N. Franklin, and E. Ebert (2018). "Evaluation of wintertime precipitation forecasts over the Australian

Snowy Mountains." In: *Atmos. Res.* 207, pp. 42–61. DOI: 10.1016/j.atmosres.2018.02.017.

Huang, Y., A. Protat, S. T. Siems, and M. J. Manton (2015). "A-train observations of maritime midlatitude storm-track cloud systems: comparing the Southern Ocean against the North Atlantic." In: *J. Climate* 28.5, pp. 1920–1939. DOI: 10.1175/JCLI-D-14-00169.1.

Huang, Y., S. T. Siems, M. J. Manton, L. B. Hande, and J. M. Haynes (2012a). "The structure of low-altitude clouds over the Southern Ocean as seen by CloudSat." In: *J. Climate* 25.7, pp. 2535–2546. DOI: 10.1175/JCLI-D-11-00131.1.

Huang, Y., S. T. Siems, M. J. Manton, A. Protat, and J. Delanoë (2012b). "A study on the low-altitude clouds over the Southern Ocean using the DARDAR-MASK." In: *J. Geophys. Res.: Atmospheres* 117.D18. DOI: 10.1029/2012JD017800.

Huang, Y., S. T. Siems, M. J. Manton, and G. Thompson (2014). "An evaluation of WRF simulations of clouds over the Southern Ocean with A-Train observations." In: *Mon. Wea. Rev.* 142.2, pp. 647–667. DOI: 10.1175/MWR-D-13-00128.1.

Huffman, G. J., R. F. Adler, M. M. Morrissey, D. T. Bolvin, S. Curtis, R. Joyce, B. McGavock, and J. Susskind (2001). "Global precipitation at one-degree daily resolution from multisatellite observations." In: *J. Hydrometeor.* 2.1, pp. 36–50. DOI: 10.1175/1525-7541(2001)002<0036:GPAODD>2.0.CO;2.

Iacono, M. J., J. S. Delamere, E. J. Mlawer, M. W. Shephard, S. A. Clough, and W. D. Collins (2008). "Radiative forcing by long-lived greenhouse gases: Calculations with the AER radiative transfer models." In: *J. Geophys. Res. Atmos.* 113.D13. DOI: 10.1029/2008JD009944.

Irving, D., I. Simmonds, and K. Keay (2010). "Mesoscale cyclone activity over the ice-free Southern Ocean: 1999-2008." In: *J. Climate* 23.20, pp. 5404–5420. DOI: 10.1175/2010JCLI3628.1.

Jakob, C. and G. Tselioudis (2003). "Objective identification of cloud regimes in the Tropical Western Pacific." In: *Geophys. Res. Lett.* 30.21. DOI: 10.1029/2003GL018367.

Janić, Z. I. (2001). *Nonsingular implementation of the Mellor-Yamada level 2.5 scheme in the NCEP Meso model*. US Department of Commerce, National Oceanic and Atmospheric Administration, National Weather Service, National Centers for Environmental Prediction, pp. 1–61.

Jensen, J. B., S. Lee, P. B. Krummel, J. Katzfey, and D. Gogoasa (2000). "Precipitation in marine cumulus and stratocumulus.: Part I: Thermodynamic and dynamic observations of closed cell circulations and cumulus bands." In: *Atmos. Res.* 54.2, pp. 117–155. DOI: 10.1016/S0169-8095(00)00040-5.

Jimi, S. I., J. L. Gras, S. T. Siems, and P. B. Krummel (2007). "A short climatology of nanoparticles at the Cape Grim baseline air pollution station, Tasmania." In: *Environ. Chem.* 4.5, pp. 301–309. DOI: 10.1071/EN07038.

Jones, C. R., C. S. Bretherton, and D. Leon (2011). "Coupled vs. decoupled boundary layers in VOCALS-REx." In: *Atmos. Chem. Phys.* 11.14, pp. 7143–7153. DOI: `0.5194/acp-11-7143-2011`.

Jovanovic, B., K. Braganza, D. Collins, and D. Jones (2012). "Climate variations and change evident in high-quality climate data for Australia's Antarctic and remote island weather stations." In: *Aust. Meteorol. Oceanogr. J* 62, pp. 247–261.

Kaimal, J. C. and J. J. Finnigan (1994). *Atmospheric boundary layer flows: their structure and measurement.* Oxford university press.

Kang, Y., D. Belušić, and K. Smith-Miles (2015). "Classes of structures in the stable atmospheric boundary layer." In: *Q. J. R. Meteorol. Soc.* 141, pp. 2057–2069. DOI: `10.1002/qj.2501`.

Kanitz, T., P. Seifert, A. Ansmann, R. Engelmann, D. Althausen, C. Casiccia, and E. G. Rohwer (2011). "Contrasting the impact of aerosols at northern and southern midlatitudes on heterogeneous ice formation." In: *Geophys. Res. Lett.* 38.17. DOI: `10.1029/2011GL048532`.

Kawai, H., S. Yabu, Y. Hagihara, T. Koshiro, and H. Okamoto (2015). "Characteristics of the cloud top heights of marine boundary layer clouds and the frequency of marine fog over mid-latitudes." In: *J. Meteor. Soc. Japan. Ser. II* 93.6, pp. 613–628. DOI: `10.2151/jmsj.2015-045`.

Klein, S. A. and D. L. Hartmann (1993). "The seasonal cycle of low stratiform clouds." In: *J. Climate* 6.8, pp. 1587–1606. DOI: `10.1175/1520-0442(1993)006<1587:TSCOLS>2.0.CO;2`.

Kloesel K. A .and Albrecht, B. A. (1989). "Low-level inversions over the tropical Pacific-Thermodynamic structure of the boundary layer and the above-inversion moisture structure." In: *Mon. Weather. Rev.* 117.1, pp. 87–101. DOI: `10.1175/1520-0493(1989)117<0087:LLIOTT>2.0.CO;2`.

Lang, F., Y. Huang, M. J. Manton, and S. T. Siems (2018). "Characteristics of the marine atmospheric boundary Layer over the Southern Ocean in response to the synoptic forcing." In: *J. Geophys. Res.: Atmospheres*. DOI: `10.1029/2018JD028700`.

Lim, K. S. and S. Hong (2010). "Development of an effective double-moment cloud microphysics scheme with prognostic cloud condensation nuclei (CCN) for weather and climate models." In: *Mon. Wea. Rev.* 138.5, pp. 1587–1612. DOI: `10.1175/2009MWR2968.1`.

Mace, G. (2010). "Cloud properties and radiative forcing over the maritime storm tracks of the Southern Ocean and North Atlantic derived from A-Train." In: *J. Geophys. Res.: Atmospheres* 115.D10. DOI: `10.1029/2009JD012517`.

Mace, G. G., R. Marchand, Q. Zhang, and G. Stephens (2007). "Global hydrometeor occurrence as observed by CloudSat: Initial observations from summer 2006." In: *Geophys. Res. Lett.* 34.9. DOI: `10.1029/2006GL029017`.

Mace, G., Q. Zhang, M. Vaughan, R. Marchand, G. Stephens, C. Trepte, and D. Winker (2009). "A description of hydrometeor layer occurrence statistics derived from the first year of merged Cloudsat and CALIPSO data." In: *J. Geophys. Res.: Atmospheres* 114.D8. DOI: 10.1029/2007JD009755.

Mahrt, L. (2007). "Weak-wind mesoscale meandering in the nocturnal boundary layer." In: *Environ. Fluid Mech.* 7.4, pp. 331–347. ISSN: 1567-7419. DOI: 10.1007/s10652-007-9024-9.

— (2008). "Mesoscale wind direction shifts in the stable boundary-layer." In: *Tellus A.* 60.4, pp. 700–705. ISSN: 02806495. DOI: 10.1111/j.1600-0870.2008.00324.x.

— (2009). "Characteristics of submeso winds in the stable boundary layer." In: *Boundary-Layer Meteorol.* 130.1, pp. 1–14. DOI: 10.1007/s10546-008-9336-4.

— (2010). "Common microfronts and other solitary events in the nocturnal boundary layer." In: *Q. J. R. Meteorol. Soc.* 136.652, pp. 1712–1722. ISSN: 00359009. DOI: 10.1002/qj.694.

— (2014). "Stably stratified atmospheric boundary layers." In: *Annu. Rev. Fluid. Mech.* 46, pp. 23–45. DOI: 10.1146/annurev-fluid-010313-141354.

Mahrt, L., S. Richardson, N. Seaman, and D. Stauffer (2012). "Turbulence in the nocturnal boundary layer with light and variable winds." In: *Quart. J. Roy. Meteor. Soc.* 138.667, pp. 1430–1439. DOI: 10.1002/qj.1884.

Marchand, R., G. G. Mace, T. Ackerman, and G. Stephens (2008). "Hydrometeor detection using CloudSat-An Earth-orbiting 94-GHz cloud radar." In: *J. Atmos. Ocean. Technol.* 25.4, pp. 519–533. DOI: 10.1175/2007JTECHA1006.1.

Markowski, P. and Y. Richardson (2010). *Mesoscale meteorology in midlatitudes.* Vol. 2. John Wiley & Sons.

Mason, S., J. K. Fletcher, J. M. Haynes, C. Franklin, A. Protat, and C. Jakob (2015). "A hybrid cloud regime methodology used to evaluate southern ocean cloud and shortwave radiation errors in ACCESS." In: *J. Climate* 28.15, pp. 6001–6018. DOI: 10.1175/JCLI-D-14-00846.1.

Mellor, G. L. and T. Yamada (1982). "Development of a turbulence closure model for geophysical fluid problems." In: *Rev. Geophys. Space Phys.* 20.4, pp. 851–875.

Mlawer, E. J., S. J. Taubman, P. D. Brown, M. J. Iacono, and S. A. Clough (1997). "Radiative transfer for inhomogeneous atmospheres: RRTM, a validated correlated-k model for the longwave." In: *J. Geophys. Res.: Atmospheres* 102.D14, pp. 16663–16682. DOI: 10.1029/97JD00237.

Monserrat, S. and A. J. Thorpe (1992). "Gravity-wave observations using an array of microbarographs in the Alearic Islands." In: *Q. J. R. Meteorol. Soc.* 118.504, pp. 259–282. DOI: 10.1002/qj.49711850405.

Monti, P., H. J. S. Fernando, M. Princevac, W. C. Chan, T. A. Kowalewski, and E R E. R. Pardyjak (2002). "Observations of flow and turbulence in the nocturnal

boundary layer over a slope." In: *J. Atmos. Sci.* 59.17, pp. 2513–2534. DOI: 10.1175/1520-0469(2002)059<2513:OOFATI>2.0.CO;2.

Morrison, A. E., S. T. Siems, M. J. Manton, and A. Nazarov (2010). "A modeling case study of mixed-phase clouds over the Southern Ocean and Tasmania." In: *Mon. Wea. Rev.* 138.3, pp. 839–862. DOI: 10.1175/2009MWR3011.1.

Morrison, H., G. Thompson, and V. Tatarskii (2009). "Impact of cloud microphysics on the development of trailing stratiform precipitation in a simulated squall line: Comparison of one-and two-moment schemes." In: *Mon. Wea. Rev.* 137.3, pp. 991–1007. DOI: 10.1175/2008MWR2556.1.

Mortarini, L., M. Stefanello, G. Degrazia, D. Roberti, S. T. Castelli, and D. Anfossi (2016). "Characterization of wind meandering in low-wind-speed conditions." In: *Boundary-Layer Meteorol.* DOI: 10.1007/s10546-016-0165-6.

Muhlbauer, A., I. L. McCoy, and R. Wood (2014). "Climatology of stratocumulus cloud morphologies: microphysical properties and radiative effects." In: *Atmospheric Chemistry and Physics* 14.13, pp. 6695–6716.

Naud, C. M., J. F. Booth, and A. D. Del Genio (2014). "Evaluation of ERA-Interim and MERRA cloudiness in the Southern Ocean." In: *J. Climate* 27.5, pp. 2109–2124. DOI: 10.1175/JCLI-D-13-00432.1.

— (2016). "The Relationship between Boundary Layer Stability and Cloud Cover in the Post-Cold-Frontal Region." In: *J. Climate* 29.22, pp. 8129–8149. DOI: 10.1175/JCLI-D-15-0700.1.

Naud, C. M., D. J. Posselt, and S. C. van den Heever (2015). "A CloudSat–CALIPSO view of cloud and precipitation properties across cold fronts over the global oceans." In: *J. Climate* 28.17, pp. 6743–6762. DOI: 10.1175/JCLI-D-15-0052.1.

Nicholls, S. (1984). "The dynamics of stratocumulus: Aircraft observations and comparisons with a mixed layer model." In: *Quart. J. Roy. Meteor. Soc.* 110.466, pp. 783–820. DOI: 10.1002/qj.49711046603.

Nicholls, S. and J. Leighton (1986). "An observational study of the structure of stratiform cloud sheets: Part I. Structure." In: *Q. J. R. Meteorol. Soc.* 112.472, pp. 431–460. DOI: 10.1002/qj.49711247209.

Nieuwstadt, F .T. M. and P. G. Duynkerke (1996). "Turbulence in the atmospheric boundary layer." In: *Atmos. Res.* 40.2-4, pp. 111–142. DOI: 10.1016/0169-8095(95)00034-8.

Norris, J. R. (1998a). "Low cloud type over the ocean from surface observations. Part I: Relationship to surface meteorology and the vertical distribution of temperature and moisture." In: *J. Climate* 11.3, pp. 369–382. DOI: 10.1175/1520-0442(1998)011<0383:LCTOTO>2.0.CO;2.

— (1998b). "Low cloud type over the ocean from surface observations. Part II: Geographical and seasonal variations." In: *J. Climate* 11.3, pp. 383–403. DOI: 10.1175/1520-0442(1998)011<0369:LCTOTO>2.0.CO;2.

Norris, J. R. and S. F. Iacobellis (2005). "North Pacific cloud feedbacks inferred from synoptic-scale dynamic and thermodynamic relationships." In: *J. Climate* 18.22, pp. 4862–4878. DOI: 10.1175/JCLI3558.1.

Pan, H. and W. Wu (1995). *Implementing a mass flux convection parameterization package for the NMC medium-range forecast model.* Office Note 409, NOAA/EMC, p. 40.

Panofsky, H. A. and J. A. Dutton (1984). "Atmospheric turbulence: models and methods for engineering aplications." In: *Atmospheric turbulence: models and methods for engineering aplications.* John Wiley & Sons.

Pleim, J. E. (2007). "A combined local and nonlocal closure model for the atmospheric boundary layer. Part I: Model description and testing." In: *J. Appl. Meteor. Climatol.* 46.9, pp. 1383–1395. DOI: 10.1175/JAM2539.1.

Pleim, J. E. and J. S. Chang (1992). "A non-local closure model for vertical mixing in the convective boundary layer." In: *Atmos. Environ.* 26.6, pp. 965–981. DOI: 10.1016/0960-1686(92)90028-J.

Pope, M., C. Jakob, and M. J. Reeder (2009). "Regimes of the north Australian wet season." In: *J. Climate* 22.24, pp. 6699–6715. DOI: 10.1175/2009JCLI3057.1.

Poulos, G. S., W. Blumen, D. C. Fritts, J. K. Lundquist, J. Sun, S. P. Burns, C. Nappo, R. Banta, R. Newsom, J. Cuxart, et al. (2002). "CASES-99: A comprehensive investigation of the stable nocturnal boundary layer." In: *Bull. Am. Meteorol. Soc.* 83.4, pp. 555–581. DOI: 10.1175/1520-0477(2002)083<0555:CACIOT>2.3.CO;2.

Rees, J. M. and S. D. Mobbs (1988). "Studies of internal gravity waves at Halley Base, Antarctica, using wind observations." In: *Q. J. R. Meteorol. Soc.* 114.482, pp. 939–966. DOI: 10.1002/qj.49711448206.

Rémillard, J., P. Kollias, E. Luke, and R. Wood (2012). "Marine boundary layer cloud observations in the Azores." In: *J Climate* 25.21, pp. 7381–7398. DOI: doi.org/10.1175/JCLI-D-11-00610.1.

Russell, L. M., D. H. Lenschow, K. K. Laursen, P. B. Krummel, S. T. Siems, A. R. Bandy, D. C. Thornton, and T. S. Bates (1998). "Bidirectional mixing in an ACE 1 marine boundary layer overlain by a second turbulent layer." In: *J. Geophys. Res.: Atmospheres* 103, p. 16. DOI: 10.1029/97JD03437.

Sallée, J.-B., E. Shuckburgh, N. Bruneau, A. J. S. Meijers, T. J. Bracegirdle, and Z. Wang (2013). "Assessment of Southern Ocean mixed-layer depths in CMIP5 models: Historical bias and forcing response." In: *J. Geophys. Res.: Oceans* 118.4, pp. 1845–1862. DOI: 10.1002/jgrc.20157.

Sandu, I., A. Beljaars, P. Bechtold, T. Mauritsen, and G. Balsamo (2013). "Why is it so difficult to represent stably stratified conditions in numerical weather prediction (NWP) models?" In: *J. Adv. Model. Earth Syst.* 5.2, pp. 117–133. DOI: 10.1002/jame.20013.

Sarmadi, F., Y. Huang, S. T. Siems, and M. J. Manton (2017). "Characteristics of wintertime daily precipitation over the Australian Snowy Mountains." In: *J. Hydrometeor.* 2017. DOI: 10.1175/JHM-D-17-0072.1.

Seibert, P., F. Beyrich, S. Gryning, S. Joffre, A. Rasmussen, and P. Tercier (2000). "Review and intercomparison of operational methods for the determination of the mixing height." In: *Atmos. Environ.* 34.7, pp. 1001–1027. DOI: 10.1016/S1352-2310(99)00349-0.

Seidel, D. J., Y. Zhang, A. Beljaars, J. Golaz, A. R. Jacobson, and B. Medeiros (2012). "Climatology of the planetary boundary layer over the continental United States and Europe." In: *J. Geophys. Res.: Atmospheres* 117.D17. DOI: 10.1029/2012JD018143.

Simmonds, I. and K. Keay (2000). "Mean Southern Hemisphere extratropical cyclone behavior in the 40-year NCEP–NCAR reanalysis." In: *J. Climate* 13.5, pp. 873–885. DOI: 10.1175/1520-0442(2000)013<0873:MSHECB>2.0.CO;2.

Skamarock, W. C., J. B. Klemp, J. Dudhia, D. O. Gill, D. M. Barker, M. G. Duda, X. Huang, W. Wang, and J. P Powers (2008). *A description of the advanced research WRF version 3*. NCAR/TN-4751STR NCAR Tech. Note, p. 113.

Srinivas, C. V., R. Venkatesan, and A. B. Singh (2007). "Sensitivity of mesoscale simulations of land–sea breeze to boundary layer turbulence parameterization." In: *Atmos. Environ.* 41.12, pp. 2534–2548. DOI: 10.1016/j.atmosenv.2006.11.027.

Stephens, G. L., T. L'Ecuyer, R. Forbes, A. Gettelmen, J. Golaz, A. Bodas-Salcedo, K. Suzuki, P. Gabriel, and J. Haynes (2010). "Dreary state of precipitation in global models." In: *J. Geophys. Res.: Atmospheres* 115.D24. DOI: 10.1029/2010JD014532.

Streten, N. A. (1988). "The climate of Macquarie Island and its role in atmospheric monitoring." In: *Papers and Proceedings of the Royal Society of Tasmania*. Vol. 122. 1, pp. 91–106.

Stull, R. B. (1988). *An Introduction to Boundary Layer Meteorology*. Vol. 13. Springer Science & Business Media.

— (2006). "The Atmospheric Boundary Layer." In: *Atmospheric science: an introductory survey*. Ed. by J. M. Wallace and P. V. Hobbs. Elsevier. Chap. 9, pp. 375–417.

— (2017). *Practical Meteorology: an algebra-based survey of atmospheric science*. Univ. of British Columbia, p. 940.

Suarez, A., D. R. Stauffer, and B. J. Gaudet (2015). "Wavelet-based methodology for the verification of stochastic submeso and meso-gamma fluctuations." In: *Mon. Wea. Rev.* 143.10, pp. 4220–4235. DOI: 10.1175/MWR-D-15-0075.1.

Sun, J., D. H. Lenschow, L. Mahrt, and C. Nappo (2013). "The relationships among wind, horizontal pressure gradient, and turbulent momentum transport during CASES-99." In: *J. Atmos. Sci.* 70.11, pp. 3397–3414. DOI: 10.1175/JAS-D-12-0233.1.

Sun, J., L. Mahrt, C. J. Nappo, and D. H. Lenschow (2015a). "Wind and temperature oscillations generated by wave–turbulence interactions in the stably stratified boundary layer." In: *J. Atmos. Sci.* 72.4, pp. 1484–1503. DOI: 10.1175/JAS-D-14-0129.1.

Sun, J., C. J. Nappo, L. Mahrt, D. Belušić, B. Grisogono, D. R. Stauffer, M. Pulido, C. Staquet, Q. Jiang, A. Pouquet, et al. (2015b). "Review of wave-turbulence interactions in the stable atmospheric boundary layer." In: *Rev. Geophys.* 53.3, pp. 956–993. DOI: 10.1002/2015RG000487.

Thompson, G., P. R. Field, R. M. Rasmussen, and W. D. Hall (2008). "Explicit forecasts of winter precipitation using an improved bulk microphysics scheme. Part II: Implementation of a new snow parameterization." In: *Mon. Wea. Rev.* 136.12, pp. 5095–5115. DOI: 10.1175/2008MWR2387.1.

Trenberth, K. E. and J. T. Fasullo (2010). "Simulation of present-day and twenty-first-century energy budgets of the southern oceans." In: *J. Climate* 23.2, pp. 440–454. DOI: 10.1175/2009JCLI3152.1.

Van der Hoven, I. (1957). "Power spectrum of horizontal wind speed in the frequency range from 0.0007 to 900 cycles per hour." In: *J. Meteorol.* 14.2, pp. 160–164. DOI: 10.1175/1520-0469(1957)014<0160:PSOHWS>2.0.CO;2.

Vercauteren, N. and R. Klein (2015). "A clustering method to characterize intermittent bursts of turbulence and interaction with submesomotions in the stable boundary layer." In: *J. Atmos. Sci.* 72.4, pp. 1504–1517. DOI: 10.1175/JAS-D-14-0115.1.

Vercauteren, N., L. Mahrt, and R. Klein (2016). "Investigation of interactions between scales of motion in the stable boundary layer." In: *Q. J. R. Meteorol. Soc.* DOI: 10.1002/qj.2835.

Vickers, D. and L. Mahrt (2007). "Observations of the cross-wind velocity variance in the stable boundary layer." In: *Environ. Fluid Mech.* 7.1, pp. 55–71. ISSN: 1567-7419. DOI: 10.1007/s10652-006-9010-7.

Vickers, D., L. Mahrt, and D. Belušić (2008). "Particle simulations of dispersion using observed meandering and turbulence." In: *Acta Geophys.* 56.1, pp. 234–256. DOI: 10.2478/s11600-007-0041-3.

von Engeln, A. and J. Teixeira (2013). "A planetary boundary layer height climatology derived from ECMWF reanalysis data." In: *J. Climate* 26.17, pp. 6575–6590. DOI: 10.1175/JCLI-D-12-00385.1.

Wang, Q., K. Suhre, P.B. Krummel, S.T. Siems, L. Pan, T.S. Bates, J.E. Johnson, D.H. Lenschow, B.J. Huebert, G.L. Kok, R.D. Schillawski, A.S.H. Prevot, and S. Businger (1999). "Characteristics of marine boundary layers during two Lagrangian measurement periods: 1. General conditions and mean characteristics." In: *J. Geophys. Res. Atmos.* 104.D17, pp. 21751–21765. DOI: 10.1029/1998JD100099.

Wang, Z., D. Belusic, Y. Huang, S. T. Siems, and M. J. Manton (2016). "Understanding orographic effects on surface observations at Macquarie Island." In: *J. Appl. Meteor. Climatol.* 55.11, pp. 2377–2395. DOI: 10.1175/JAMC-D-15-0305.1.

Wang, Z., S. T. Siems, D. Belusic, M. J. Manton, and Y. Huang (2015). "A climatology of the precipitation over the Southern Ocean as observed at Macquarie Island." In: *J. Appl. Meteor. Climatol.* 54.12, pp. 2321–2337. DOI: 10.1175/JAMC-D-14-0211.1.

While, J., C. Mao, M. J. Martin, J. Roberts-Jones, P. A. Sykes, S. A. Good, and A. J. McLaren (2017). "An operational analysis system for the global diurnal cycle of sea surface temperature: implementation and validation." In: *Q. J. R. Meteorol. Soc.* 143.705, pp. 1787–1803. DOI: 10.1002/qj.3036.

Wilczak, J. M., S. P. Oncley, and S. A. Stage (2001). "Sonic anemometer tilt correction algorithms." In: *Boundary-Layer Meteorol.* 99.1, pp. 127–150. DOI: 10.1023/A:1018966204465.

Williams, K. D., A. Bodas-Salcedo, M. Déqué, S. Fermepin, B. Medeiros, M. Watanabe, C. Jakob, S. A. Klein, C. A. Senior, and D. L. Williamson (2013). "The Transpose-AMIP II experiment and its application to the understanding of Southern Ocean cloud biases in climate models." In: *J. Climate* 26.10, pp. 3258–3274. DOI: 10.1175/JCLI-D-12-00429.1.

Wilson, L., M. J. Manton, and S. T. Siems (2013). "Relationship between rainfall and weather regimes in south-eastern Queensland, Australia." In: *Int. J. Climatol.* 33.4, pp. 979–991. DOI: 10.1002/joc.3484.

Winters, K. B., P. N. Lombard, J. J. Riley, and E. A D'Asaro (1995). "Available potential energy and mixing in density-stratified fluids." In: *J. Fluid. Mech.* 289, pp. 115–128. DOI: 10.1017/S002211209500125X.

Wood, R. (2012). "Stratocumulus clouds." In: *Mon. Wea. Rev.* 140.8, pp. 2373–2423. DOI: 10.1175/MWR-D-11-00121.1.

Wood, R. and C. S. Bretherton (2006). "On the relationship between stratiform low cloud cover and lower-tropospheric stability." In: *J. Climate* 19.24, pp. 6425–6432. DOI: 10.1175/JCLI3988.1.

Young, I. R., S. Zieger, and A. V. Babanin (2011). "Global trends in wind speed and wave height." In: *Science* 332.6028, pp. 451–455. DOI: 10.1126/science.1197219.

Yue, Q., B. H. Kahn, E. J. Fetzer, and J. Teixeira (2011). "Relationship between marine boundary layer clouds and lower tropospheric stability observed by AIRS, CloudSat, and CALIOP." In: *J. Geophys. Res.: Atmospheres* 116.D18. DOI: 10.1029/2011JD016136.